



**Max-Planck-Institut für Metallforschung**  
Stuttgart

---

# **Low Temperature Sintering Additives for Silicon Nitride**

Branko Matovic

Dissertation  
an der  
**Universität Stuttgart**

---

Bericht Nr. 137  
August 2003



# **Low Temperature Sintering Additives for Silicon Nitride**

**Dissertation**

Von der Fakultät Chemie der Universität Stuttgart

zur Erlangung der Würde eines

**Doktors der Naturwissenschaften (Dr. rer. nat.)**

genehmigte Abhandlung

Vorgelegt von

**Branko Matović**

Aus Kraljevo, Serbien

**Hauptberichter : Prof. Dr. rer. nat. Fritz Aldinger**

**Mitberichter : Prof. Dr. rer. nat. Dr. hc. mult. Günter Petzow**

Tag der mündlichen Prüfung : 15.08. 2003.

**Institut für Nichtmetallische Anorganische Materialien der Universität Stuttgart**

**Max-Planck-Institut für Metallforschung, Stuttgart**

**Pulvermetallurgisches Laboratorium**

**2003**





Dedicated to my daughter Doroteja



## **Acknowledgements**

This Ph. D. work was done from May 2000 to April 2003 in Max-Planck Institute for Metal Research, Stuttgart, supported by a Max-Planck-Society Scholarship.

I am glad to take this opportunity to thank my thesis advisor Prof. Dr. Fritz Aldinger for his earnest involvement and competent guidance in this work.

My special thanks to my group leader Dr. G. Rixecker, with whom even serious work is an entertainment.

I am taking this opportunity to thank Prof. G. Petzow who friendly helped me and accepted to become the "Mitberichter" for my final examination. I also want to thank Prof. E. J. Mittemeijer for giving consent to examine my thesis.

There were many people who helped me: Mr. Kosanovic, Mr. Mager, Mr. Schweitzer, Mr. Kummer, Mr. Labitzke, Miss Predel, Dr. Bunjes, Mr. Bruckner, Mr. Hammoud, Mrs. Feldhofer, Mrs. Schäufler...and many others. Sincere thanks to all of them.

There were many people who made my working and living easier and full of fun. I would like to thank Krenar, friends from the "Indian community: Suba, Biswas, Gautam, Ravi, Datta, Manga, Nana; Korean friends: 1<sup>st</sup> Lee, 2<sup>nd</sup> Lee, 3<sup>rd</sup> Lee... Ann, many Parks; Sandra, Stefanie, Dirk, Anita, Ute, Aleksandar, Marija, Zaklina, Dragan, Amin, El-Shazlyt, Jia and many others.

My special thanks to Dr. S. Boskovic who is "guilty" why for my spending three nice years in PML.

Finally, I am indebted to my family (Dragica and Doroteja) who have borne my pressure with patience and good humour especially to my daughter Doroteja.



## ABSTRACT

This work deals with sintering additives for the low temperature pressureless sintering of  $\text{Si}_3\text{N}_4$ , via a transient liquid technique. Much attention has been given to the development of a sintering process using low-cost  $\text{Si}_3\text{N}_4$  powder (Silzot HQ, Germany) as the starting material and employing sintering additives which are also both economically attractive and enable sintering at low temperatures. Two new additives based on the  $\text{Li}_2\text{O}-\text{Y}_2\text{O}_3$  system ( $\text{LiYO}_2$ ), and on the  $\text{Li}_2\text{O}-\text{Al}_2\text{O}_3-\text{SiO}_2$  system ( $\text{LiAlSiO}_4$ ) were investigated in this study. The grain boundary liquid phases that form from the two additive systems possess similar eutectic temperatures ( $<1300^\circ\text{C}$ ) enabling liquid phase sintering of  $\text{Si}_3\text{N}_4$  at temperatures as low as  $1500^\circ\text{C}$ .

Different procedures for powder homogenization were investigated first. This was necessary because the grain size and shape distribution of the  $\text{Si}_3\text{N}_4$  powder under investigation differ significantly from those of powders normally used for the liquid phase sintering of  $\text{Si}_3\text{N}_4$ . Among three mechanical mixing processes for the introduction of additives in  $\text{Si}_3\text{N}_4$  powder, namely attrition milling, ball milling and vibratory milling, best results were obtained with attrition milling. This method yielded a uniform dispersion of the additive powder in a fine unagglomerated  $\text{Si}_3\text{N}_4$  matrix without contamination. It also produced good sintering characteristics.

The densities obtained for sintered samples with 15 and 20 wt% of  $\text{LiYO}_2$  and with 10 wt% of  $\text{LiAlSiO}_4$  additives, respectively, were more than 98% of the theoretical density.  $\text{Li}_2\text{O}$  is removed in gaseous form during sintering and thus, the liquid phase is partially transient. This creates some potential for good high temperature properties in spite of the low sintering temperature.

The densification step is followed by a phase transformation from  $\alpha\text{-Si}_3\text{N}_4$  to  $\beta\text{-Si}_3\text{N}_4$  in both cases. The lag between these two stages in the sintering process is more pronounced in the  $\text{Li}_2\text{O}-\text{Al}_2\text{O}_3-\text{SiO}_2$  additive system due to the high viscosity of the transient liquid. The degree of  $\alpha\rightarrow\beta$  phase transformation increases during prolonged sintering. The reaction kinetics of the phase transformation were found to be of first-order in both systems.

The microstructure of  $\text{Si}_3\text{N}_4$  materials with the both additives sintered at  $1600^\circ\text{C}$  for 8 h is characterized by a homogeneous distribution of elongated  $\beta\text{-Si}_3\text{N}_4$  grains and glassy phase, located in thin layers at grain boundaries and triple points. The  $\beta\text{-Si}_3\text{N}_4$  grains are surrounded by a glassy phase at almost all grain contacts indicating a good wetting behavior.

Grain growth was observed to be anisotropic in both cases, leading to rod-like crystals providing a microstructure which has potential for enhanced fracture toughness. Fracture toughness values of  $6.7 \text{ MPa}\cdot\text{m}^{1/2}$  and  $6.2 \text{ MPa}\cdot\text{m}^{1/2}$  were measured for the specimens sintered with 15 wt%  $\text{LiYO}_2$  and 10 wt%  $\text{LiAlSiO}_4$  additives, respectively.

The thermal conductivity of  $\text{Si}_3\text{N}_4$  with the  $\text{LiYO}_2$  additive is higher in comparison to the material sintered with  $\text{LiAlSiO}_4$  additive. The decrease in the thermal conductivity in the latter is attributed to the dissolving of aluminum and oxygen in the  $\beta\text{-Si}_3\text{N}_4$  grains which act as phonon scattering sites.

## Contents

Abstract	1
Contents	3
List of figures	6
List of tables	10
<b>1 Introduction</b>	<b>12</b>
<b>2 Literature review</b>	<b>14</b>
2.1 Crystal structure of silicon nitride	14
2.2 Preparative routes for silicon nitride powders	19
2.3 Processing techniques of silicon nitride ceramics	22
2.4 Sintering	24
2.4.1 Basic theory of liquid phase sintering	24
2.4.1.1 Factors controlling liquid phase sintering	24
2.4.2 Basic mechanisms of liquid-phase sintering	27
2.4.2.1 Particle rearrangement	27
2.4.2.2 Solution-precipitation	28
2.4.2.3 Solid-state or skeleton sintering	29
2.5 Liquid phase sintering of silicon nitride	30
2.5.1 Densification	30
2.5.2 Phase transformation	31
2.5.3 Grain growth	31
2.6 Microstructure	32
2.7 Sintering additives	33
2.8 Mechanical Properties of $\text{Si}_3\text{N}_4$	36
2.9 Thermal properties	39
2.10 Oxidation resistance of $\text{Si}_3\text{N}_4$	40
2.11 Applications	41
2.12 Motivation	42
<b>3 Experimental procedure</b>	<b>43</b>
3.1 Characterization	44

---

3.1.1 Measurements of specific surface area and particle size distribution.....	44
3.1.2 X-ray diffraction.....	44
3.1.3 Chemical analysis.....	44
3.1.4 Scanning electron microscopy.....	45
3.2 Results.....	45
3.2.1 Starting material.....	45
3.3 Additive preparation.....	47
3.4 Greenbody fabrication.....	49
3.4.1 High temperature thermogravimetry.....	50
3.4.2 Dilatometry.....	50
3.4.3 Sintering.....	51
3.5 Characterization of the ceramics.....	52
3.5.1 Sintered density and mass loss.....	52
3.5.2 Room temperature fracture toughness.....	52
3.5.3 Determination of thermal conductivity.....	53
<b>4 Powder processing.....</b>	<b>55</b>
<b>5 Densification.....</b>	<b>62</b>
5.1 Dilatometric study.....	62
5.1.1 Densification temperature.....	62
5.1.1.1 $\text{Si}_3\text{N}_4\text{-LiYO}_2\text{-SiO}_2$ system.....	62
5.1.1.2 $\text{Si}_3\text{N}_4\text{-Li}_2\text{O-Al}_2\text{O}_3\text{-SiO}_2$ system.....	67
5.2 Sintering density.....	73
5.3 General remarks.....	80
<b>6 Phase transformation.....</b>	<b>81</b>
6.1 Temperature and time dependence.....	81
6.2 Influence of additive content.....	83
6.3 Kinetics of phase transformation.....	84
6.4 Transformation mechanism.....	86
6.5 Relation of transformation to densification.....	87



<b>7 Microstructure</b> .....	90
7.1 Microstructural observation in systems sintered with <i>LiYO<sub>2</sub> additive</i> .....	91
7.2 Microstructural observation in systems sintered with <i>LiAlSiO<sub>4</sub> additive</i> .....	96
<b>8 Properties</b> .....	100
8.1 Fracture toughness and hardness.....	100
8.2 Thermal conductivity.....	102
<b>9 Conclusions</b> .....	106
<b>Zusammenfassung</b> .....	108
<b>References</b> .....	118
<b>Curiculum Vitea (Lebenslauf)</b> .....	125

## List of figures

Figure	Contents	Page
2.1. a	Crystal structure of trigonal $\alpha$ - $\text{Si}_3\text{N}_4$	15
2.1. b	Crystal structure of hexagonal $\beta$ - $\text{Si}_3\text{N}_4$	16
2.1c	Crystal structure of $\gamma$ - $\text{Si}_3\text{N}_4$ .	17
2.2	Phase relationship in the M-Si-Al-N-O System	18
2.3	Wetting behavior between a liquid and a solid	25
2.4	Equilibrium contact angle between a liquid and a solid	26
2.5	Equilibrium dihedral angle between a grain and the liquid phase	26
2.6	Schematic diagram illustrating the three stages of liquid-phase sintering on a typical sintering curve	29
2.7	Phase transformation in $\text{Si}_3\text{N}_4$ -SiAlON-additive system	31
2.8	Typical microstructure of a liquid-phase sintered $\text{Si}_3\text{N}_4$ ceramics	32
2.9	Dependence of the strength of pressureless sintered $\text{Si}_3\text{N}_4$ on the density	37
3.1	Flow chart of the experimental procedure	43
3.2	Typical Scanning electron micrographs of as-received silicon nitride powder	46
3.3	XRD pattern of as-received Silzot HQ $\text{Si}_3\text{N}_4$ powder	47
3.4. (a)	XRD pattern of synthesized $\text{LiYO}_2$ additive	48
3.4. (b)	SEM micrograph of synthesized $\text{LiYO}_2$ additive	48
3.5	XRD pattern of Li-exchanged zeolite at 800 and 1000°C	49
3.6	Schematic diagram of sample preparation method	50
3.7	Schematic diagram of sintering schedule	51
3.8	A schematic view of the Vickers' microhardness test	53
3.9	Experimental set up for measurement thermal diffusivity	
3.10	Typical curve for thermal diffusivity of $\text{Si}_3\text{N}_4$ ceramics at ambient temperature	54
4.1	The effects of milling time on the specific surface area	56
4.2	SEM photomicrographs of as-received $\text{Si}_3\text{N}_4$ and a powder attrition milled for 4 h	57
4.3	Oxygen content during processing with $\text{LiYO}_2$ additives	

	(milled for 1,2,4 h ; d-dry milling; w-wet milling)	58
4.4. (a)	Backscattered electron images of green compacts showing the Y distribution (LiYO <sub>2</sub> containing Si <sub>3</sub> N <sub>4</sub> mixtures prepared by ball and attrition milling for 1h)	59
4.4. (b)	Backscattered electron images of green compacts showing the Y distribution (LiYO <sub>2</sub> containing Si <sub>3</sub> N <sub>4</sub> mixtures prepared by ball and attrition milling for 2 and 4 h). The light spots represent the additive that is distributed in the green compacts	59
4.5	SEM micrographs of polished and plasma etched sections of the sintered samples made by different homogenization procedures (a-attrition milling and b-vibratory milling)	60
5.1	Length change of Si <sub>3</sub> N <sub>4</sub> green bodies (A-5 wt%, B-10 wt%, C-15 wt%, D-20 wt% of LiYO <sub>2</sub> ) between room temperature and 1500°C	63
5.2	Linear shrinkage versus additive content in dilatometer experiments, after a holding time of 5 min at 1500°C	63
5.3	Density according to dilatometric measurements of Si <sub>3</sub> N <sub>4</sub> with 15 wt% of LiYO <sub>2</sub> additive after a holding time of 5 min at the temperatures indicated	64
5.4	Influence of the amount of LiYO <sub>2</sub> on the densification of Si <sub>3</sub> N <sub>4</sub> samples fired at 1500°C with a holding a time of 5 min	65
5.5	Shrinkage (a) and shrinkage velocity (b) of a silicon nitride green Body with 15% LiYO <sub>2</sub> additive showing characteristic features at (1) 1180°C; (2) 1275°C; (3) 1364°C and (4) 1453°C	66
5.6	Length change of Si <sub>3</sub> N <sub>4</sub> green bodies (A-5 wt%, B-10 wt%, C-15 wt%, D-20 wt% of LAS between room temperature and 1500°C	68
5.7	Linear shrinkage versus LAS additive content in dilatometer experiments, after a holding time of 5 min at 1500°C	68
5.8	Density according to dilatometric measurements of Si <sub>3</sub> N <sub>4</sub> with 10 wt% of LAS additive after a holding time of 5 min	69
5.9	Influence of the amount of LAS additive on the densification of Si <sub>3</sub> N <sub>4</sub> samples fired at 1500°C with a holding a time of 5 min	70
5.10	Shrinkage (a) and shrinkage velocity (b) of a silicon nitride green Body with 15% LAS additive showing characteristic features at (1) 1080°C, (2) 1180°C; (3) 1275°C and (4) 1490°C	71
5.11	The difference in the densification behavior between Si <sub>3</sub> N <sub>4</sub> -LiYO <sub>2</sub> and Si <sub>3</sub> N <sub>4</sub> -LiAlSiO <sub>4</sub> ceramics with 15% of additive sintered at different temperatures from 1500°C up to 1700°C with a holding time of 5 min	73
5.12	Relative densities at 1500°C vs. annealing time for Si <sub>3</sub> N <sub>4</sub> with LiYO <sub>2</sub> additives (5, 10, 15 and 20%)	74
5.13	Relative densities at 1500°C vs. annealing time for Si <sub>3</sub> N <sub>4</sub> with	

	LiAlSiO <sub>4</sub> additives (5, 10, 15 and 20%)	75
5.14	Lithia losses of Si <sub>3</sub> N <sub>4</sub> compacts with 15 wt% of LiYO <sub>2</sub> additive during dilatometric measurement and upon prolonged annealing time at 1500°C	76
5.14	Mass loss as a function of temperature for Si <sub>3</sub> N <sub>4</sub> compacts with different amounts of LiYO <sub>2</sub> and LiAlSiO <sub>4</sub> additives during sintering with a holding time of 5 min	77
5.15	Mass loss of Si <sub>3</sub> N <sub>4</sub> ceramics with the additive systems LiYO <sub>2</sub> (LY) and LiAlSiO <sub>4</sub> (LAS), heat-treated at 1550°C (a) and 1600°C (b) under 0.1 MPa N <sub>2</sub> as a function of soaking time.	78
5.16	Mass loss of Si <sub>3</sub> N <sub>4</sub> ceramics with the additive systems LiYO <sub>2</sub> (LY) And LiAlSiO <sub>4</sub> (LAS), heat-treated at 1550°C (a) and 1600°C (b) Under 0.1 Mpa N <sub>2</sub> as a function of soaking time.	78
5.17	Mass loss of lithium in Si <sub>3</sub> N <sub>4</sub> samples sintered at various temperatures	79
6.1	The phase transformation as a function of temperature in the Si <sub>3</sub> N <sub>4</sub> -LiYO <sub>2</sub> and Si <sub>3</sub> N <sub>4</sub> -LiAlSiO <sub>4</sub> systems for 5 minutes of annealing	81
6.2	The phase transformation as a function of temperature in the Si <sub>3</sub> N <sub>4</sub> -LiYO <sub>2</sub> and the Si <sub>3</sub> N <sub>4</sub> -LiAlSiO <sub>4</sub> systems (15 wt%) for 1 hour of annealing	82
6.3	The effect of additive content on phase transformation during sintering of Si <sub>3</sub> N <sub>4</sub> -LiAlSiO <sub>4</sub> ceramics at different temperature	83
6.4	The effect of additive content on phase transformation during sintering of Si <sub>3</sub> N <sub>4</sub> -LiAlSiO <sub>4</sub> ceramics at 1500°C	84
6.5	Linear dependence of the logarithm of the α-Si <sub>3</sub> N <sub>4</sub> concentration on time for Si <sub>3</sub> N <sub>4</sub> containing various amounts of the LiYO <sub>2</sub> additive at 1450°C	85
6.6	Linear dependence of log α-phase on time for Si <sub>3</sub> N <sub>4</sub> containing various amount of the LiAlSiO <sub>4</sub> additive at 1500°C	86
6.7	Densification and phase transformation as a function of sintering temperature for LiYO <sub>2</sub> -Si <sub>3</sub> N <sub>4</sub> and LiAlSiO <sub>4</sub> -Si <sub>3</sub> N <sub>4</sub> systems	87
6.8	The relationships between densification and phase transformation as a function of sintering time for LiYO <sub>2</sub> -Si <sub>3</sub> N <sub>4</sub> and LiAlSiO <sub>4</sub> -Si <sub>3</sub> N <sub>4</sub> systems for 15 wt% of additive at 1500°C	88
7.1	SEM micrograph of polished and plasma etched section of samples with 15 wt% additive sintered at 1500°C for 0.5 h (a) and for 2 h (b) and for 8 h (c)	91
7.2	SEM image of polished and CF <sub>4</sub> plasma-etched cross section of the sintered Si <sub>3</sub> N <sub>4</sub> material doped with LiYO <sub>2</sub> additive	92
7.3	SEM microstructure of Si <sub>3</sub> N <sub>4</sub> ceramics with total additive content of LiYO <sub>2</sub> by (a) 10 wt%, (b) 15 wt%, (c) 20 wt%, respectively	93

---

7.4	SEM micrograph of polished and plasma etched section of samples with 15 wt% additive sintered at 1600°C for 8 h	94
7.5	XRD pattern of a sample with 15 wt% of additive sintered at 1600°C for 8 h	95
7.6	Backscattered electron images and EDX of $\beta$ -Si <sub>3</sub> N <sub>4</sub> grain	96
7.7	Backscattered electron images and EDX of intergranuly phase	96
7.8	SEM micrograph of polished and plasma etched section of samples with 15 wt% of LiAlSiO <sub>4</sub> additive sintered at 1500°C for 8 h	98
7.9	SEM micrograph of a polished and plasma etched section of a sample sintered with 10 wt% of additive at 1600 °C for 8 h	98
7.10	SEM micrograph of a polished and plasma etched section of a sample sintered with 15 wt% of additive at 1600 °C for 8 h	99
7.11	Backscattered electron images and EDX of $\beta$ -Si <sub>3</sub> N <sub>4</sub> grain. Sample is sintered at 1650°C for 1 h	99
8.1	Variation of fracture toughness and hardness as a function of the annealing time in Si <sub>3</sub> N <sub>4</sub> ceramics sintered with LiYO <sub>2</sub> and LiAlSiO <sub>4</sub> additive systems, respectively at 1500°C	100
8.2	Microstructure and crack path in Si <sub>3</sub> N <sub>4</sub> ceramic sintered with 15 wt% of LiAlSiO <sub>4</sub> additive at 1500°C for 8 h	101
8.3	Microstructure and crack path in Si <sub>3</sub> N <sub>4</sub> ceramic sintered with 15 wt% of LiYO <sub>2</sub> additive at 1600°C for 8 h	102
8.4	Temperature dependence of thermal diffusivity of Si <sub>3</sub> N <sub>4</sub> ceramics sintered with 15 wt% of LiYO <sub>2</sub> (a) and SiAlSiO <sub>4</sub> (b) additive	104

## List of Tables

Table	Contents	Page
2-I	Crystal structure and lattice parameters of $\text{Si}_3\text{N}_4$ modifications	14
2-II	Production of $\text{Si}_3\text{N}_4$ powders	19
2-III	Typical properties of $\text{Si}_3\text{N}_4$ powders produced by various processing techniques	20
2-IV	Microstructural features of liquid-phase sintering as a function of dihedral angles ( $\psi$ )	27
2-V	Oxide additives used for the densification of $\text{Si}_3\text{N}_4$	34
2-VI	Summary of sintering studies of $\text{Si}_3\text{N}_4$ at atmospheric pressure with magnesia and yttria additives and their compounds	35
2-VII	Typical properties (at room temperature) for advanced hot-pressed and pressureless sintered silicon nitrides	36
2-VIII	Flexural strength data on pressureless sintered $\text{Si}_3\text{N}_4$	38
2-IX	Time evolution of $\text{Si}_3\text{N}_4$ from chemical compound to an advanced ceramic	41
3-I	Characteristic analysis of as-received Silzot HQ $\text{Si}_3\text{N}_4$ powder	46
IV-I	Effects of milling time and different types of homogenization procedures on the properties of $\text{Si}_3\text{N}_4$ mixtures	56
IV-II	Densities after sintering at 1600°C with 5% of $\text{LiYO}_2$ additive (TD-theoretical density)	58
5-I	Phase contents of the samples quenched at different temperatures	67
5-II	Phase contents of the samples quenched from different temperatures	72
5-III	Densities after sintering with different amounts of the $\text{LiYO}_2$ additive	75

5-IV	Densities after sintering with different amounts of the $\text{LiAlSiO}_4$ additive	77
8-I	The effect of the additive amount on thermal conductivity for $\text{Si}_3\text{N}_4$ ceramics sintered with $\text{LiYO}_2$ additive	103

## 1 INTRODUCTION

Silicon nitride ( $\text{Si}_3\text{N}_4$ ) has been studied extensively during the last 50 years.  $\text{Si}_3\text{N}_4$  based ceramics were found to possess promising thermal and mechanical properties at high temperatures since 1955 [1]. As reaction bonding was the only method to fabricate  $\text{Si}_3\text{N}_4$  ceramics at that time, the products were not completely dense. For an optimum utilization of the inherent good properties of  $\text{Si}_3\text{N}_4$ , the powders must be fully densified to compacts [2]. High density materials were first obtained early in the 1960s by hot-pressing with small amounts of various oxide and nitride additives [3]. However, only simple shapes could be fabricated by this process. In the beginning of the 1970s research focused on the applications of  $\text{Si}_3\text{N}_4$  as a structural material for gas turbines [4]. As a result pressureless [5] and gas pressure sintering [6] techniques were developed. This made possible the fabrication of components having high density and complex shape. During the past 30 years, many different aspects have been explored, such as the fundamental properties of  $\text{Si}_3\text{N}_4$ , powder production, porous and dense  $\text{Si}_3\text{N}_4$  and amorphous thin films for applications in electronics. It was found that  $\text{Si}_3\text{N}_4$  possesses a unique combination of properties, such as high strength at ambient and high temperatures, good thermal shock resistance due to a low coefficient of thermal expansion, relatively good resistance to oxidation compared to other high-temperature structural materials, high wear resistance and high thermal conductivity. In addition, the density of  $\text{Si}_3\text{N}_4$  is only about 40% of superalloys. This combination of properties makes it possible for  $\text{Si}_3\text{N}_4$  to replace metallic components that are conventionally used as structural materials.

During investigations on the sintering of  $\text{Si}_3\text{N}_4$ , it was also found that some oxides can be dissolved into  $\text{Si}_3\text{N}_4$  grains [7, 8]. Thus, the resulting material is not pure silicon nitride anymore. "Silicon nitride ceramics" is thus a general name for multicomponent mixtures or alloys of  $\text{Si}_3\text{N}_4$ . The solid solutions with  $\text{Al}_2\text{O}_3$  have been referred to as Sialons. The creep and corrosion resistance of high density Sialon was envisaged to be higher than that of sintered  $\text{Si}_3\text{N}_4$  ceramics because of the reduction or elimination of the grain boundary phase [9] which could be aspired to with these materials.

Si-N bonds are predominantly covalent and this is the source of the excellent intrinsic properties of silicon nitride ceramics. However, due to the high degree of covalent bonding, it is very difficult to sinter these materials to full density. As a consequence, several alternative techniques have been developed to improve the densification of  $\text{Si}_3\text{N}_4$  based ceramics [10].



Fully dense  $\text{Si}_3\text{N}_4$  can be produced by the addition of densification additives which allow liquid phase sintering (LPS). A wide range of sintering additives for  $\text{Si}_3\text{N}_4$  have been explored to date [11, 2]. Since the densification rate is strongly related to the type and amount of sintering additives, as are the microstructural development and the thermal and mechanical properties of sintered bodies, there is considerable effort to find and optimize sintering aids for high performance  $\text{Si}_3\text{N}_4$  materials.

In spite of their excellent properties and great potential, the application of  $\text{Si}_3\text{N}_4$  based ceramics is still limited. The main reasons for this is the high cost of raw materials, i.e.  $\text{Si}_3\text{N}_4$  and the sintering additives, in addition to the production process being cost-intensive [12]. In general, high-quality  $\text{Si}_3\text{N}_4$  grades are used in combination with rare-earth oxides ( $\text{RE}_2\text{O}_3$  with e.g.,  $\text{RE}=\text{Y}$ ,  $\text{Ce}$ ,  $\text{Yb}$ ,  $\text{Lu}$ ) [2], which are not only expensive but require high sintering temperatures. Therefore, there is a ongoing search for a production process that utilizes low-cost  $\text{Si}_3\text{N}_4$  powder and sintering additives which are equally cheap and enable attainment of lower sintering temperatures. Recently, more attention has been given to low-temperature sintering of  $\text{Si}_3\text{N}_4$  ceramics with the aim of reducing manufacturing costs [13, 14].

The present investigation deals with the use of low-temperature sintering additives for pressureless sintering of  $\text{Si}_3\text{N}_4$ , via a transient liquid phase technique. Two new additives in the  $\text{Li}_2\text{O}-\text{Y}_2\text{O}_3$  and  $\text{Li}_2\text{O}-\text{Al}_2\text{O}_3-\text{SiO}_2$  systems have been employed. The grain boundary liquid phases (GBLP) originating from these two additives possess a similar eutectic temperature ( $< 1300^\circ\text{C}$ ) but differ in viscosity [15]. It turns out that the chemistry and therefore viscosity and crystallization behavior of the intergranular phase can be tailored by evaporating partially the  $\text{Li}_2\text{O}$ . At the same time, there is a substantial reduction in the processing temperature. From a scientific perspective, this is a good case for studying the role of GBLP in these sintered materials.

The major objectives of this research can be summarized as follows:

1. Optimizing the results of pressureless-sintering in the  $\text{Si}_3\text{N}_4-\text{Li}_2\text{O}-\text{Y}_2\text{O}_3$  and  $\text{Si}_3\text{N}_4-\text{Li}_2\text{O}-\text{Al}_2\text{O}_3-\text{SiO}_2$  systems. This includes finding the best powder homogenization procedures, the lowest effective sintering temperature and the optimum amount of additive.
2. Determining the reaction kinetics of densification, phase transformation and grain growth.
3. Characterizing the evolution of the microstructure.
4. Characterizing thermomechanical and mechanical properties of the sintered materials.

## 2 LITERATURE REVIEW

### 2.1 Crystal structure of silicon nitride

Silicon nitride exists in three crystallographic modifications designated as the  $\alpha$ ,  $\beta$  and  $\gamma$  phases. While the  $\alpha$  and  $\beta$  modifications can be produced under normal nitrogen pressure and have great importance in the production of advanced ceramics, the recently discovered  $\gamma$ - $\text{Si}_3\text{N}_4$  can be formed only at extremely high pressures [16] and has no practical use yet.

In a simple chemical picture, chemical bonding in  $\alpha$ - and  $\beta$ - $\text{Si}_3\text{N}_4$  are due to the overlap of the  $sp^3$  hybrid orbitals of silicon atoms with the  $sp^2$  hybrid orbitals of the nitrogen atoms. Each nitrogen atom has a remaining  $p$  atomic orbital which is nonbonding and occupied by a lone pair of electrons [17, 18].

The basic unit of  $\text{Si}_3\text{N}_4$  is the  $\text{SiN}_4$  tetrahedron. A silicon atom is at the centre of a tetrahedron, with four nitrogen atoms at each corner. The  $\text{SiN}_4$  tetrahedra are joined by sharing corners in such a manner that each nitrogen is common to three tetrahedra. Thus nitrogen has three silicon atoms as neighbors [9]. The structural difference between  $\alpha$ - and  $\beta$ - $\text{Si}_3\text{N}_4$  can be explained by different arrangements of Si-N layers. The basic units are linked together to form puckered six-membered rings which surround large holes. These basal planes form the building blocks for the structures of  $\alpha$  and  $\beta$ - $\text{Si}_3\text{N}_4$ . The  $\alpha$ - $\text{Si}_3\text{N}_4$  structure is formed by stacking the basal planes in the ABCDABCD... order, and  $\beta$ - $\text{Si}_3\text{N}_4$  is constructed of basal planes stacked in the ABAB... sequence [19]. The AB layer is the same in  $\alpha$ - $\text{Si}_3\text{N}_4$  and  $\beta$ - $\text{Si}_3\text{N}_4$ , and the CD layer in  $\alpha$ - $\text{Si}_3\text{N}_4$  is related to the AB layer of  $\beta$ - $\text{Si}_3\text{N}_4$  by a  $c$ -glide plane. Regarding the unit cell dimensions,  $\alpha$ - and  $\beta$ - $\text{Si}_3\text{N}_4$  structures are related by  $a_\alpha \approx a_\beta$  (Table 2-I). The  $\beta$ - $\text{Si}_3\text{N}_4$  structure exhibits channels parallel to the  $c$ -axis which are about 0.15 nm in diameter enabling higher diffusion coefficients of ions compared to the  $\alpha$ -structure. These channels are changed into voids with seven nearest neighbouring nitrogen atoms in  $\alpha$ - $\text{Si}_3\text{N}_4$ . The  $\alpha$ - and  $\beta$ -forms have trigonal and hexagonal symmetry. The relevant crystallographic data are listed in Table 2-I.

Table 2-I : Crystal structure and lattice parameters of  $\text{Si}_3\text{N}_4$  modifications.

Modification	$\alpha$ - $\text{Si}_3\text{N}_4$	$\beta$ - $\text{Si}_3\text{N}_4$	$\gamma$ - $\text{Si}_3\text{N}_4$
Space group	$P31_C$	$P6_3$ or $P6_3/m$	Fd3m
Lattice parameter			
a (nm)	0.7818(3)	0.7595(1)	0.7738
c (nm)	0.5591(4)	0.29023(6)	

The  $\alpha$ -structure belongs to the space group  $P31_C$ , with 28 atoms per unit cell (Fig. 2.1a). Its lattice parameters are very sensitive to the oxygen content dissolved in the structure. This was the reason why it was assumed that  $\alpha$ - $\text{Si}_3\text{N}_4$  is an oxynitride with an oxide content of 0.9-1.48 wt% corresponding to the compositions [21]:  $\text{Si}_{11.5}\text{N}_{15}\text{O}_{0.5}$  and  $\text{Si}_{11.5}\text{Si}_2\text{N}_{15}\text{O}_{0.5}$ . In these formulas some N atoms were replaced with O atoms and other N sites remained vacant.

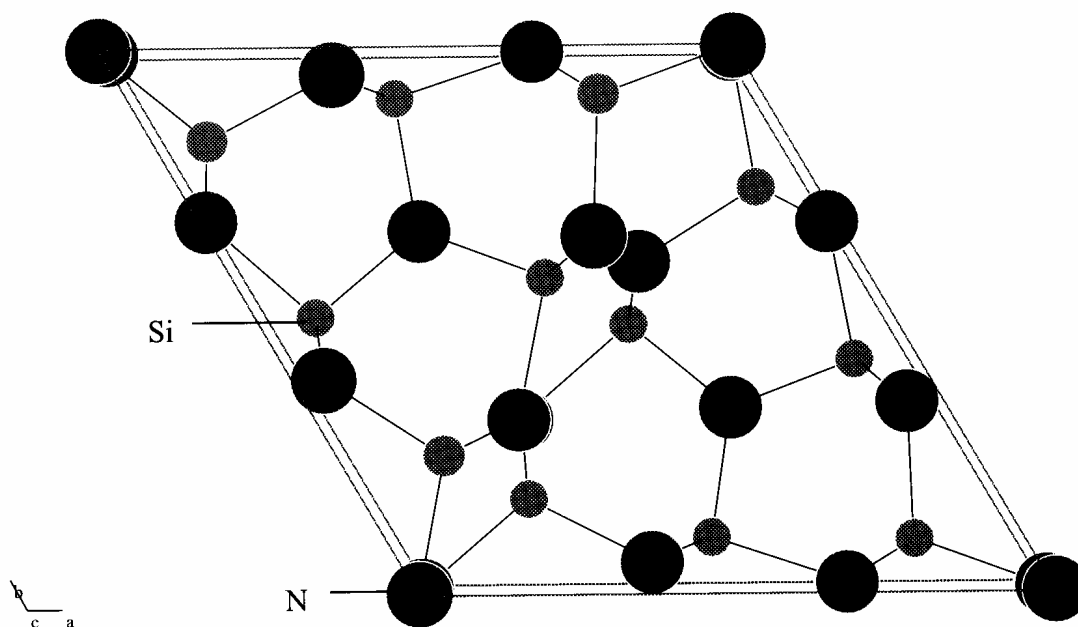


**Fig. 2.1a** : Crystal structure of trigonal  $\alpha$ - $\text{Si}_3\text{N}_4$ . Taken from [2].

However, more detailed investigations showed that the oxygen content was less than that required by the formulas given above [22]. Although oxygen is capable of replacing nitrogen in some sites, it is not needed to form the  $\alpha$ -structure. A refinement of the crystal structure of an  $\alpha$ - $\text{Si}_3\text{N}_4$  single crystal produced by a chemical vapour deposition process clearly demonstrated that the bond length and site occupancy data do not indicate any oxygen in the structure [23].

The atomic arrangement of the  $\beta$ -form is derived from the structure of the mineral phenacite ( $\text{BeSi}_2\text{O}_4$ ), with the oxygen atoms being replaced by nitrogen and the beryllium atoms by silicon [24]. The unit cell of  $\beta$ - $\text{Si}_3\text{N}_4$  consists of  $\text{Si}_6\text{N}_8$  units (Fig. 2.1b). While the literature values of the structural parameters of this modification do not differ remarkably, the real space group, whether centrosymmetric ( $P6_3/m$ ) or acentric ( $P6_3$ ), is still under debate [25]. In the structure of space group  $P6_3/m$ , the silicon and nitrogen atoms lie in mirror planes at  $z=1/4$  and  $z=3/4$ , normal to the  $c$ -axis [26]. In the case of the acentric space group, the nitrogen atoms are slightly displaced from the mirror planes [27].

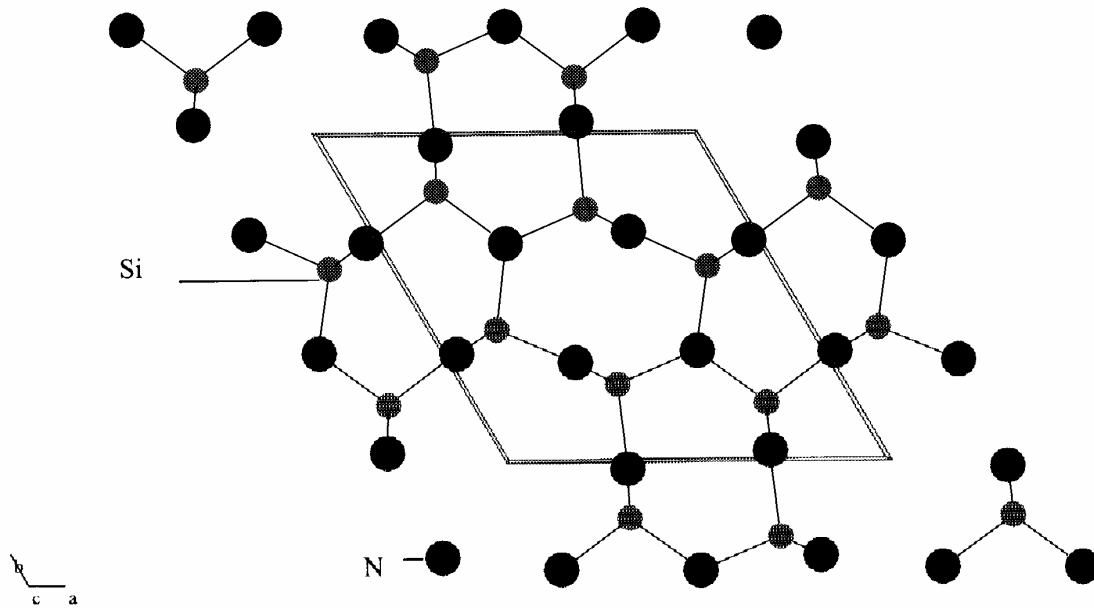


**Fig. 2.1b** : Crystal structure of hexagonal  $\beta$ - $\text{Si}_3\text{N}_4$ . After [2].

During heating above  $1400^\circ\text{C}$ , the  $\alpha$ -phase irreversibly transforms to the  $\beta$ -phase.  $\beta$ - $\text{Si}_3\text{N}_4$  is the thermodynamically more stable phase at all temperatures and hence the transformation from  $\beta$ - to  $\alpha$ -phase is not possible [28]. The transformation is a reconstructive process involving the breaking and reconstruction/formation of six Si-N bonds in each unit cell. This transformation mechanism can proceed only in the presence of liquid phases, that lower the activation energy for transformation. The value for the activation energy in the presence of the liquid phase is about  $405 \text{ kJ/mol}^{-1}$  which is close to the Si-N bond energy ( $435 \text{ kJ/mol}^{-1}$ ) [29]. The recently discovered  $\gamma$ -modification has a cubic structure, similar to the spinel structure [30]. One silicon atom is coordinated tetrahedrally by four nitrogen atoms and two silicon atoms have octahedral coordination by (six) nitrogen atoms (Fig. 2.1c.). This atomic arrangement results in a density of  $3.75 \text{ g cm}^{-3}$ , which is larger than that of  $\alpha$ - and  $\beta$ - $\text{Si}_3\text{N}_4$  ( $3.19 \text{ g cm}^{-3}$ ). In addition, the cubic modification has a hardness of 35.5 GPa, which is larger than that of stishovite, a high pressure phase of  $\text{SiO}_2$  (33 GPa) and significantly higher than the hardness of  $\alpha$ - and  $\beta$ - $\text{Si}_3\text{N}_4$ . Thus, the  $\gamma$ -modification is the third hardest material after diamond and cubic boron nitride [29].

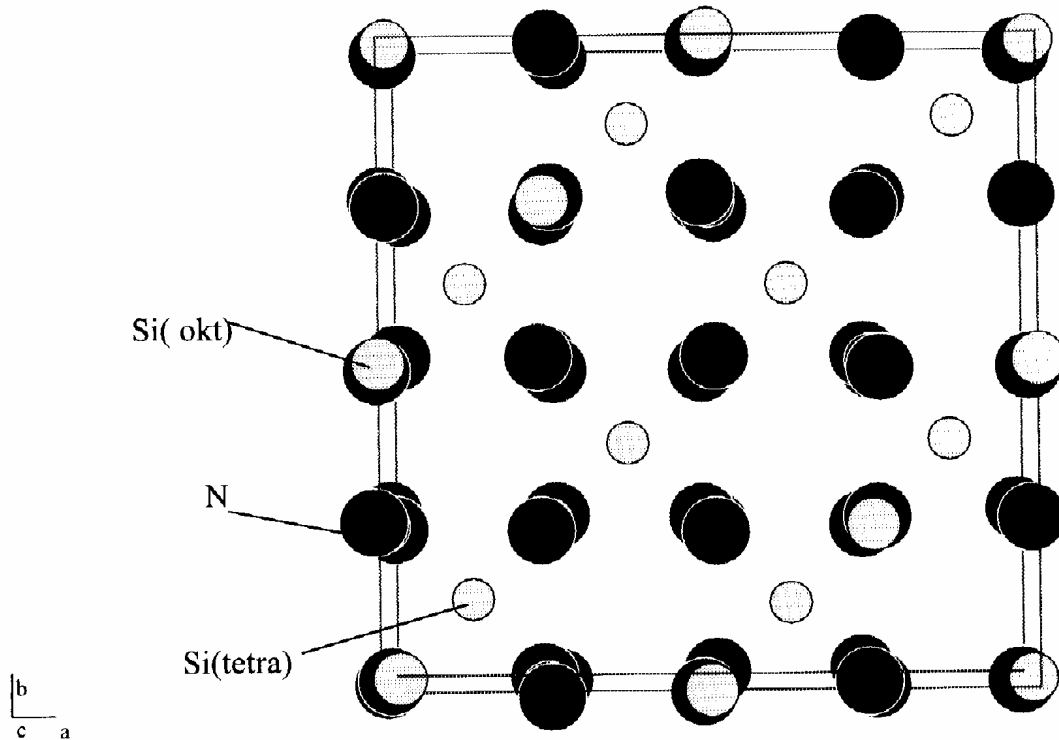


*Fig. 2.1c : Crystal structure of  $\gamma$ - $\text{Si}_3\text{N}_4$ . Taken from [2].*

Silicon and  $\text{Si}_3\text{N}_4$  have a high affinity to oxygen. Since the dimensions of the  $\text{SiN}_4$  tetrahedron are very similar to those of  $\text{SiO}_4$  [30], some oxynitrides exist consisting of both,  $\text{SiO}_4$  and  $\text{SiN}_4$  tetrahedra. The most common oxynitride is built up of  $\text{SiN}_3\text{O}$  tetrahedra which are linked together to form a three-dimensional network with the formula  $\text{Si}_2\text{N}_2\text{O}$ . Moreover, silicon and oxygen atoms in  $\beta$ - $\text{Si}_3\text{N}_4$  can be replaced by Al and O atoms to form the so-called Sialons with the formula  $\text{Si}_{6-z}\text{Al}_z\text{N}_{8-z}\text{O}_z$ , since the unit cell contains two  $\text{Si}_3\text{N}_4$  units. The number of replaced Al and O atoms is represented by the “z” value which can be varied continuously from zero to about 4.2 [31, 32]. The  $\text{Si}_3\text{N}_4$  ceramics with “z” values  $\geq 0.5$  belong to the group of extended  $\beta$ - $\text{Si}_3\text{N}_4$  solid solutions ( $\beta_{\text{SS}}$ ) and all others with “z” values  $\leq 0.5$  belong to group of low  $\beta$ - $\text{Si}_3\text{N}_4$  solid solutions [2]. Similar extended solid solutions can be formed with the addition of BeO or BeN [33]. However, these solid solutions (SiBeON) have no practical use due to the toxicity of Be.

$\alpha$ - $\text{Si}_3\text{N}_4$  has an empty position with a coordination number of eight (7+1), which can be partially occupied by ions with an atomic radius of about 0.1 nm. Occupation of the void position causes a stabilization of the metastable  $\alpha$ - $\text{Si}_3\text{N}_4$ . The cations which can be incorporated in the  $\alpha$  phase are  $\text{Li}^+$ ,  $\text{Mg}^{+2}$ ,  $\text{Ca}^{+2}$ ,  $\text{Y}^{+3}$  and lanthanides with  $Z \geq 60$  [34]. Additionally, Si and N must be replaced by Al and O to obtain electroneutrality. The resulting

$\alpha$ -solid solutions are the so-called  $\alpha$ -Sialons with the formula  $M_xSi_{12-m-n}Al_{m+n}N_{16-n}O_n$ , where  $m$  represents the number of (Si-N) bonds in  $\alpha$ - $Si_3N_4$  which are replaced by (Al-N) bonds,  $n$  is the number of (Si-N) bonds that are replaced by (Al-O) bonds, and  $x$  equals  $m$  divided by the valency of the M cation. The charge discrepancy is compensated by M cations occupying the interstices in the (Si,Al)-(O,N) network. Thus,  $\alpha$ -Sialon can be regarded as a substitutional-interstitial solid solution. The parameter “x” has a minimum value 0.33 for trivalent cations and 0.3 for divalent cations since there is a miscibility gap between  $\alpha$ - $Si_3N_4$  and  $\alpha$ -SiAlON, and the value of  $x$  cannot exceed 2 as there are only two interstitial sites in the unit cell [35]. Since the substitution range of  $\alpha$ -solid solutions is smaller than for  $\beta$  solutions, the formation of single phase  $\alpha$ -Sialon is rather difficult. Deviations from the stoichiometry lead to the simultaneous formation of  $\beta$ -solid solutions. The relationship between  $\alpha$ - and  $\beta$ -Sialon is given in Fig.2.2.

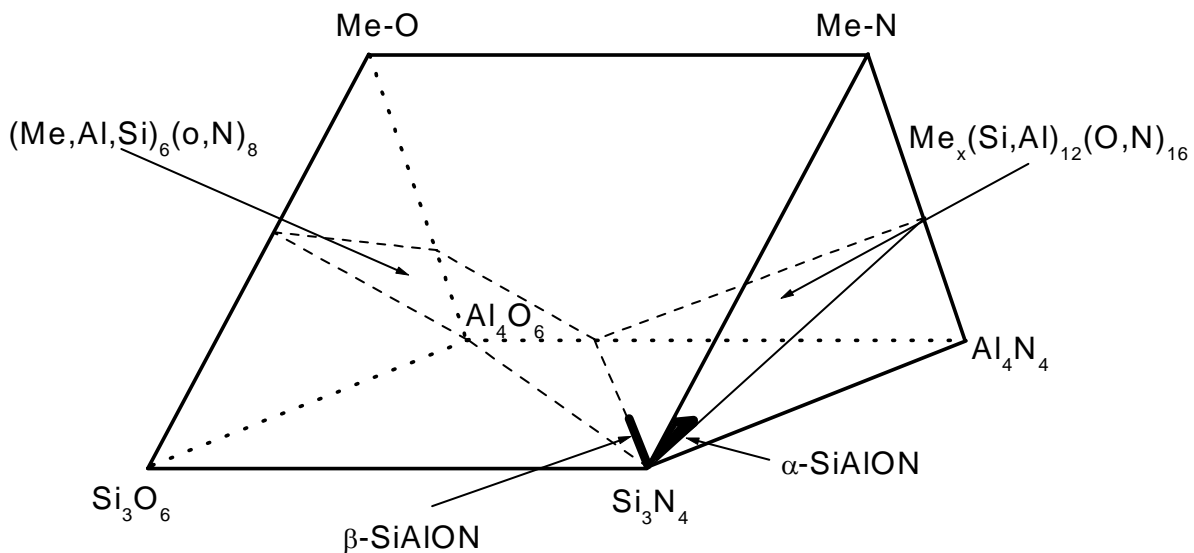
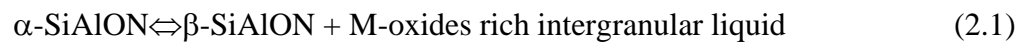


**Fig. 2.2 :** Phase relationship in the M-Si-Al-N-O System [36].

An important feature of the SiAlON system is that the  $\alpha$ - to  $\beta$ -SiAlON phase transformation is fully reversible [37]. The  $\alpha$ -phase is more stable at lower temperatures and can accommodate metal oxides [38]. During the  $\alpha$ - to  $\beta$ -SiAlON transformation metal oxides are rejected to the intergranular regions according to the equation :



Additionally, the phase composition can be controlled by heat treatment procedures.

## 2.2 Preparative routes for silicon nitride powders

Since the occurrence of  $\text{Si}_3\text{N}_4$  as a mineral in nature is very rare [39], all silicon nitride-based ceramics must be produced synthetically. There are many different production routes for  $\text{Si}_3\text{N}_4$  powders, namely

- direct nitridation of silicon
- carbothermic reduction of silica
- diimide synthesis
- vapor phase synthesis
- plasmachemical synthesis
- pyrolyses of silicon organic compounds and
- laser induced reactions.

All of these routes are based on four different chemical processes (Table 2-II) [40]. However, only direct nitridation of silicon and diimide synthesis techniques are commercially viable processes [41].

*Table 2-II : Production of  $\text{Si}_3\text{N}_4$  powders*

Method	Chemical process
direct nitridation	$3 \text{ Si} + 2 \text{ N}_2 \Rightarrow \text{Si}_3\text{N}_4$
carbothermal nitridation	$3 \text{ SiO}_2 + 6 \text{ C} + 2 \text{ N}_2 \Rightarrow \text{Si}_3\text{N}_4 + 6 \text{ CO} \uparrow$
diimide synthesis	$\text{SiCl}_4 + 6 \text{ NH}_3 \Rightarrow \text{Si}(\text{NH})_2 + 4 \text{ NH}_4\text{Cl} \uparrow$ $3 \text{ Si}(\text{NH})_2 \Rightarrow \text{Si}_3\text{N}_4 + 2 \text{ NH}_3 \uparrow$
vapor phase synthesis	$3 \text{ SiCl}_4 + 4 \text{ NH}_3 \Rightarrow \text{Si}_3\text{N}_4 + 12 \text{ HCl} \uparrow$

The reaction conditions may be adjusted to provide powders of different crystallinity,  $\alpha/\beta$  ratio, morphology, particle size, particle size distribution and impurities. Typical chemical analysis data and properties for commercial silicon nitride powders synthesized by different techniques as mentioned above are given in Table 2-III.

The direct nitridation of silicon is performed in an atmosphere of  $\text{N}_2$ ,  $\text{N}_2/\text{H}_2$  or  $\text{NH}_3$  at temperatures above  $1100^\circ\text{C}$  but below the melting point of silicon ( $1410^\circ\text{C}$ ). The  $\alpha$ -phase of

silicon nitride is the major product. Since the  $\beta$ -modification appears only in the presence of a liquid phase,  $\beta$ - $\text{Si}_3\text{N}_4$  formation is favored either by the presence of impurity elements, which are able to form low-melting eutectics, or by nitridation above the melting point of silicon [42]. This reaction is highly exothermic and it is extremely difficult to control the temperature using raw silicon. The heat of reaction can be used for the self-propagating synthesis of  $\text{Si}_3\text{N}_4$  [43]. However, because of the uncontrolled reaction and a significant amount of  $\beta$ -phase in the product, the self-propagation method can not be used for the production of high quality  $\text{Si}_3\text{N}_4$  powders. The process finally results in  $\text{Si}_3\text{N}_4$  lumps which are then crushed and milled. The quality of the final product depends on the purity of the raw material, the milling procedure after nitridation and additional chemical purification of the powder.

The direct nitridation method can be carried out by a plasma chemical reaction, where temperatures on the order of  $5750^\circ\text{C}$  are reached. The time of reaction is very short, resulting in a high amount of amorphous  $\text{Si}_3\text{N}_4$  and nano-crystallites of the  $\alpha$ - and  $\beta$ -phases (about 20 nm). The grain size can be increased to 100 nm by an additional heat treatment process [44].

*Table 2-III : Typical properties of  $\text{Si}_3\text{N}_4$  powders produced by various processing techniques.*

Technique	Direct nitridation of silicon	Vapor phase synthesis	Carbotherma l nitridation	Diimide synthesis
Specific surface area ( $\text{g cm}^{-2}$ )	8-25	3.7	4.8	10
Oxygen content (wt %)	1.0-2.0	1.0	1.6	1.4
Carbon content (wt %)	0.1-0.4	-	0.9-1.1	0.1
Metallic impurities (wt %) $\Sigma$ Fe, Al, Ca	0.07-0.15	0.03	0.06	0.005
Crystallinity (%)	100	60	100	100
$\alpha/(\alpha + \beta)$ (%)	95	95	95	85
Morphology	equiaxed	equiaxed + rod-like	equiaxed + rod-like	equiaxed



Carbothermal nitridation was the earliest method to be used for Si<sub>3</sub>N<sub>4</sub> production [45]. The process involves the nitridation of carbon and silica precursor powder mixtures in a flowing nitrogen atmosphere at temperatures in the range from 1400° up to 1500°C. The overall reaction given in Table II proceeds via a number of intermediate reactions. The first step involves the generation of SiO (gas) by the reduction of silica by carbon :



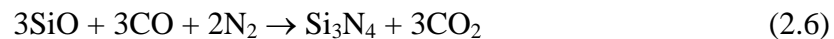
The CO produced in eqn. 2.2 is also capable of reducing further silica through the following reaction:



The carbon within the system can in turn reduce the CO<sub>2</sub> thereby regenerating CO as given by eqn. (2.4):



The SiO(g) produced by eqn. (2.2) or (2.3) reacts with N<sub>2</sub> to form Si<sub>3</sub>N<sub>4</sub> according to the reactions given by eqn. (2.5) and (2.6):



The characteristics of the Si<sub>3</sub>N<sub>4</sub> powders resulting from carbothermic reduction depend on many factors namely the C/SiO<sub>2</sub> ratio, the nitrogen flow rate, reaction temperature, particle size and specific surface area of silica and carbon and the impurities present. Although this route has an advantage over direct nitridation because of the ready availability of the reactants C and SiO<sub>2</sub>, compared to Si powder, the process has not yet been commercialized.

The diimide thermal decomposition fabrication process comprises three major steps : (a) diimide synthesis, (b) diimide thermal decomposition and (c) crystallization. In the first step, silicon tetrachloride (SiCl<sub>4</sub>) and ammonia (NH<sub>3</sub>) are made to react by liquid phase surface reaction or vapor phase reaction to synthesize silicon diimide (Si(NH)<sub>2</sub>) and ammonium chloride (NH<sub>4</sub>Cl). In the following step the Si(NH)<sub>2</sub> is thermally decomposed at a temperature

of about 1000°C to obtain an amorphous silicon nitride powder. During the final step, the amorphous powder is crystallized in a temperature range of 1300-1500°C to form the  $\alpha$ -Si<sub>3</sub>N<sub>4</sub> powder [46]. This powder is characterized by sub-micron equiaxed particles containing a large amount of  $\alpha$ -phase.

The vapor phase synthesis takes place between different gaseous species in the temperature range from 800° up to 1400°C. Usually, the starting materials are SiCl<sub>4</sub> and ammonia which react to form amorphous Si<sub>3</sub>N<sub>4</sub>. Crystallization of the amorphous powder is carried out at temperatures 1300-1500°C. Deagglomeration is also a necessary step to be carried out.

Synthesis of powders by lasers is a useful technique for making nano-size (10-100 nm) powders starting from gaseous or volatile mixtures [47] and is based on the absorption of infrared laser energy e.g., (10.6  $\mu$ m wavelength for CO<sub>2</sub> laser) which is converted into vibrational modes of the reactant gases that produce very high temperatures (above 1000°C) for a short total reaction time (0.1 s or less). These conditions are necessary for the initiation of a chemical reaction the final result of which is the formation of the powder. Due to the coherent nature of the laser source, a well-localized reaction zone can be defined.

The grown particles have a spherical morphology, small size, narrow size distribution and their stoichiometry can be precisely controlled by adjusting the main process parameters such as laser intensity, pressure in the reaction cell, reactant flow rates, reaction gas ratio and temperature of the reaction [48].

All these powders are useful in structural ceramic applications.

### **2.3 Processing techniques of silicon nitride ceramics**

The high degree of covalent bonding makes it very difficult to produce pure dense Si<sub>3</sub>N<sub>4</sub> ceramics by classical sintering (simple heating of powder compacts). The main reason for this is that the diffusion of silicon (at 1400°C  $D_{\text{Si}} \approx 0.5 \times 10^{-19} \text{ m}^2 \cdot \text{s}^{-1}$ ) and nitrogen (at 1400°C  $D_{\text{N}} \approx 6.8 \times 10^{-10} \text{ m}^2 \cdot \text{s}^{-1}$ ) in the volume or at the grain boundaries of Si<sub>3</sub>N<sub>4</sub> is extremely slow [10]. As densification by sintering requires mass transport via volume or grain boundary diffusion and since such diffusion is a thermally activated process, a higher sintering temperature would result in a highly dense material [49]. However, at high temperatures Si<sub>3</sub>N<sub>4</sub> starts to dissociate [50]. Therefore, sintering additives are utilized as a possibility to promote liquid phase sintering and thus enhance volume or grain boundary diffusion. As a consequence, many different sintering techniques have been developed:

---

— Reaction bonding	RBSN
— Hot pressing	HPSN
— Hot-isostatic pressing	HIPSN
— Gas-pressure sintering	GPSN
— Pressureless sintering	SSN

One common densification method is the nitridation of silicon compacts, leading to reaction-bonded silicon nitride (RBSN) materials. By this method, complex shapes can be produced using various ceramic forming methods (slip casting, injection molding, die pressing, isostatic pressing) with low costs. However, the process leads to a material of limited density (about 70-88%) resulting in poor mechanical properties. Because of the residual porosity the strength of RBSN is relatively low. Furthermore, the pore structure leads to high oxidation rates and to small erosion resistance [42, 51]. Thus, low densities and pore structure limit the range of possible applications of RBSN materials.

Hot-pressing of pure silicon nitride powder at high temperatures does not result in full density and leads to the production of porous materials with properties similar to those of RBSN [52]. In spite of this, the first dense  $\text{Si}_3\text{N}_4$  ceramic was that accomplished by hot pressing  $\text{Si}_3\text{N}_4$  powders containing MgO as sintering additive [3]. Such kind of hot-pressed  $\text{Si}_3\text{N}_4$  ceramics (HPSN) is a high strength material, which can be used at temperatures up to 1000°C without a decrease in strength. Because of high cost and difficulties to machine the components, hot-pressing, today, has limited use for the production of simple shaped parts and low quantities.

Another method is to apply isostatic pressure instead of uniaxial pressure, i.e. hot-isostatic pressing (HIPSN). During this process a high gas pressure is applied to consolidate a powder compact or to remove the residual porosity from presintered bodies. The uniform manner of applying the high pressure results in fully isotropic material properties. The possibility to use much higher pressures than in uniaxial hot-pressing leads to an enhancement in the densification of the products. Thus, fully dense ceramic parts can be produced from powders of lower sintering activity and with smaller amounts of additives as compared with uniaxial hot pressing. Three different routes are used in order to produce fully dense ceramics by the HIP technique: (a) HIP densification of  $\text{Si}_3\text{N}_4$  powder compacts, (b) HIP densification of reaction bonded  $\text{Si}_3\text{N}_4$  and (c) HIP densification of normal sintered  $\text{Si}_3\text{N}_4$ . All these techniques lead to materials which combine excellent mechanical and thermo-mechanical properties. The main disadvantage of this method is its high cost. The most common

sintering/densification method for high-strength  $\text{Si}_3\text{N}_4$  ceramics is gas pressure sintering (GPSN). This method allows sintering of complex-shaped parts with medium cost. However, the most economical method is to sinter  $\text{Si}_3\text{N}_4$  powder compacts with additive under 0.1 MPa  $\text{N}_2$  at 1700°-1800°C, i.e. pressureless or normal sintering (SSN). The powder mixtures ( $\text{Si}_3\text{N}_4$  plus additives) are compacted to required shapes by various shaping methods. Complex-shaped components of dense  $\text{Si}_3\text{N}_4$  which require little machining remain after sintering. Because the highest sintering temperature is restricted by thermal dissociation of  $\text{Si}_3\text{N}_4$  [53], relatively large amounts of additives are necessary to fabricate high density materials.

## **2.4 Sintering**

### ***2.4.1 Basic theory of liquid phase sintering***

Liquid phase sintering (LPS) is the sintering process in which a part of the material being sintered is in the liquid state. This is a conventional technique, that has been used to manufacture ceramics for many centuries [54]. LPS is important for systems which are difficult to densify by solid state sintering, i.e. ceramics that possess a high degree of covalent bonding e.g., ( $\text{Si}_3\text{N}_4$  and SiC). The liquid is normally produced from a mixture of at least two powders, a major component and an additive. On heating of the mixture, the additive melts or reacts with a small part of the major component to form a eutectic. The amount of liquid produced at the sintering temperature is usually maintained in the range of 5-15 vol%. In most systems, the liquid does not change its volume. Due to persistence of the liquid throughout the sintering process, this condition is referred to as persistent liquid-phase sintering. In other systems, the liquid may be present over a major part of the sintering process and then disappears by different ways namely

1. incorporation into the solid phase (formation of a solid solution),
2. crystallization of the liquid or devitrification of glassy phase and
3. evaporation.

All these situations are referred to as transient liquid-phase sintering. Transient LPS is a very important technique in the sintering of  $\text{Si}_3\text{N}_4$  with additives for producing dense  $\text{Si}_3\text{N}_4$  based ceramics.

#### ***2.4.1.1 Factors controlling liquid phase sintering***

Liquids with a low surface tension readily wet solids, giving rise to small contact angles,

while liquids with a high surface tension show poor wetting, forming larger contact angles (Fig. 2.3). At the molecular level, if the cohesion between the liquid molecules is smaller than the adhesion between the liquid and solid, the liquid has a tendency to wet the solid. The degree of wetting is quantified by the equilibrium contact angle that forms between the liquid and the solid and is defined in Fig. 2.4. If the energies of the liquid/vapor, solid/vapor and solid/liquid interfaces are  $\gamma_{lv}$ ,  $\gamma_{sv}$  and  $\gamma_{sl}$  respectively, then a simple balance of forces indicates equilibrium according to the equation given below

$$\gamma_{sv} = \gamma_{sl} + \gamma_{lv} \cdot \cos\theta \quad (2.7)$$

Hence, higher values of  $\gamma_{sv}$  and lower values of  $\gamma_{sl}$  and/or  $\gamma_{lv}$  promote wetting. This equation, derived by Young and Dupre [55], shows that a necessary condition for liquid-phase sintering to occur is that the contact angle must lie between 0 and  $90^\circ$  (to stay consistent with the drawings). For higher contact angles ( $>\pi/2$ ), the liquid will bead up in the pores and the sintering can occur only by the solid-state mechanism. The contact angle also has an important effect on the magnitude and nature of the capillary forces exerted by the liquid on the solid grains [56].

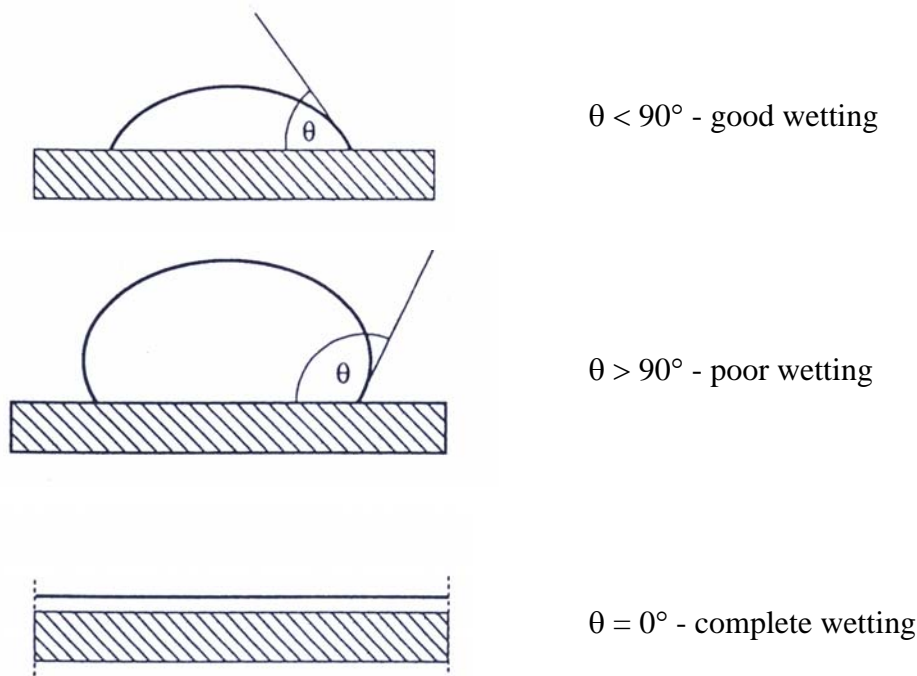


**Fig. 2.3 :** Wetting behavior between a liquid and a solid.

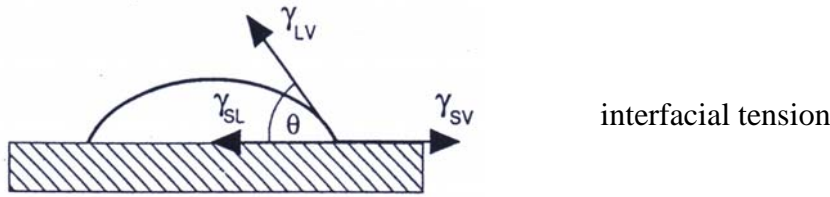


**Fig. 2.4 :** Equilibrium contact angle between a liquid and a solid.

The other necessary condition for LPS is that the liquid distributes itself to cover the surfaces of the particulate solids. The complete penetration and separation of the grain boundary by the liquid depends on the dihedral angle which is defined as the angle between the solid/liquid interfaces as sketched in Fig. 2.5 :

$$\gamma_{gb} = 2 \gamma_{sl} \cos (\psi/2) \quad (2.8)$$

The grain boundary energy ( $\gamma_{gb}$ ) must be less than twice the solid/liquid surface energy  $\gamma_{sl}$  [57]. Thus, high values of  $\gamma_{gb}$  and low values of  $\gamma_{sl}$  are desirable. The microstructural features obtained for various values of the dihedral angle are listed in table 2-IV. For  $\psi = 0$ , the liquid completely penetrates the grain boundaries and no solid/solid contact exists. As  $\psi$  increases, the penetration of the liquid phase between the grains decreases and the number of solid/solid contacts increases.

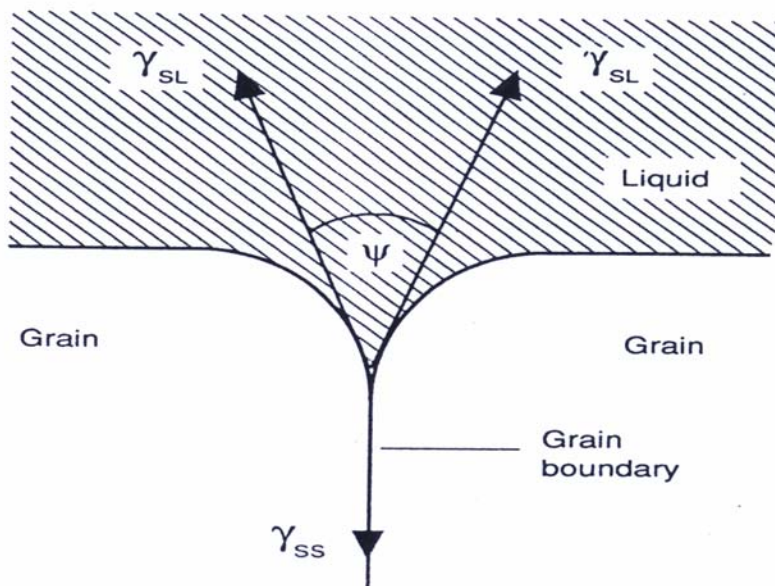


**Fig. 2.5 :** Equilibrium dihedral angle between a grain and the liquid phase.

*Table 2-IV Microstructural features of liquid-phase sintering as a function of dihedral angles ( $\psi$ ).*

Dihedral angle ( $\psi$ )	Microstructure
0°	isolated grains separated by liquid phase
0-60°	partial penetration of grain boundaries by liquid along the three-grain edges
60-120°	isolated pockets of liquid at extended four-grains junctions
≥ 120°	isolated liquid phase at four grain junctions

Surface tension between solids and liquids generates capillary forces, which may give rise to very strong attractive forces among neighboring grains. The contact stress that is generated upon grain impingement, in combination with the lubricating potential of the liquid, enhances the dissolution of solids leading to rapid particle rearrangement and densification. The main processing parameters, such as particle size, green density, sintering temperatures, time and atmosphere, have large effects on the material characteristics obtained by liquid-phase sintering. All of these factors contribute to the complexity and difficulty in understanding liquid-phase sintering mechanisms.

#### ***2.4.2 Basic mechanisms of liquid-phase sintering***

The plausible mechanisms for liquid-phase sintering have been described in detail by Kingery [58, 59], Petzow et al. [60] and German [61]. In order to understand these mechanisms, a number of experimental and theoretical investigations were made. All of them come to the same conclusion that the LPS process occurs in three stages, so that there is some degree of overlapping between the theories. Classically, the following sequence of sintering stages is considered to be prevailing:

1. Particle rearrangement,
2. Solution-reprecipitation and
3. Solid-state or skeleton sintering.

##### ***2.4.2.1 Particle rearrangement***

Rearrangement is the dominant process in the first stage. After a liquid has been formed within the powder compact, rapid densification occurs, due to liquid capillary forces via the

movement of the solid particles from their initial positions towards an arrangement of random dense packing and a higher degree of space filling. Rearrangement is also an effective densification phenomenon during the whole shrinkage period, even during solid state sintering [62].

This process is rapid. However, except for large liquid contents, it cannot lead to complete densification. Many parameters, such as the amount of liquid, its viscosity, green density, wetting, sintering temperature etc. strongly affect this stage. Kingery's model gives an empirical approach in which the rate of densification corresponds approximately to the viscous flow and follows a relation as given below:

$$\Delta L/L_0 \approx 1/3 \Delta V/V_0 \approx t^{1+y} \quad (2.9)$$

where  $\Delta L$  is the change in length and  $L_0$  the original length,  $\Delta V$  and  $V_0$  correspond to the change in volume and initial volume respectively. The exponent  $1+y$  is slightly greater than unity due to the fact that pore sizes decrease and the driving force increases during the process, while at the same time  $t$ , the resistance to rearrangement, increases from the initially pure viscous flow. There are other approaches to analyzing the rearrangement during liquid-phase sintering, such as analysis of the capillary forces between particles separated by a liquid layer. All of these models are quite complex and calculations are very cumbersome.

#### ***2.4.2.2 Solution-precipitation***

In the second stage, the rearrangement efficiency decreases significantly and the solution-precipitation process becomes dominant. Capillary forces generate a difference in the chemical potential at the points of contact between grains when compared to the areas that are not in contact. This chemical potential gradient induces the dissolution of atoms at the contact points and their reprecipitation away from the contact areas, which leads to shrinkage and densification. The necessary condition for the process to occur would be a finite solubility of the solid in the liquid and good wetting ability of the liquid. In addition to densification, coarsening can occur simultaneously by the dissolution of the smaller particles and their reprecipitation on the larger particles. The dissolution and reprecipitation of dissolved materials contributes to the microstructural development, shape accommodation and grain growth.

There are two theories explaining the evolution of densification during liquid phase sintering, namely the contact flattening theory and the pore filling theory. The fundamental difference between these theories lies in whether the grain shape is changed or not during densification



of the powder compact. Kingery [58] proposed that shrinkage and hence densification is achieved by the matter transport from the contact area between grains to the off-contact neck region, analogous to solid-state sintering. The contact regions between particles become flat. This process results in a continuous change in grain shape until there is a complete elimination of the pores. A number of investigations were confirmed this theory [59, 63, 64, 65, 66].

Another mechanism of densification has been proposed according to microstructural observations [67]. In this model, an isolated pores were eliminated by the instantaneous filling with liquid [68, 69]. Upon prolonged sintering, the liquid pocket is eliminated by microstructural homogenization due to material deposition of the grains at the concave surfaces and growth toward the liquid pocket center. Once the the pore filling occurs, the grains grow into the liquid pocket, resulting in microstructural homogenization [70, 71, 72]. This solution-precipitation process is the classic Ostwald ripening process [73]. Dissolution of the small grains and precipitation away from the contact points causes the centers of the larger grains to approach each other, resulting in shrinkage. Ostwald ripening is thought to accompany the densification process.

#### 2.4.2.3 Solid-state or skeleton sintering

The last stage is referred to as solid-state controlled sintering. The overall shrinkage or densification rates are significantly reduced due to formation of a rigid skeleton that inhibits further rearrangement [74, 75]. Coarsening is the dominant process. The three stages of liquid-phase sintering are sketched as a sintering curve in Fig. 2.6. Particle rearrangement is

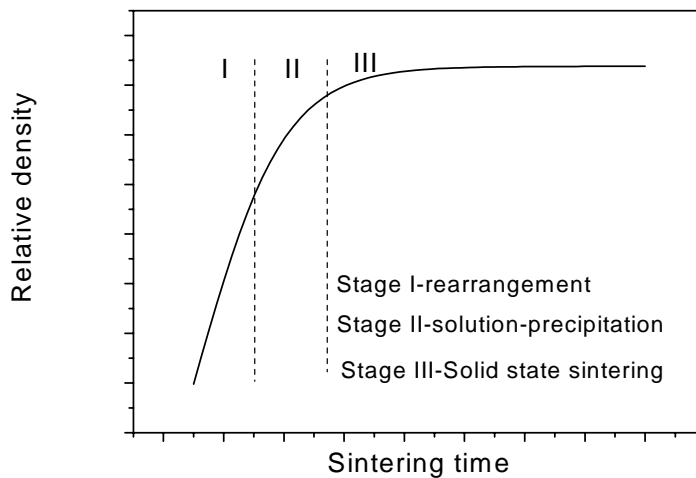


**Fig. 2.6 :** Schematic diagram illustrating the three stages of liquid-phase sintering on a typical sintering curve.

the process occurring the fastest on a time scale of minutes [76]. The solution-precipitation process and skeleton sintering depend on diffusion through the liquid and solid, respectively, and hence, are slower in comparison to I stage (particle rearrangement)

## **2.5 Liquid phase sintering of silicon nitride**

Many manufacturing techniques such as pressureless sintering, gas-pressure sintering, hot-pressing and hot-isostatic pressing, that are employed for obtaining dense  $\text{Si}_3\text{N}_4$  bodies, are related to liquid-phase sintering. The sintering behaviour of  $\text{Si}_3\text{N}_4$  ceramics is affected directly by the characteristics of the liquid phase present. If the liquid fulfills the conditions of good wettability and solubility of  $\text{Si}_3\text{N}_4$ , densification can be described according to the standard mechanisms of liquid phase sintering: particle rearrangement, solution-precipitation and particle coalescence (or grain growth). During the sintering of  $\alpha\text{-Si}_3\text{N}_4$ , the phase transformation to  $\beta\text{-Si}_3\text{N}_4$  is an additional phenomenon interrelated with this sequence.

### **2.5.1 Densification**

The densification of  $\text{Si}_3\text{N}_4$  is negligible before the formation of the liquid. Once the liquid is formed, densification takes place through particle rearrangement, due to capillary forces as detailed above. The extent of particle rearrangement is mainly dependent on the size and shape of particles and amount and viscosity of the liquid phase. The rearrangement process ceases when interparticle contacts are formed that prevent the system from further densification. After formation of the particle bridges, however, the solution-precipitation process starts resulting in the collapse of the bridging. This leads to densification by secondary rearrangement and center-to-center approach [62]. The driving forces for the second stage are the higher solubility at the contact points of the particles and the differences in the chemical potentials between small and large particles, that lead to dissolution of small particles and precipitation of matter on the surface of larger particles.

There are two possible rate controlling steps during solution-precipitation, namely surface reaction and solute diffusion [77]. Which process would be dominant can be decided if the activation energies are obtained from the reaction kinetics. In case of the surface reaction, the activation energy ranges from 290 to 435 kJ/mol. This value matches the Si-N bond energy [78]. For the solute diffusion mechanism, the reaction activation energy lies in the range of 580-730 kJ/mol. These values correspond to the energies of Si diffusion in various silicate

glasses [79]. In addition, the reaction is not sensitive to changes in either the liquid composition or the liquid content for the surface reaction controlled mechanism when compared to the solute diffusion mechanism.

### 2.5.2 Phase transformation

The  $\alpha$ - $\text{Si}_3\text{N}_4$  phase is thermodynamically unstable during sintering (e.g. at 1400-2000°C and 0.1 to 100 MPa  $\text{N}_2$  pressure [2]) and shows a tendency to transform into the more stable  $\beta$ - $\text{Si}_3\text{N}_4$ . The transformation is a reconstructive one [80]. This process involves the breaking and reforming of Si-N bonds. The nearest neighbour atoms remain the same in both the crystallographic forms [81]. The relations of  $\alpha$ - and  $\beta$ - $\text{Si}_3\text{N}_4$  with  $\alpha$ - and  $\beta$ -SiAlON are shown in Fig.2.7. While the  $\beta \rightarrow \alpha$ - $\text{Si}_3\text{N}_4$  transformation has not been observed, the transformation between  $\alpha$ - and  $\beta$ -Sialon is reversible [38].

Phase transformations play an important role for microstructural development. Different microstructures are possible depending on the location where reprecipitating of solute occurs. This location of reprecipitation can be either new  $\beta$ -nuclei generated by supersaturation [82] or the pre-existing  $\beta$ -grains, which coexist with the  $\alpha$ -phase in the starting powders. If the raw powder contains a low concentration of  $\beta$ -grains, high supersaturation in the liquid phase

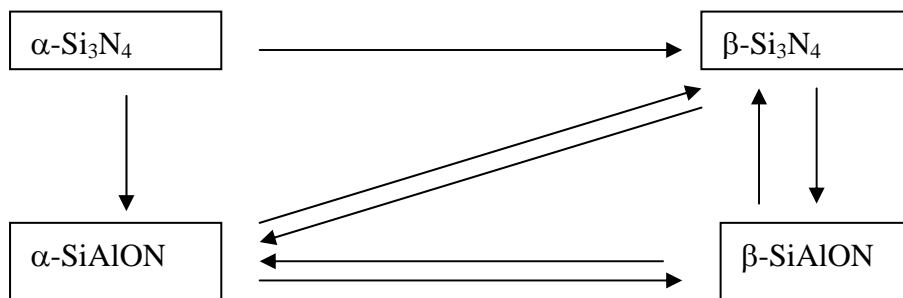


**Fig. 2.7 :** Phase transformation in  $\text{Si}_3\text{N}_4$ -Sialon-additive system.

is created locally resulting in a spontaneous nucleation and crystallization of idiomorphic rod-like  $\beta$ -grains. The precipitation on pre-existing  $\beta$ -grains results in a coarser and more equiaxed structure [83].

### 2.5.3 Grain growth

Growth of  $\text{Si}_3\text{N}_4$  grains is commonly observed during sintering. The driving force originates from the curvature difference between grains [84].  $\text{Si}_3\text{N}_4$  prism planes are more stable compared to basal planes. However, basal planes grow faster than the prism planes resulting in a needle like-grain morphology. The difference in growth rates is related to an energetically more favourable attachment of a surface nucleus on the basal plane [2]. The growth kinetics can be described by the following formula :

$$G^n - G_o^n = kt \quad (2.10)$$

where  $G$  is average grain size,  $G_o$  the initial grain size,  $k$  the kinetic constant, and  $t$  the observation time. The grain growth occurs in order for it to reach a steady state. When the grains grow in a steady state, the normalized grain-size distribution is invariant with time, independent of the initial grain-size distribution, and the exponent  $n$  is 3 for diffusion control [85] and 2 for interface-reaction control [86].

### 2.6 Microstructure

After the liquid phase sintering the microstructure of dense  $\text{Si}_3\text{N}_4$  consists mainly of  $\beta\text{-Si}_3\text{N}_4$  and of mostly amorphous grain-boundary phases. During cooling, the liquid solidifies to amorphous or partially crystalline secondary phases, which are located either at the grain boundaries in the form of thin layers or at triple junctions (Fig. 2.8). This intergranular phase strongly affects the mechanical properties, especially at high temperatures. The thickness of



**Fig. 2.8 :** Typical microstructure of a liquid-phase sintered  $\text{Si}_3\text{N}_4$  ceramics [schematic (a) and SEM micrograph (b)].

1-  $\text{Si}_3\text{N}_4$  matrix grains, 2-crystalline secondary phase, 3-amorphous residue at triple junctions and grain boundaries.

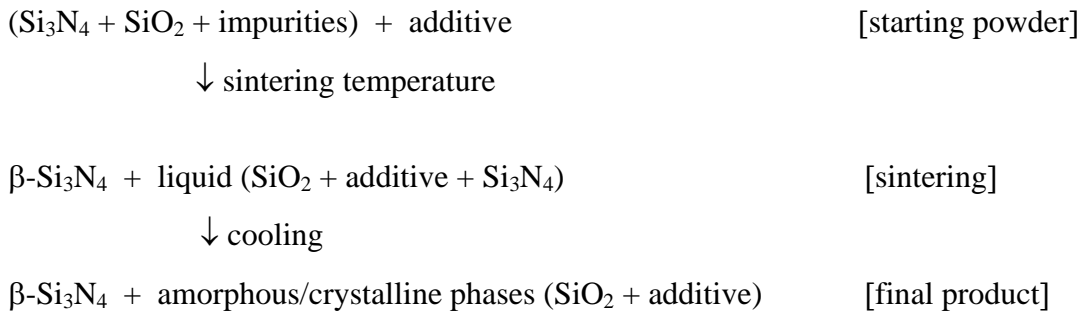
the grain boundary film depends rather on the types of additives than on the amount of liquid phase. An increase in the latter leads only to an increasing volume of the triple points [87].

A typical feature of sintered  $\text{Si}_3\text{N}_4$  ceramics is the morphology of the  $\text{Si}_3\text{N}_4$  grains. Residual  $\alpha$ -grains are equiaxed. The  $\beta$ -phase exhibits an elongated grain structure with an aspect ratio (ratio of length to thickness) usually in the range of 5 to 10 [88, 89].

The microstructural development is controlled mainly by the  $\text{Si}_3\text{N}_4$  starting powders, the additives used and the sintering parameters.

## 2.7 Sintering additives

The desirable properties of  $\text{Si}_3\text{N}_4$  ceramics are achieved only in a fully dense material. However, it is difficult to densify  $\text{Si}_3\text{N}_4$  into a usable form without the use of sintering additives as discussed previously. Thus, using additives is a prerequisite for obtaining dense  $\text{Si}_3\text{N}_4$  ceramics. The type and amount of sintering additives determine the liquid forming temperature, the onset of densification and its rate during sintering [11]. They also define the morphology of the  $\beta$ -grains and the characteristics of the grain-boundary phase, which in turn controls the high-temperature properties. The role of the additive can be expressed by the following reactions:



Silica at the surface of  $\text{Si}_3\text{N}_4$  powder particles reacts with the sintering additive producing a liquid phase. The melting temperature of the additive- $\text{SiO}_2$  composition and the amount and viscosity of the resulting liquid phase are closely connected with the  $\text{SiO}_2$  concentration on the  $\text{Si}_3\text{N}_4$  particle surfaces, the amount of dissolved  $\alpha\text{-Si}_3\text{N}_4$  in the liquid and the impurity content of the starting powder. The liquid promotes densification through a solution-reprecipitation mechanism. Upon cooling, the liquid solidifies and forms the residual intergranular glassy phase and possibly secondary crystalline phases [90], as already explained in 2.6.

Different types of additives have been employed for the pressureless and pressure-assisted sintering of  $\text{Si}_3\text{N}_4$  ceramics [11, 49, 2, 91, 92] :

(a) Binary metal oxides or ternary oxides which do not form solid solutions with  $\text{Si}_3\text{N}_4$ . They remain as an amorphous or partially crystallized silicate grain-boundary phase. The more thoroughly investigated additives are  $\text{MgO}$ ,  $\text{Y}_2\text{O}_3$ ,  $\text{Al}_2\text{O}_3$ ,  $\text{La}_2\text{O}_3$ ,  $\text{CeO}_2$ ,  $\text{Yb}_2\text{O}_3$ ,  $\text{ZrO}_2$ ,  $\text{Li}_2\text{O}$ ,  $\text{MgAl}_2\text{O}_4$ ,  $\text{ZrSiO}_4$ .

(b) Oxides or non-oxides or their mixtures which form solid solutions with  $\text{Si}_3\text{N}_4$ , like  $\text{BeO}$ ,  $\text{AlN}$ ,  $\text{Al}_2\text{O}_3 + \text{AlN}$ ,  $\text{Y}_2\text{O}_3 + \text{AlN}$ ,  $\text{ZrN}$ ,  $\text{ZrC}$ ,  $\text{Mg}_3\text{N}_2$ . They also form liquid phases with silica from the  $\text{Si}_3\text{N}_4$  surface.  $\alpha\text{-Si}_3\text{N}_4$  is dissolved in the liquid and re-precipitated as  $\beta\text{-Si}_3\text{N}_4$  solid solution which has incorporated a certain amount of the starting additive. During sintering, the amount and composition of the liquid phase changes gradually and it has been envisaged to be possible to produce a material without an amorphous intergranular phase [93, 94].

The eutectic temperatures of the commonly used oxide systems for the liquid-phase sintering of  $\text{Si}_3\text{N}_4$  are listed in Table 2-V. However, it has been indicated that the presence of N lowers these eutectic temperatures further [95]. The alkali and alkaline-earth oxides have a low melting point and the viscosity of the resulting liquid is also low. The solution-diffusion-precipitation processes are enhanced. In case of rare-earth oxides, the melting temperatures with  $\text{SiO}_2$  are higher and densification rates are lower [96].

Table 2-V : Oxide additives used for the densification of  $\text{Si}_3\text{N}_4$ .

Additive $\text{M}_x\text{O}_y$	Temperature of liquid formation, °C	
	Silicate $\text{M}_x\text{O}_y\text{-SiO}_2$	Oxynitride $\text{M}_x\text{O}_y\text{-SiO}_2\text{-Si}_3\text{N}_4$
$\text{Li}_2\text{O}$	1030	1030 [97]
$\text{MgO}$	1543	1390 [97]
$\text{Y}_2\text{O}_3$	1650	1480 [98]
$\text{CeO}_2$	1560	1460 [97]
$\text{ZrO}_2$	1640	1590 [97]
$\text{CaO}$	1435	1435 [97]
$\text{Al}_2\text{O}_3$	1595	1470 [98]

The viscosity of the liquid phase has a strong effect on the grain morphology which in turn affects the mechanical properties. Materials processed with additives that form liquid phases of higher viscosity consist of grains with a high aspect ratio [99], and as a consequence,

exhibit better mechanical properties both at room temperature and at high temperatures. A good example for different behavior of sintering additives are magnesia and yttria, respectively. The temperature of liquid formation for the MgO-SiO<sub>2</sub>-Si<sub>3</sub>N<sub>4</sub> system is lower by nearly 100°C in comparison with the Y<sub>2</sub>O<sub>3</sub>-SiO<sub>2</sub>-Si<sub>3</sub>N<sub>4</sub> system (Table 2-V). The MgO melt has also a lower viscosity than Y-SiAlON melts. The solubility of Si<sub>3</sub>N<sub>4</sub> in a magnesium-containing melt is higher than in a yttrium-containing one. Therefore, the effect of MgO additive as a sintering aid is more beneficial. On the other hand, the higher viscosity and melting point of yttrium-containing liquid allow the sintered product to retain its thermomechanical properties at higher temperatures.

From Tables 2-V and 2-VI, it is clear that the sintering behaviour is improved with increasing amount of additives. However, high additive amounts above 20 vol% for certain

*Table 2-VI : Summary of sintering studies of Si<sub>3</sub>N<sub>4</sub> at atmospheric pressure with magnesia and yttria additives and their compounds [100].*

Additive	Sintering temperature (°C)	Sintered density (% Th. D.)
5 mol% MgO	1500-1700	86
10 mol% spinel (MgO·Al <sub>2</sub> O <sub>3</sub> )	1650-1900	96
5 wt% MgO + 0.15 wt% CaO + 0.8 wt% FeO + 4 wt% Y <sub>2</sub> O <sub>3</sub> + 2 wt% Al <sub>2</sub> O <sub>3</sub>	1750	95
10 wt% MgO·Al <sub>2</sub> O <sub>3</sub>	1600-1750	97
5 wt% MgO + BeO + CeO <sub>2</sub>	1800	97
4 mol% Y <sub>2</sub> O <sub>3</sub> + 2 mol% Al <sub>2</sub> O <sub>3</sub>	1725	Not mentioned
10 wt% Y <sub>2</sub> O <sub>3</sub> + 3 wt% Al <sub>2</sub> O <sub>3</sub>	1600-1750	98
3.5-20 wt% Y <sub>2</sub> O <sub>3</sub> + 20 wt% Al <sub>2</sub> O <sub>3</sub>	1750-1825	100
10 mol% Y <sub>2</sub> O <sub>3</sub> + 20 mol% SiO <sub>2</sub>	1750	90
4-17 wt% Y <sub>2</sub> O <sub>3</sub> + 2-4 wt% Al <sub>2</sub> O <sub>3</sub>	1500-1750	95

thermodynamically less stable additives and/or high oxygen content of the starting powders can cause the formation of gas bubbles by increasing in the formation of gaseous SiO [101].

Also, the ratio of the components in the additive has a major influence on the evolution of the microstructure. In case of yttria and alumina additives, with decreasing ratio of  $Y_2O_3$  to  $Al_2O_3$ , the microstructure becomes finer with a lower aspect ratio [102].

During sintering, the amount and composition of the additives may be changed due to interaction with the atmosphere. Using nitrogen alumina can be partially reacted to AlN which is very easily dissolved in the  $Si_3N_4$  lattice causing a shift of the liquid phase composition and the structural properties of the  $Si_3N_4$  ceramics. At high sintering temperatures, the alkali and alkaline-earth oxides are unstable and evaporate. On the other hand, rare-earth oxides are more stable than the other additives [103, 104], and even during long sintering times no change in their concentration has been found.

## 2.8 Mechanical properties of $Si_3N_4$ materials

Typical data for the properties of hot-pressed and pressureless sintered  $Si_3N_4$  are presented in Table 2-VII. It can be inferred from the given data that  $Si_3N_4$  possesses high strength, good thermal-shock resistance due to the low coefficient of thermal expansion and relatively good resistance to oxidation compared to other high-temperature structural materials [105].

Table 2-VII : Typical properties (at room temperature) for advanced hot-pressed and pressureless sintered silicon nitrides [106].

Property	Hot pressed $Si_3N_4$	Pressureless sintered $Si_3N_4$
Density ( $g/cm^3$ )	>3.20	3.20
Thermal conductivity (W/mK)	29.3	15.5
Flexural strength (MPa)	1200	
Compressive strength (MPa)	4500	4000
Thermal expansion ( $10^{-6}/K$ )	3.2	3.4
Young's modulus (GPa)	320	280
Toughness- $K_{Ic}$ ( $MNm^{3/2}$ )	8.3	5.4

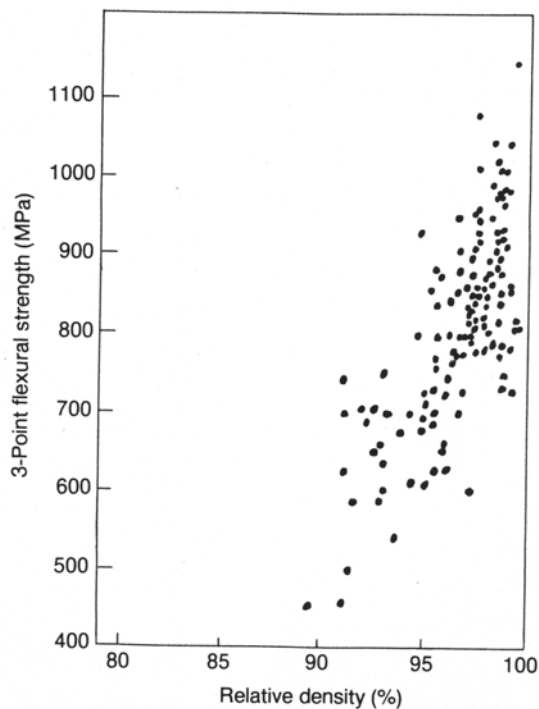
The mechanical property of  $Si_3N_4$  ceramics depend on pores present, cracks and inclusions. Among these factors, porosity has been demonstrated to have a pronounced effect on strength.



Fig. 2.9 shows the relationship of the relative density and strength of pressureless sintered  $\text{Si}_3\text{N}_4$  with yttria and alumina additives.

Fracture toughness differs mainly with variations in the microstructure. The grain shape and the size and phase composition of the grain-boundary phase have a strong influence. High fracture toughness of  $\text{Si}_3\text{N}_4$  based ceramics could be explained on the basis of similar toughening mechanisms as in whisker reinforced composite materials (grain bridging, pull-out, crack deflection, and crack branching [107, 108, 109]). However, these toughening mechanisms are only active when the dominant fracture mode is intergranular.

The ratio of transgranular to intergranular fracture depends on the strength of both intergranular-phase and  $\text{Si}_3\text{N}_4$  grains. A material with higher toughness has a weaker grain boundary. On the other side, the strength of the grain-boundary phase is connected with the local residual stresses [110]. When the thermal expansion coefficient of the grain-boundary phase is higher than that of the  $\text{Si}_3\text{N}_4$  grains, the grain-boundary phase is under tensile stress and the fraction of intergranular fracture is high. As a consequence, the fracture toughness



**Fig. 2.9 :** *Dependence of the strength of pressureless sintered  $\text{Si}_3\text{N}_4$  on the density. After [106]*

increases. In contrast, ceramics with a grain boundary phase under compression have low fracture toughness because of a higher amount of transgranular fracture [111].

A comparison of the flexural strength values of pressureless sintered  $\text{Si}_3\text{N}_4$  at ambient and high temperature is given in Table 2-VIII.

Table 2-VIII : Flexural strength data of pressureless sintered  $\text{Si}_3\text{N}_4$ . After [100].

Additive	Flexural strength	
	room temperature (MPa)	high temperature (MPa)
10 mol% spinel	706	-
$\text{Y}_2\text{O}_3$ , $\text{Al}_2\text{O}_3$	412	-
15 wt% ( $\text{MgO} + \text{Al}_2\text{O}_3$ )	351	-
3.5-20 wt% $\text{Y}_2\text{O}_3$ + 0-20 wt% $\text{Al}_2\text{O}_3$	700	455 (at 1200°C)
5 wt% ( $\text{MgO} + \text{BeO} + \text{CeO}_2$ )	827	428 (at 1200°C)
15 mol% $\text{Y}_2\text{O}_3$	473	-
3-10 wt% $\text{Y}_2\text{O}_3$	450	-
3-10 wt% $\text{CeO}_2$	520	-
3.3-7.2 mol% $\text{CeO}_2$ + 12.8-20 mol% $\text{SiO}_2$	709	393 (at 1200°C)
4.3 wt% $\text{Y}_2\text{O}_3$ + 3.6 wt% $\text{SiO}_2$	826	338 (at 1200°C)
4 wt% $\text{CeO}_2$ + 4 wt% $\text{SiO}_2$	778	356 (at 1200°C)
6.3 wt% $\text{La}_2\text{O}_3$ + 3.6 wt% $\text{SiO}_2$	729	412 (at 1200°C)
5.9 wt% $\text{Sm}_2\text{O}_3$ + 3.6 wt% $\text{SiO}_2$	696	455 (at 1200°C)
7.5 mol% $\text{Y}_2\text{O}_3$ + 7.5 mol% $\text{Pr}_6\text{O}_{11}$	800	>800 (at 1300°C)
1 wt% $\text{Al}_2\text{O}_3$ + 3 wt% $\text{CeO}_2$	750	-
2 wt% $\text{Al}_2\text{O}_3$ + 5 wt% $\text{Y}_2\text{O}_3$	860	-
5-10 wt% Y-Al-garnet	779	-
13.4 wt% $\text{ZrO}_2$ + 2.2 wt% $\text{Y}_2\text{O}_3$ + 4.1 wt% $\text{Al}_2\text{O}_3$	422	463 (at 1200°C)

The amount, composition and degree of crystallization of the grain boundary phase are the key factors for a successful development of  $\text{Si}_3\text{N}_4$  ceramics for applications at elevated temperatures. Additives which result in amorphous silicate phases with a low softening point and low viscosity, such as alkali and alkaline earth oxides and  $\text{Al}_2\text{O}_3$  and  $\text{AlN}$ , generally have a high strength at room temperature. However, due to a low softening point, they are not well suited for high temperature applications. Refractory intergranular phases with a higher degree of crystallinity were obtained by yttria or other rare earth oxides as sintering additives [112, 113]. The high temperature properties of  $\text{Si}_3\text{N}_4$  with rare-earth oxides as sintering additive increase with decreasing ionic radii. The most superior high temperature properties are found

with  $\text{Lu}_2\text{O}_3$  as sintering additive due to the presence of  $\text{Lu}_2\text{Si}_2\text{O}_7$  and  $\text{Lu}_4\text{Si}_2\text{O}_7\text{N}_2$  as the grain boundary phases [2].

The presence of nitrogen in silicate glass helps to produce hard and refractory grain boundaries in the sintered product, thus improving its high temperature properties.

## ***2.9 Thermal properties***

Thermal conductivity is one interesting property of  $\text{Si}_3\text{N}_4$  which combined with the excellent mechanical properties make it a serious candidate for high-performance substrates [114]. Firstly, Haggerty and Lightfoot pointed out  $\text{Si}_3\text{N}_4$  as a material with potentially high thermal conductivity at room temperature [115]. Calculation shows that the intrinsic thermal conductivity of  $\beta\text{-Si}_3\text{N}_4$  single crystals is  $320 \text{ W m}^{-1} \text{ K}^{-1}$  which is similar to the thermal conductivity of SiC and AlN that have been successfully fabricated for commercial uses as high thermal conductivity substrates and heatsinks [116]. However, relatively poor thermal conductivity values, ranging from 20 to  $70 \text{ W m}^{-1} \text{ K}^{-1}$  have been reported for  $\text{Si}_3\text{N}_4$  ceramics fabricated by reaction bonding [11], chemical vapor deposition [117], hot pressing and hot-isostatic-pressing methods [118]. Very recently, Watari et al. fabricated a  $\text{Si}_3\text{N}_4$  with thermal conductivity value of  $155 \text{ W m}^{-1} \text{ K}^{-1}$  by a novel processing technique termed grain-orientation technology [116].

It is postulated that heat flow in hexagonal  $\beta\text{-Si}_3\text{N}_4$  is different depending on the crystal axis. In single crystal measurements it was shown that the conductivity along the c-axis is about three times higher than that along the a-axis [119].

The thermal conductivity of  $\text{Si}_3\text{N}_4$  ceramics depends strongly on the amount of Al impurities and/or sintering additives because the incorporation of Al and O in the  $\beta\text{-Si}_3\text{N}_4$  structure reduces the thermal conductivity of the grains due to the reduced free path of phonons. Thus, Al-free sintering additives are a precondition for the production of  $\text{Si}_3\text{N}_4$  ceramics with high thermal conductivity [2]. Internal defects in the grains [120] and increasing grain boundary thickness were also found to decrease the thermal conductivity [121].

From a commercial point of view, it is very important to fabricate high thermal conductivity  $\text{Si}_3\text{N}_4$  ceramics by conventional sintering technique such as pressureless sintering. Seeding combined with careful control of grain boundary composition can be one processing strategy for this purpose. In addition, microstructure design for harmonizing high thermal conductivity

with good mechanical and electrical properties is also very important for the widespread use of  $\text{Si}_3\text{N}_4$  ceramics as a high thermal conductivity material [114].

## 2.10 Oxidation resistance of $\text{Si}_3\text{N}_4$ materials

As silicon nitride materials are used in oxidising environments, a number of studies have been made on the oxidation of  $\text{Si}_3\text{N}_4$  sintered with different additive systems [122, 123, 124, 125, 126, 127, 128].

$\text{Si}_3\text{N}_4$  is thermodynamically unstable in air. However, it is protected against further oxidation by a thin surface layer of amorphous silica. Generally, there are three oxidation reactions, which can cause oxidation of  $\text{Si}_3\text{N}_4$ :



Reaction 2.11 forms a dense oxide layer that inhibits further oxidation and is therefore called passive oxidation. Once an oxide layer is formed the rate of further reaction is controlled by the oxygen diffusion through this layer and shows a parabolic rate law:

$$(\Delta G/A)^2 = K_p t \quad (2.13)$$

where  $(\Delta G/A)$  is the weight gain per unit area,  $t$  is the oxidation time and  $K_p$  is the parabolic rate constant. Reactions 2.12 a and b occur at low oxygen partial pressures. The reactions proceed in a continuous manner. This is the so-called active oxidation which does not form a protective layer and thus proceeds as long as the oxygen (or  $\text{SiO}_2$ ) is not completely consumed.

There are a number of other parameters which influence the oxidation. The presence of impurity elements increases the rate of oxidation if they are incorporated into the amorphous layer, where they are normally concentrated by segregation and increase the oxygen diffusivity [129]. An opposite effect is observed if these elements promote the crystallization of oxide phases on the surface, resulting in a lower oxygen diffusivity and a decreased oxidation rate. Oxidation also increases if crystalline secondary oxynitride phases oxidize. This reaction involves a significant increase of volume as in the case of some silicon yttrium-

oxynitrides. The volume increase can produce surface flaws thereby creating fresh surfaces [130].

## 2.11 Applications

$\text{Si}_3\text{N}_4$  based materials, as described previously, have good mechanical and thermal properties, which are well-balanced compared to other ceramic materials. They are lighter and possess better heat resistance and wear resistance than metals. For example, SiC is an excellent heat conductor, however, its toughness and thermal shock resistance are behind that of  $\text{Si}_3\text{N}_4$ . Toughened zirconia can exhibit much higher strength and toughness as  $\text{Si}_3\text{N}_4$ , but its high temperature properties and thermal shock resistance are poor. Different types of  $\text{Si}_3\text{N}_4$  materials can be produced by changing the starting powders, types and amounts of additives and manufacturing processes. These properties make them prime candidate materials for structural applications at ambient and high temperatures. Table 2-IX presents the time evolution of  $\text{Si}_3\text{N}_4$  with regard to its application [2].

*Table 2-IX : Time evolution of  $\text{Si}_3\text{N}_4$  from chemical compound to an advanced ceramic.*

Year	Development-with regard to $\text{Si}_3\text{N}_4$
1830	Diimide synthesis
1859	Direct nitridation
1896	Carbothermal reduction of $\text{SiO}_2$
1910	Chemical formula
1950	Reaction bonded parts
1955	First application as refractories
1957	Crystal structure
1961	Fully dense bodies (hot pressed material)
1971	$\beta$ -SiAlON
1976	Liquid phase sintering (LPS)
1977	Gas pressure sintering (GPS)
1978	$\alpha$ -SiAlON
1979	Cutting tools
1981	Components for engines
1985	Turbo charger rotors
1993	Valves
1996	Components for aircraft
1999	$\gamma$ - $\text{Si}_3\text{N}_4$
2000	Valve plate for common rail systems
2001	Cooking plates

Further improvement of the material properties, lower cost and collaboration between ceramic producers and industrial use is expected to create new fields of applications with a higher acceptance of  $\text{Si}_3\text{N}_4$  on the market.

## 2.12 Motivation

In spite of the excellent properties of  $\text{Si}_3\text{N}_4$  based ceramics, their widespread use is still limited, the main reason being the cost factor with respect to:

1. Raw materials ( $\text{Si}_3\text{N}_4$  powders)
2. Raw materials (additives)
3. Production processes

The motivation for this work is to improve the economic viability of silicon nitride products by way of lowering the cost of starting materials and lowering the sintering temperature. Additives that satisfy these criteria are from the  $\text{Li}_2\text{O}-\text{Y}_2\text{O}_3$  and  $\text{Li}_2\text{O}-\text{Al}_2\text{O}_3-\text{SiO}_2$  systems. The reasons for their suitability as sintering additives are as follows:

1. Lithia and yttria have been effective single component additives. Experimental evidence confirms this assumption [131]. Hence, a mixed oxides from both system should as well be useable as an additive.
2.  $\text{Li}_2\text{O}$  reduces the viscosity of the liquid phase and thus minimises the total amount of additive needed for sintering.
3. Yttrium is insoluble in  $\text{Si}_3\text{N}_4$ , while lithium dissolves only when both aluminum and oxygen are present [132]. This means that  $\text{Li}_2\text{O}$  and  $\text{Y}_2\text{O}_3$  are localized in grain-boundary phases and do not change the local covalency of  $\text{Si}_3\text{N}_4$ .
4. In the case of the  $\text{Li}_2\text{O}-\text{Al}_2\text{O}_3-\text{SiO}_2$  system, due to solubility of Li and Al in  $\text{Si}_3\text{N}_4$ , one can expect the formation of a sintered material with only a small amount of residual glassy phase at the grain boundaries resulting in an improved temperature resistance at intermediate temperatures [133].

### 3 EXPERIMENTAL PROCEDURE

The experimental part of this study was designed in order to provide information on the sintering and microstructural evolution and mechanical properties of the  $\text{Si}_3\text{N}_4\text{-LiYO}_2$  and  $\text{Si}_3\text{N}_4\text{-Li}_2\text{O-Al}_2\text{O}_3\text{-SiO}_2$  systems.

The first group of experiments deal with the additive preparation and characterization of the starting material. The second group of experiments are focused on following the sintering kinetics and microstructural evolution in the aforementioned systems. The objectives are (a) to acquire experimental data on density as a function of temperature, time and heating rate and (b) to analyse the key microstructural features and their evolution during the course of sintering.

The last group of experiments are focused on the mechanical and thermo-mechanical characterisation of the material and on correlating phase composition, microstructure and mechanical properties.

The experimental procedure of the present study is summarised in the flow chart (Fig. 3.1).

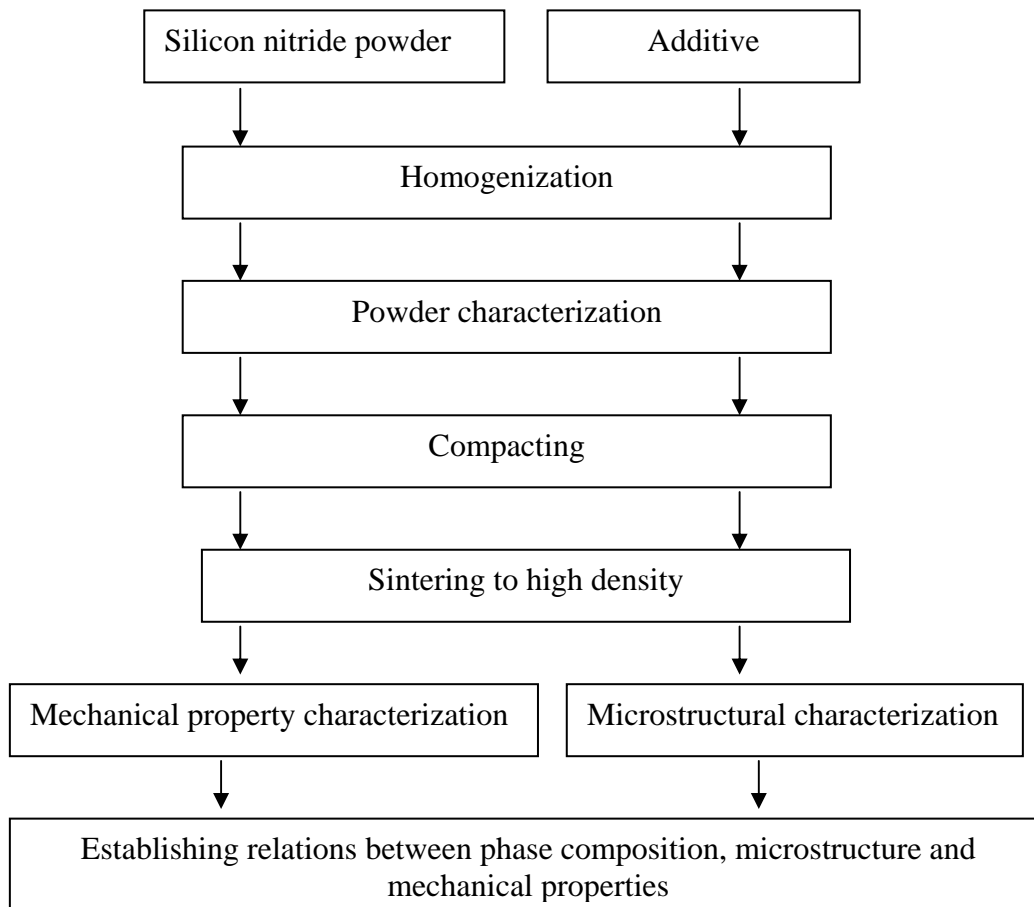


*Fig. 3.1 : Flow chart of the experimental procedure.*

### 3.1 Characterization

The starting materials used in this study were commercial Si<sub>3</sub>N<sub>4</sub> powder (Silzot HQ, SKW-Trostberg AG) and self-made additives namely LiYO<sub>2</sub> and Li-exchanged zeolite. All starting materials were characterized in terms of their particle size distribution, specific surface areas, phase composition, chemical analysis and particle morphology.

#### 3.1.1 Specific surface area and particle size distribution

Particle size distributions were measured by laser granulometry. Specific surface areas were measured using the BET technique (Gemini, Micromeritics). Helium was used as the purging gas and nitrogen as the adsorbed gas.

#### 3.1.2 X-ray diffraction

The crystalline phases present in the raw powders, mixtures and sintered ceramics were identified by X-ray powder diffraction using a Siemens diffractometer model D5000 Kristalloflex (Ni-filtered Cu K<sub>α</sub> radiation; λ = 1.5406 Å). The X-ray tube was operated at 40 kV and 20 mA. Diffractographs of the samples were recorded over the 2θ range from 10° up to 80° at a scanning rate of 2°/min using a position-sensitive detector with 8° acceptance angle. For phase analysis, the software Diffrac AT was used. XRD was also used for quantitative evaluation of the weight fraction of the α-Si<sub>3</sub>N<sub>4</sub> and β-Si<sub>3</sub>N<sub>4</sub> phases by calculations based on of the method proposed by Gazzara and Messier [134]:

$$\beta - Si_3N_4 (wt\%) = \frac{I_{\beta(101)} + I_{\beta(210)}}{I_{\alpha(102)} + I_{\alpha(210)} + I_{\beta(101)} + I_{\beta(210)}} \quad (3.1)$$

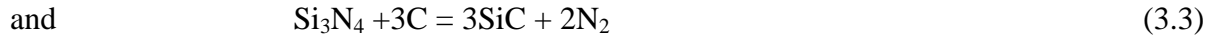
where I<sub>β(101)</sub> and I<sub>β(210)</sub> are the diffraction intensities of the (101) and (210) planes of β-Si<sub>3</sub>N<sub>4</sub> and I<sub>α(102)</sub> and I<sub>α(210)</sub> represent the intensities of (102) and (201) planes of α-Si<sub>3</sub>N<sub>4</sub>.

#### 3.1.3 Chemical analysis

For nitrogen and oxygen determination, an elemental analyser (Leco TC-436 DR) was used. The analysis was done by carrier gas hot extraction: the sample was weighed into a Ni capsule to which about 50 mg of material was added. The capsule was then transferred to a graphite



crucible, which was heated to about 2500°C. The sample decomposes in the Ni melt according to the reactions:



The gases formed are transported with the carrier gas helium to the detection systems. CO or CO<sub>2</sub> (after oxidation of CO to CO<sub>2</sub>) are detected and quantified using a IR-cell, and N is detected by a thermal conductivity detector.

Chemical analysis by inductively coupled plasma-optical emission spectrometry (ICP-OES, Spectro, Germany) was used to quantify the Li content of samples after various heat treatments.

#### ***3.1.4 Scanning electron microscopy***

In order to observe the powder morphology, scanning electron microscopy (SEM) was employed. SEM analyses were also carried out on polished and plasma etched surfaces of samples using a JEOL 6300F microscope at 3 kV accelerating voltage. For this purpose, the specimens were mirror polished to 1 μm and carbon coated in order to avoid charging effects. The backscattered electron mode was used to examine the homogeneity of the additive distribution in the green compacts. The green compacts were coated with carbon to make their surfaces conductive. Because of the difference in atomic number, the additives appear in a differential contrast when the imaging mode is used.

### **3.2 Results**

#### ***3.2.1 Starting material***

The Si<sub>3</sub>N<sub>4</sub> powder Silzot HQ is a low cost powder produced by a special modification of the direct nitridation method from a high purity grade of silicon. Chemical analysis of the powder was provided by the manufacturer. Characteristic impurity contents are given in Table 3-I. The micrographs depicted in Fig. 3.2 show that the Si<sub>3</sub>N<sub>4</sub> powder is coarse grained with a broad

Table 3-I : Characteristic analysis of as-received Silzot HQ  $\text{Si}_3\text{N}_4$  powder.

N	>38.5 wt %
Si free	<0.5
SiC	<0.4
Al	<0.1
Fe	<0.04
Ca	<0.02
O	$\approx 0.5$
$\alpha/(\alpha+\beta) - \text{Si}_3\text{N}_4$	0.8
Specific surface area ( $\text{m}^2/\text{g}$ )	3.2
Density ( $\text{g}/\text{cm}^3$ )	3.2
Mean particle size ( $d_{50}-\mu\text{m}$ )	1.7

particle size distribution. Different morphologies of the particles like equiaxed, rod-like end even needle-shaped particles can be identified clearly.

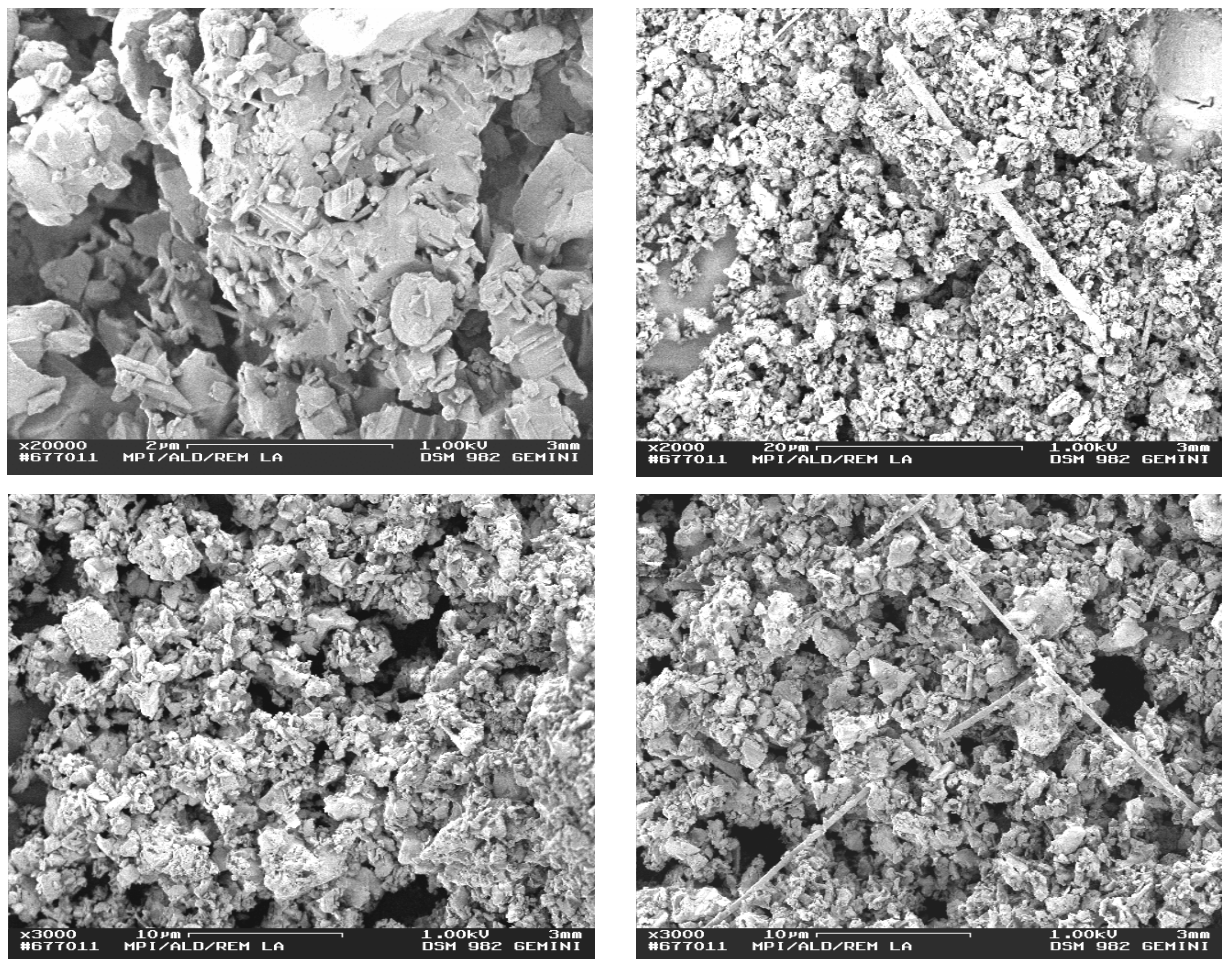
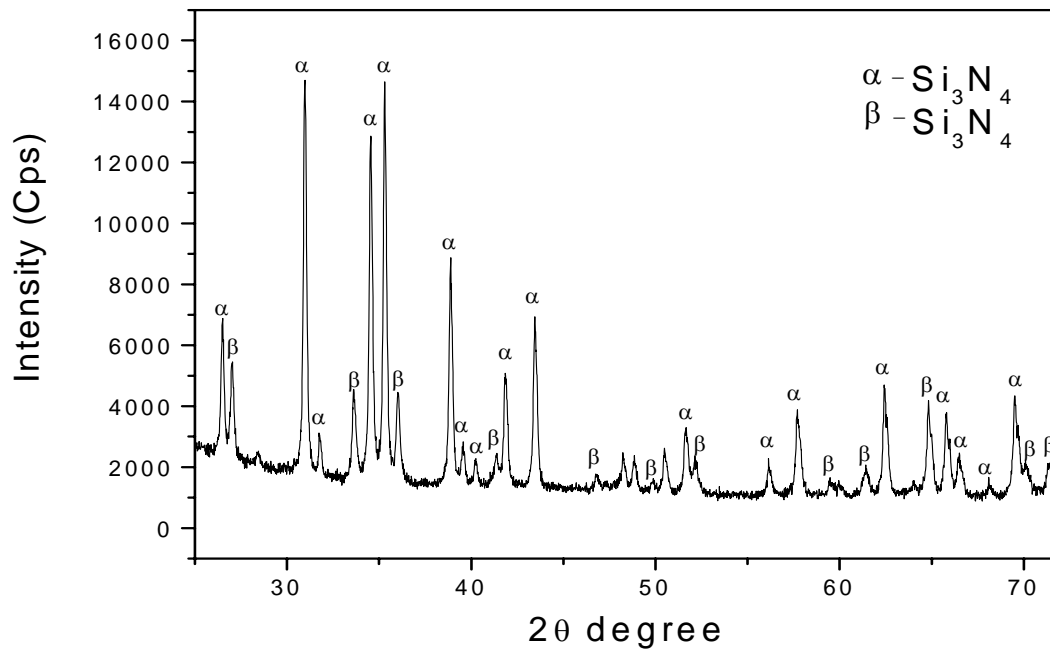


Fig. 3.2 : Typical Scanning electron micrographs of as-received silicon nitride powder.

The XRD pattern of Silzot HQ  $\text{Si}_3\text{N}_4$  powder shows the presence of only  $\alpha$ - $\text{Si}_3\text{N}_4$  and  $\beta$ - $\text{Si}_3\text{N}_4$  phases (Fig. 3.3). Thus, the as-received  $\text{Si}_3\text{N}_4$  powder was found to be free from other impurities such as elemental silicon, which is very often present in powders obtained by direct nitridation of silicon. According to quantitative analysis of the XRD pattern, the  $\beta$ - $\text{Si}_3\text{N}_4$  content in the raw powder is nearly 20%.



*Fig. 3.3 : XRD pattern of as-received Silzot HQ  $\text{Si}_3\text{N}_4$  powder.*

### 3.3 Additive preparation

The sintering additives used in the present work are  $\text{LiYO}_2$  and Li-exchanged zeolite.  $\text{LiYO}_2$  was synthesized by mixing as-received  $\text{Y}_2\text{O}_3$  and  $\text{Li}_2\text{CO}_3$  powders and calcining the mixture at  $1400^\circ\text{C}$ . The XRD pattern revealed the monophase composition (Fig. 3.4.a) with well developed tetragonal crystal habitus (Fig. 3.4.b).

A sodium form of A-zeolite, Birach Co., Bosnia, was used as the precursor material for obtaining the additive from the  $\text{Li}_2\text{O}-\text{Al}_2\text{O}_3-\text{SiO}_2$  system. Completely exchanged Li-forms of the zeolite were prepared after several steps of cation exchange with an aqueous solution of  $\text{LiCl}$  at  $80^\circ\text{C}$ .

The dried powder was heated at 800°C to cause a collapse of the zeolite structure, with the simultaneous formation of an amorphous product with a composition corresponding to  $\text{Li}_2\text{O}\cdot\text{Al}_2\text{O}_3\cdot 2\text{SiO}_2$ . By annealing at a higher temperature (1000°C), the amorphous powder

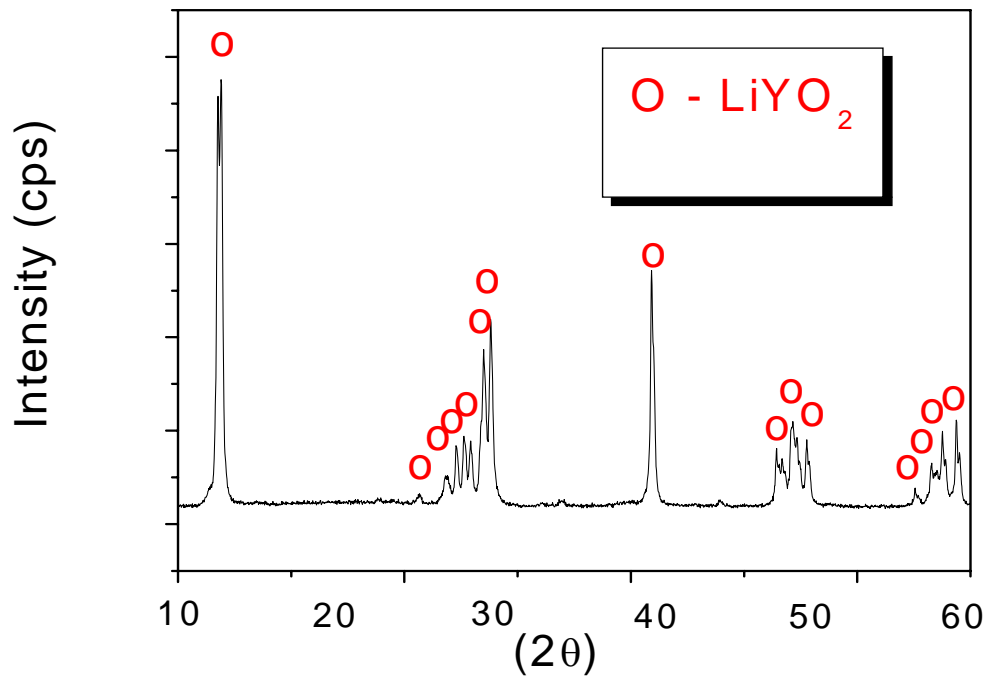


*Fig. 3.4(a) : XRD pattern of synthesized LiYO<sub>2</sub> additive.*

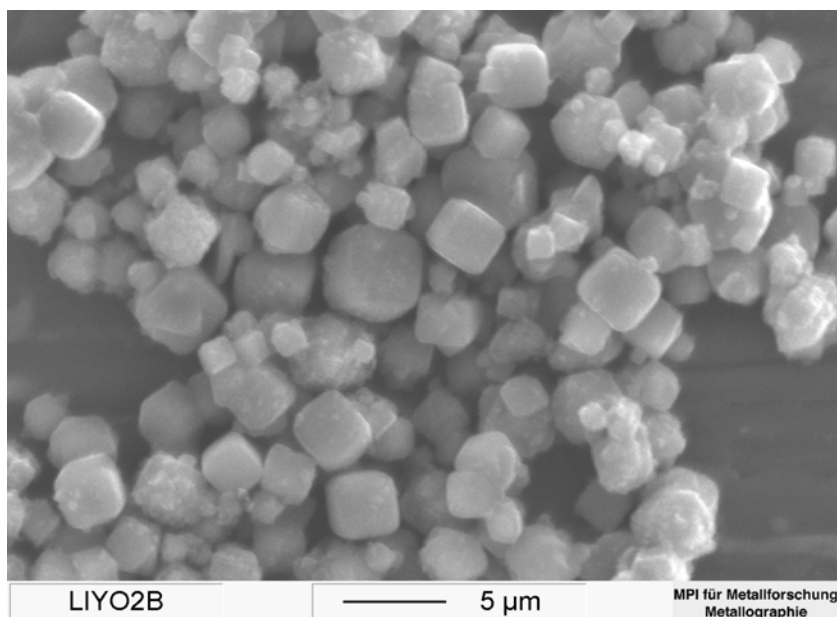


*Fig. 3.4(b) : SEM micrograph of synthesized LiYO<sub>2</sub> additive.*

crystallizes to  $\beta$ -eucryptite (Fig. 3.5). Due to its high reactivity, the amorphous powder is used as the additive.

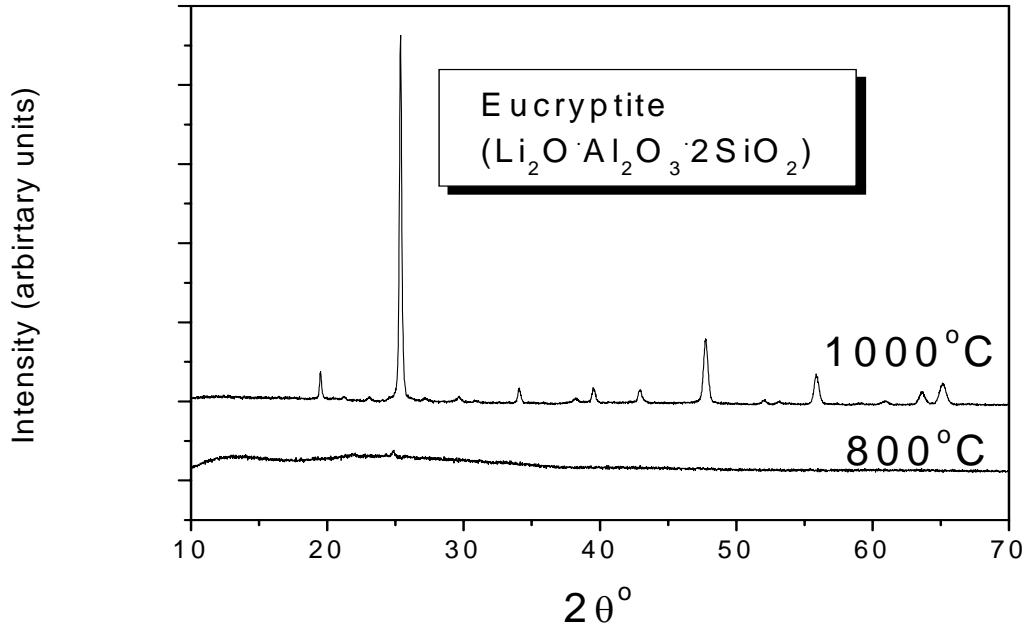


*Fig. 3.5 : XRD pattern of Li-exchanged zeolite at 800 and 1000 °C.*

### 3.4 Greenbody fabrication

The preparation method for  $\text{Si}_3\text{N}_4$  with  $\text{LiYO}_2$  additive is schematically represented in Fig. 3.6.

Powder mixtures with 5, 10, 15 and 20% of  $\text{LiYO}_2$  additive were prepared by vibratory milling, ball milling or attrition milling in isopropanol for different times using  $\text{Si}_3\text{N}_4$  milling media. One batch was mixed in a vibratory mill without any fluid medium. The slurry was separated from the dispersion medium in a rotating vacuum evaporator. Completely dried powders were obtained after 16 h at 65 °C in a drying oven. They were subsequently sieved to obtain granules with a maximum size of 160  $\mu\text{m}$ . Green body compaction was done by cold isostatic pressing. The premixes were encapsulated within rubber dies and pressed at a pressure of 240 MPa.

Powders with the  $\text{LiYO}_2$  additive were processed with all combinations of the above three milling treatments. The optimal sequence (attrition milling, see chapter 4) was chosen for later experiments with  $\text{LiYO}_2$  as well as for preparing mixtures with Li-exchanged zeolite additive.

Compositions with 5, 10, 15 and 20% of Li-exchanged zeolite additives were also prepared, but only attrition milling was used for homogenization.

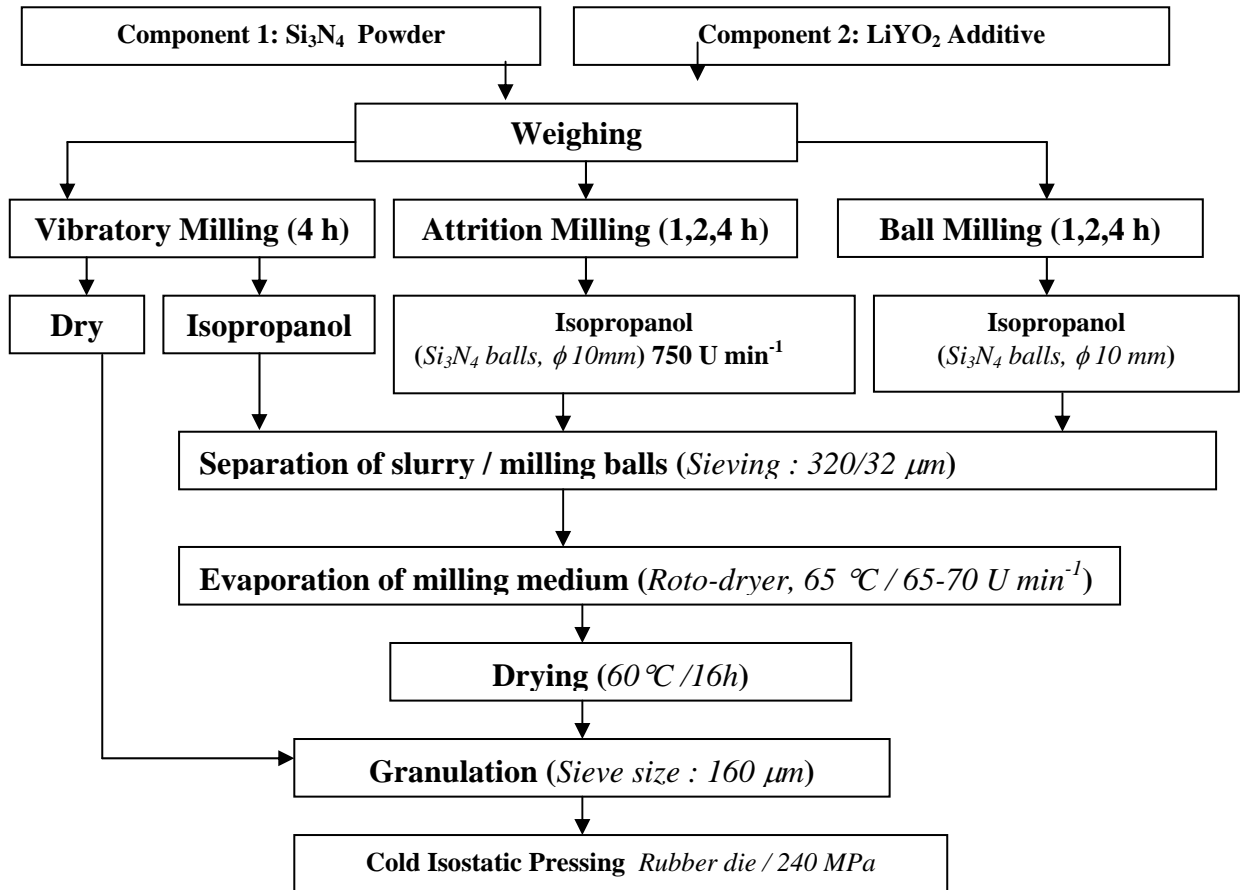


*Fig. 3.6 : Schematic diagram of sample preparation method.*

### 3.4.1 High temperature thermogravimetry

In order to investigate the stability of powder mixtures at high temperatures, thermogravimetry measurements (TG) were performed up to 1700°C. Measurements were made in nitrogen atmosphere using a graphite crucible with a heating rate of 10 K/min.

### 3.4.2 Dilatometry

Pushrod dilatometry was used to study the shrinkage behaviour of green bodies under a flowing nitrogen atmosphere at a heating rate of 5 K/min from room temperature to 1500°C. After dwell times of 5 and 480 min at the maximum temperature as well as at temperatures

corresponding to characteristic points of the shrinkage curve, the dilatometer furnace was switched off for rapid cooling.

### 3.5 Sintering

Sintering was done in a gas pressure furnace (FCT, Germany) with graphite heating elements in a nitrogen atmosphere at different temperatures and dwell times. A schematic diagram of the sintering experiments is shown in Fig. 3.7.

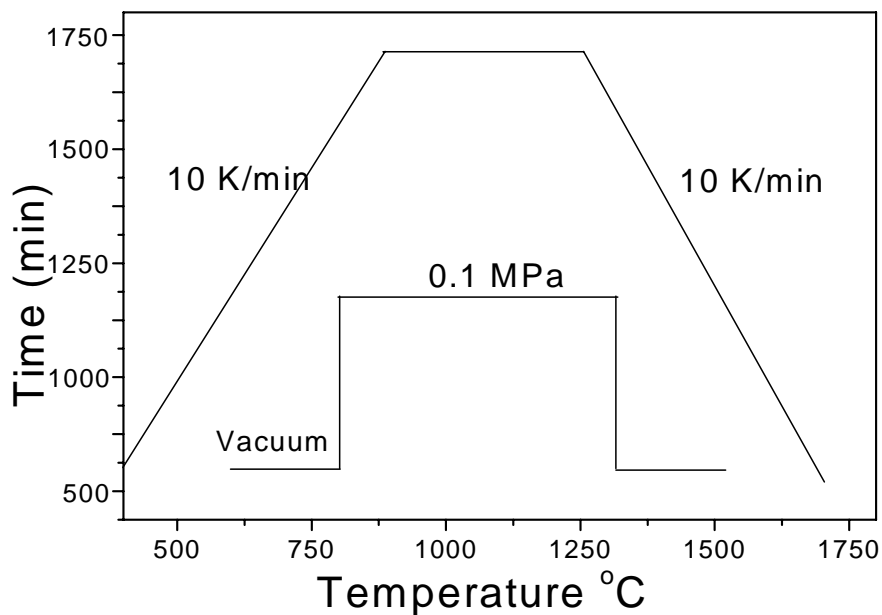


*Fig. 3.7 : Schematic diagram of sintering schedule.*

The samples were placed in a cylindrical graphite crucible which was placed in the heating zone of the furnace. The furnace was then closed and the heating chamber was evacuated. The first stage of heating was carried out in vacuum till 800°C and after that under a pressure of 0.1 MPa. The specimens intended for isothermal sintering were heated with a rate of 10 K/min to a sintering temperature in the range of 1500-1700°C at which they were held for 5 - 480 minutes and then cooled with a rate of 10 K/min.

### 3.5 Characterization of the ceramics

#### 3.5.1 Sintered density and mass loss

The sintered densities were measured by Archimedes' principle (water displacement):

$$\rho_S = \frac{m_S \cdot \rho_W}{m_S - m_W} \quad (3.4)$$

Where  $\rho_S$  = sintered density ( $\text{g/cm}^3$ ),  $\rho_W$  = density of water at room temperature ( $\approx 1 \text{ g/cm}^3$ ),  $m_S$  = mass of the sintered body in air (g) and  $m_W$  = mass of the sintered body in water (g).

Green densities were measured by weighing the samples and measuring their linear dimensions with a micrometer screw.

The relative densities ( $\rho_{\text{rel}}$ ) were calculated by dividing the sintered densities ( $\rho_S$ ) by the theoretical density ( $\rho_{\text{th}}$ ). The theoretical density was calculated based on the rule of mixture, i.e. the relative density was calculated based on the theoretical density of each individual constituent and its content.

Mass losses ( $\Delta m$ ) of the specimens were measured by using the following formula:

$$\Delta m = \frac{m_G - m_S}{m_G} \cdot 100 \quad (3.5)$$

where  $m_G$  = mass of the green body.

#### 3.5.2 Room temperature fracture toughness

Fracture toughness ( $K_{IC}$ ) was determined by using the indentation method. After polishing to a  $1 \mu\text{m}$  finish, 12 Vickers indentations per specimen are introduced under a load of 50 N. A formula valid for semi-circular crack systems [135] was used to calculate  $K_{IC}$  from the lengths of edge cracks and indentation diagonals:

$$K_{IC} = 0.016 \cdot \sqrt{\frac{E}{H}} \cdot F \cdot L^{\frac{3}{2}} \quad (3.4)$$



where  $E$  = Young's modulus, taken as 300 GPa for  $\text{Si}_3\text{N}_4$  ceramics,  $H$  = Vickers hardness (GPa).  $F$  = Load (N),  $L$  = Crack length ( $\mu\text{m}$ ) (Fig. 3.8).

From the same experiments, the hardness is calculated by the formula given below :

$$H = 1.8544 \cdot \frac{F}{d_H^2} \quad (3.5)$$

where  $d_H$  = diagonals of Vickers indentation ( $\mu\text{m}$ ).

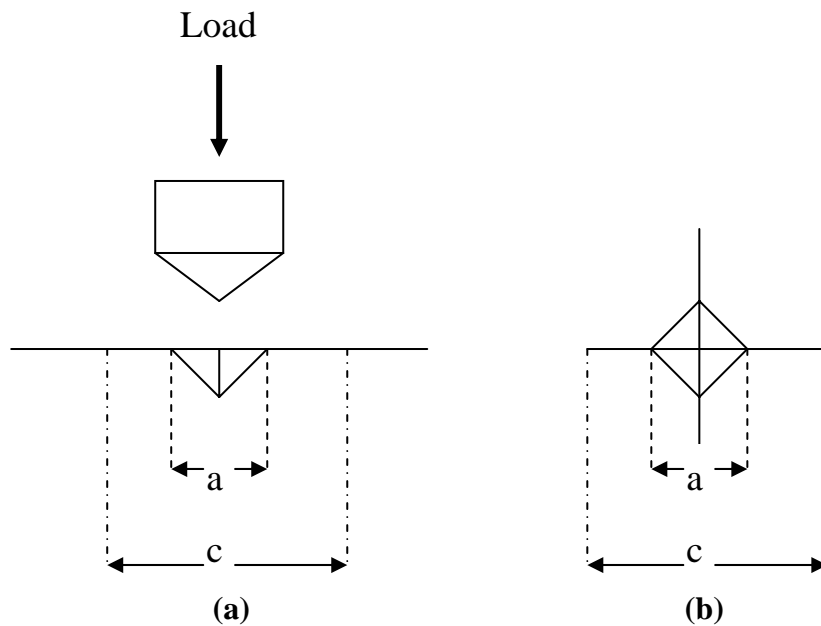


**Fig. 3.8 :** A schematic view of the Vickers' microhardness test, (a) cross-sectional view, (b) top view.

### 3.5.3 Determination of thermal conductivity

The laser-flash method was used for measuring the thermal diffusivity of  $\text{Si}_3\text{N}_4$  materials. A disk sample (diameter 1.2 mm and thickness 0.5 mm) is tested in a in-house constructed laser-flash equipment. On the front face of the sample a laser-pulse (1.06  $\mu\text{m}$  wavelength and pulse duration 1 ms) is homogeneously absorbed. On the rear face the temperature rise is measured and allows the determination of the thermal diffusivity. The method has a standard deviation of 3% for reference materials. The experimental set up is given in Fig. 3.9.

The equipment (Fig. 3.9) uses a longitudinal heat pulse method. The heat source is a pulsed Nd-YAG Laser (max. 55 J/pulse). The temperature response signal at the rear of the sample is detected by an In-Sb IR detector. The amplified signal is evaluated by a computer software.

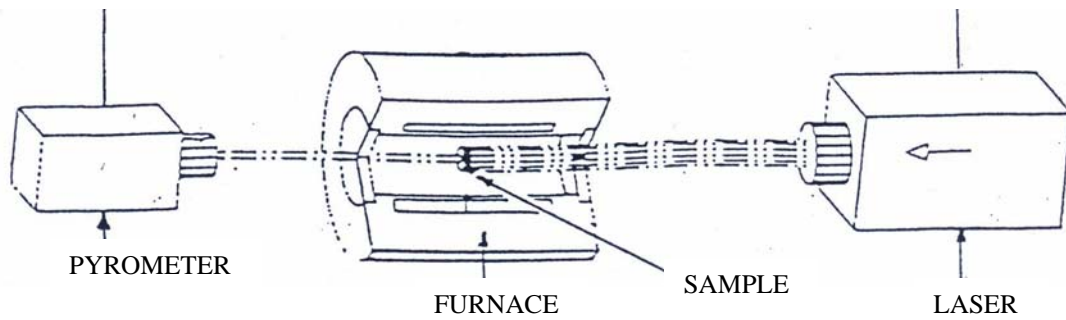


**Fig. 3.9 :** Experimental set up for measurement thermal diffusivity.

To protect the sample against heat loss, the specimen holder is installed in a vacuum chamber ( $p < 10^{-1}$  Pa). A Mo-furnace allows measurements between RT and 2000 K.

The thermal conductivity was calculated from the tabulated heat capacity,  $C_p$  of  $\text{Si}_3\text{N}_4$  [136], the thermal diffusivity,  $\alpha$ , as measured by the laser-flash technique, and the bulk density of the material,  $\rho$ , according to the equation:

$$K = C_p \cdot \alpha \cdot \rho \quad (3.6)$$

Figure 3.10 shows a typical measured curve of the temperature rise on the back side of a  $\text{Si}_3\text{N}_4$  sample.

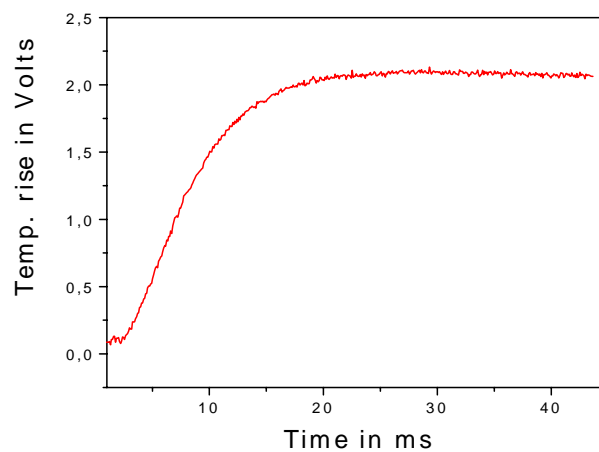


**Fig. 3.10:** Typical curve from thermal diffusivity measurement of  $\text{Si}_3\text{N}_4$  ceramics at ambient temperature.

## 4 POWDER PROCESSING

The introduction of sintering additives is a critical step in the production process. Inhomogeneities introduced at any stage before sintering remain inside the material and degrade the mechanical properties and reliability of  $\text{Si}_3\text{N}_4$  based ceramics. Therefore, in order to produce materials with optimum properties it is important to find powder processing routes able to produce high homogeneity in powder premixes/mixtures.

Various preparation routes for engineering ceramics powders have been used. The best results are obtained by chemical routes, but this method is more costly in terms of industrial manufacturing than conventional milling techniques [137]. Milling is the most common and industrially preferred method of adding and mixing the additives with the matrix [138].

This chapter deals with an investigation of the effects of different types of homogenization procedures (ball milling, attrition milling and vibratory milling) on the properties of  $\text{Si}_3\text{N}_4$  powder and sintered bodies.

Powders with favorable pressing and sintering characteristics are distinguished by a high percentage of the  $\alpha\text{-Si}_3\text{N}_4$  phase (>90%), high surface area, narrow particle size range, low content of impurities (Fe, C, Al, Ca, O) and equiaxed grain morphology [11]. In contrast, as-received Silzot HQ is a coarse grained powder with a broad particle size distribution (chapter 3., Fig. 3.2 depicts the powder morphology). Equiaxed, rod-like and even needle-shaped particles can be clearly identified. The presence of these particles leads to a decreasing compactibility and hence to low green density. Therefore, the as-received  $\text{Si}_3\text{N}_4$  powder could be pressed to only about 50% of the theoretical density.

This powder morphology is connected with a low specific surface area and with low oxygen content (chapter 3, Table III-1).

According to the above mentioned criteria, raw Silzot HQ powder is not considered to be a well sinterable powder. During the homogenization by milling several processes are occurring simultaneously. The surface of the powder increases owing to the deglomeration and to the grinding of the crystallites. As a result, the oxygen content increases [139].

Table IV-I shows the effects of milling time and method of dispersion on the characteristics of the  $\text{Si}_3\text{N}_4$  powder. The specific surface area increases for all types of homogenization, but it is most pronounced in attrition milled mixtures (Fig. 4.1).

Table IV-I : Effects of milling time and different types of homogenization procedures on the properties of  $\text{Si}_3\text{N}_4$  mixtures.

Homogenization	Time (h)	Specific surface area ( $\text{m}^2/\text{g}$ )	Content of Oxygen (wt%)	Increase of oxygen content (wt%)
Ball milling	1	5.46	2.82	1.01
Ball milling	2	5.61	2.87	1.06
Ball milling	4	6.35	3.31	1.50
Attrition milling	1	6.83	2.73	0.92
Attrition milling	2	8.99	2.89	1.08
Attrition milling	4	13.78	3.67	1.86
Vibratory milling (dry)	4	4.71	2.36	0.55
Vibratory milling (alcohol)	4	12.26	3.98	2.17

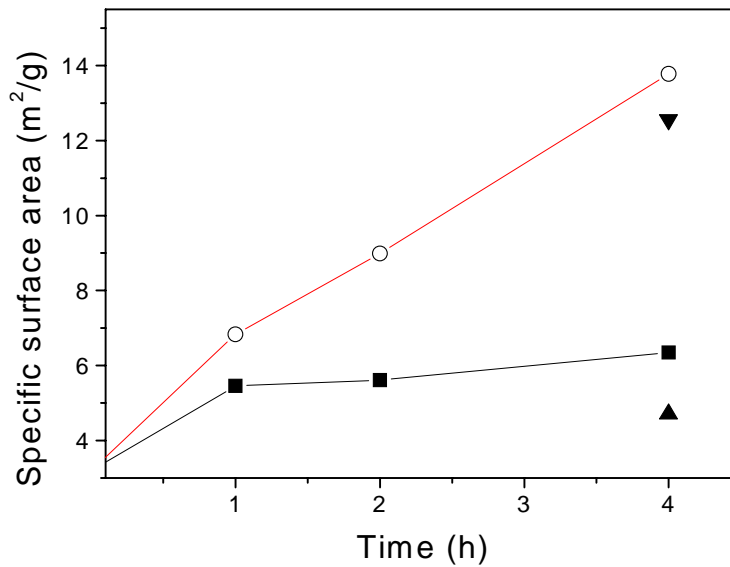
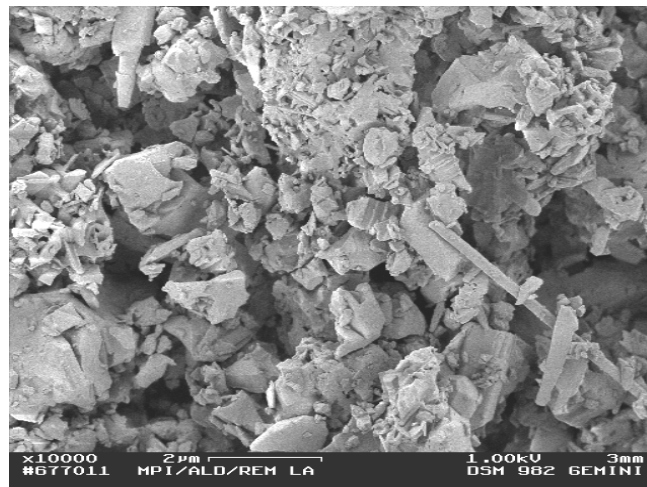


Fig. 4.1 : The effects of milling time on the specific surface area (■ - ball milling; μ - attrition milling; σ - dry vibratory milling; τ - alcohol vibratory milling).

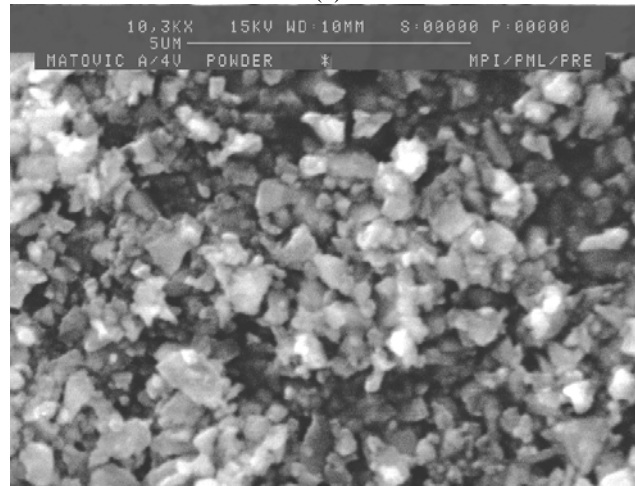
For planetary-milled mixtures, the specific surface area was significantly increased after the first hour of milling, while upon prolonged milling it stays nearly constant. In the case of attrition-milled powders, the surface area continues to grow during prolonged milling and increases by more than  $10 \text{ m}^2/\text{g}$  after 4 h of processing, as compared with the as-received  $\text{Si}_3\text{N}_4$  powder. Vibratory milling in alcohol shows very good results, but for dry vibratory milling the increase in specific surface area is less than for all other processing methods.

The increase in specific surface area is due to grinding of the crystallites. Fig. 4.2 illustrates the change in particle morphology after attrition milling in comparison with as-received

powder. Rod-like and needle-shaped particles disappear, and all particles have an equi-axed shape. This has positive effects on powder compaction.



(a)



(b)

**Fig. 4.2 :** SEM photomicrographs of as-received  $\text{Si}_3\text{N}_4$  (a) and a powder attrition milled for 4 h (b).

Table IV-I shows that during all milling procedures the oxygen content increased significantly with milling time. This is very important because for a given additive system the amount and the composition of the melt depend on the oxygen content in the  $\text{Si}_3\text{N}_4$  powder. Higher oxygen contents result in an increased amount of liquid phase and thus in an enhancement of the particle rearrangement and the diffusion processes. For the coarser-grained powders this effect is more significant. An oxygen content of at least 1.5% is necessary for high densification [11]. Fig. 4.3 shows the oxygen content as a function of the presence of the sintering additive and the milling procedure used. The overall oxygen content was calculated as the sum of oxygen from the sintering additive (5 wt %  $\text{LiYO}_2$ ) and the oxide layer on the surface of the  $\text{Si}_3\text{N}_4$  powder. The highest increase was obtained for attrition milling (4 h) and

vibratory milling (4 h in alcohol), which corresponds well with the increase specific surface area.

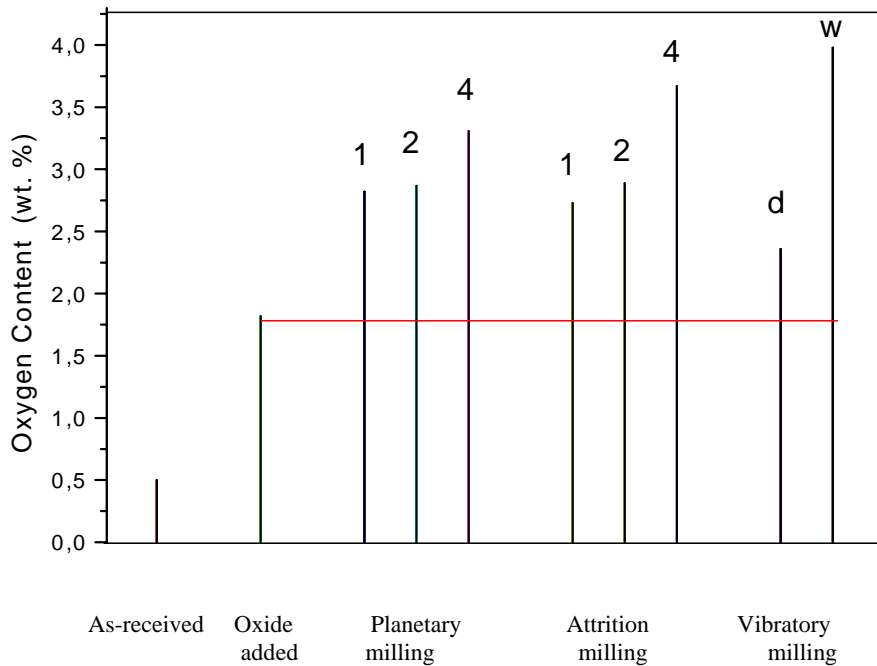


**Fig. 4.3 :** Oxygen content during processing with  $\text{LiYO}_2$  additives (milled for 1,2,4 h ; d-dry milling; w-wet milling).

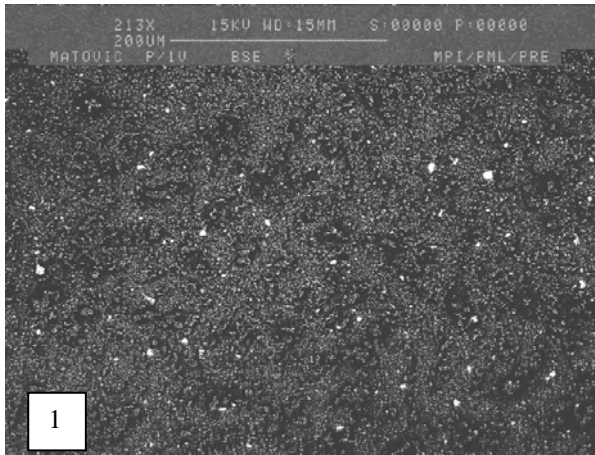
Fig. 4.4 shows the atomic number contrast mapping in different green compacts. The light spots represent the Y in  $\text{LiYO}_2$  that is distributed in the green compacts. Large spots imply an agglomeration of the additive. The number of large spots was apparently greater in the samples prepared by planetary milling, a especially for the samples milled for 1 or 2 h. Therefore, many agglomerates of the oxide additive exist in these compacts. The distribution of additives is obviously more homogenous in the compacts prepared by attrition milling than in the compacts prepared by planetary milling.

A confirmation for the higher quality of the additive distribution is the density that is achieved after sintering (Table IV-II).

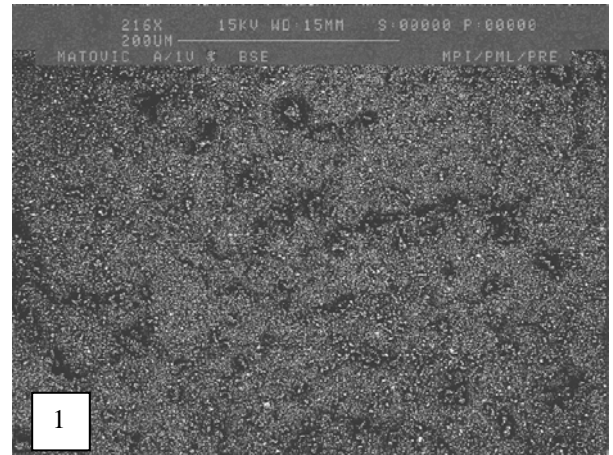
**Table IV-II :** Densities after sintering at  $1600\text{ }^\circ\text{C}$  with 5% of  $\text{LiYO}_2$  additive, (TD-theoretical density).

Time (hrs)	Ball milling		Attrition milling		Vibratory milling*	
	Density ( $\text{g/cm}^3$ )	TD (%)	Density ( $\text{g/cm}^3$ )	TD (%)	Density ( $\text{g/cm}^3$ )	TD (%)
1	2,35	73,3	2,58	80,5		
2	2,57	80,2	2,68	83,6		
4	2,56	79,9	2,92	91,1	2,94	91,6

\* wet milling



Ball milling

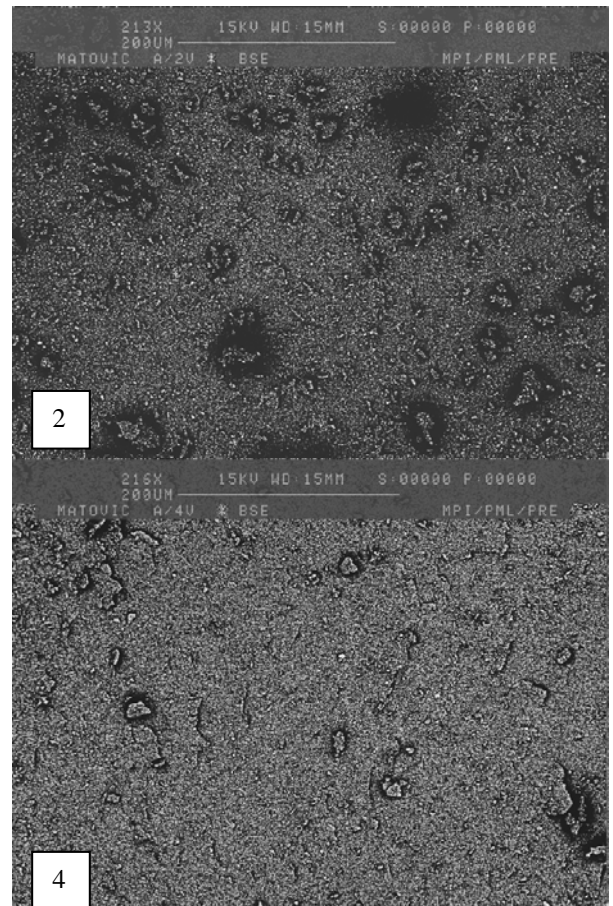


Attrition milling

**Fig. 4.4. (a) :** Backscattered electron images of green compacts showing the Y distribution ( $\text{LiYO}_2$  containing  $\text{Si}_3\text{N}_4$  mixtures prepared by ball and attrition milling for 1h).



Ball milling

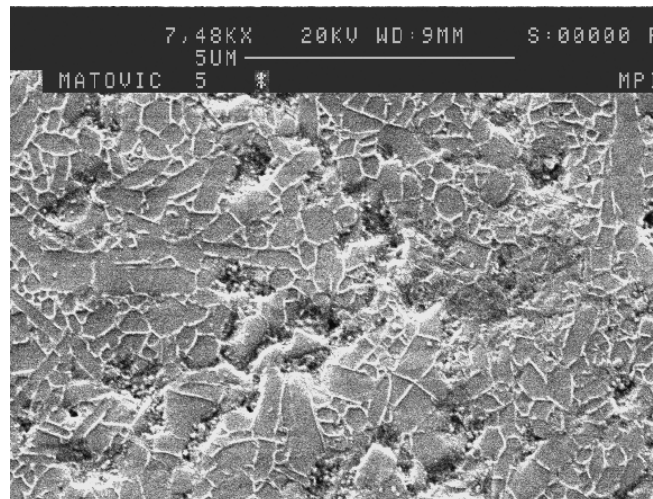


Attrition milling

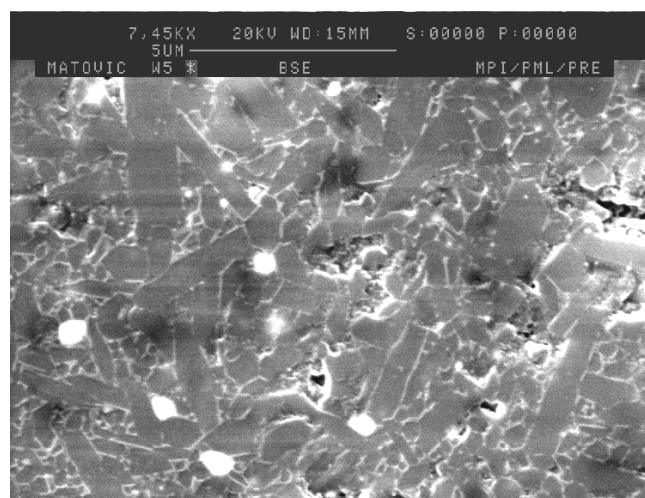
**Fig. 4.4. (b) :** Backscattered electron images of green compacts showing the Y distribution ( $\text{LiYO}_2$  containing  $\text{Si}_3\text{N}_4$  mixtures prepared by ball and attrition milling for 2 and 4 h). The light spots represent the additive that is distributed in the green compacts.

The sintered density after one hour of attrition milling is as high as after 2 and 4 h of planetary milling. With prolonged milling time attrition-milled samples increase in their density. After 4 hours of milling, a sintered density of 91% of the theoretical density is achieved. Comparable results are obtained for vibratory milled powders (wet milling). However, during vibratory milling, the powder mixture was contaminated by wear debris from the milling vial (tungsten carbide).

Different microstructures of sintered bodies are obtained for different homogenization methods (attrition and vibratory milling). The material produced from attrition-milled mixtures has a finer-grained microstructure with lower aspect ratios compared to the vibratory-milled mixtures (Fig. 4.5). In spite of the higher aspect ratio of the silicon nitride



(a)



(b)

**Fig. 4.5 :** SEM micrographs of polished and plasma etched sections of the sintered samples made by different homogenization procedures (a-attrition milling and b-vibratory milling).



grains of vibratory-milled mixtures, the presence of WC deteriorates the high-temperature strength due to its thermal decomposition and the oxidation of tungsten.

In conclusion, using three different mechanical mixing processes (attrition milling, ball milling and vibratory milling) for the introduction of additives ( $\text{LiYO}_2$ ) in  $\text{Si}_3\text{N}_4$  powder, the best results are obtained for attrition milling. This method yields a good dispersion of the additive powder in fine unagglomerated  $\text{Si}_3\text{N}_4$  without contamination. It also yields good sintering characteristics.

Vibratory milling leads to a good dispersion of the additive, but the mixture is contaminated by WC wear debris which remains inside the materials during and after sintering and may affect the properties of the ceramics.

## 5 DENSIFICATION

### 5.1 Dilatometric study

The densification behavior of  $\text{Si}_3\text{N}_4$ -based ceramics by pressureless sintering is affected directly by the characteristics of the liquid phases present. Densification is negligible before the formation of the liquid and can be improved by lowering the eutectic temperature and viscosity of the liquid phase. Hence, it is very important to find the minimum liquid-forming temperature, i. e. the effective densification temperature. However, identifying the liquid forming regions for powder compacts of the systems  $\text{Si}_3\text{N}_4$ -additive is quite complicated due to the presence of variable amounts of  $\text{SiO}_2$ , which is an inherent component of  $\text{Si}_3\text{N}_4$  powders. In order to optimize the  $\text{Si}_3\text{N}_4$ -additive material system, a series of dilatometric tests was performed.

#### 5.1.1 Densification temperature

According to the ternary diagrams for the  $\text{Li}_2\text{O}-\text{Y}_2\text{O}_3-\text{SiO}_2$  [140] and  $\text{Li}_2\text{O}-\text{Al}_2\text{O}_3-\text{SiO}_2$  [141], systems, the nominal eutectic temperature is  $1350^\circ\text{C}$  in both cases. However, due to the dissolution of  $\text{Si}_3\text{N}_4$  into the liquid phase, the overall liquid forming temperature is expected to be lower than the nominal eutectic temperature.

##### 5.1.1.1 $\text{Si}_3\text{N}_4$ - $\text{LiYO}_2$ - $\text{SiO}_2$ system

The dilatometric data (Fig. 5.1) show that shrinkage first occurs at  $1200^\circ\text{C}$  and becomes rapid at  $1275^\circ\text{C}$  in the case of samples with 15 and 20 wt% of  $\text{LiYO}_2$  additive. In case of samples with lower additive contents (5 and 10 wt%) the onset of shrinkage is retarded and its magnitude is much reduced. The onset of shrinkage can be related to liquid formation in the samples. This is in response to the melting point in the  $\text{Li}_2\text{O}-\text{SiO}_2$  system ( $1255^\circ\text{C}$ ) [142]. The shrinkage accelerates when enough liquid phase for efficient densification by particle rearrangement has been formed.

Fig. 5.2. shows the effect of additive content on the linear shrinkage of the samples after heating to  $1500^\circ\text{C}$  in dilatometer experiments. More liquid is formed as the amount of additive is increased. The maximum linear shrinkage of 11.9 % is obtained for 20 wt% of additive.

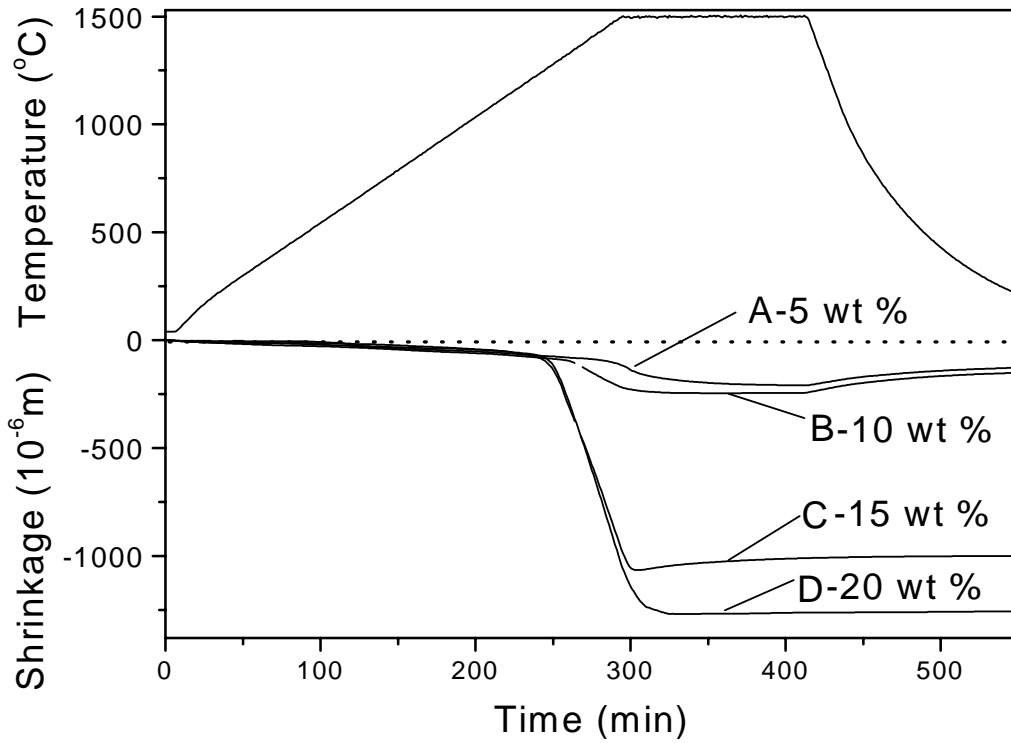


**Fig. 5.1:** Length change of  $\text{Si}_3\text{N}_4$  green bodies (A-5 wt%, B-10 wt%, C-15 wt%, D-20 wt% of  $\text{LiYO}_2$ ) between room temperature and 1500 °C. A cylinder-shaped test body was examined by dilatometry in nitrogen atmosphere.

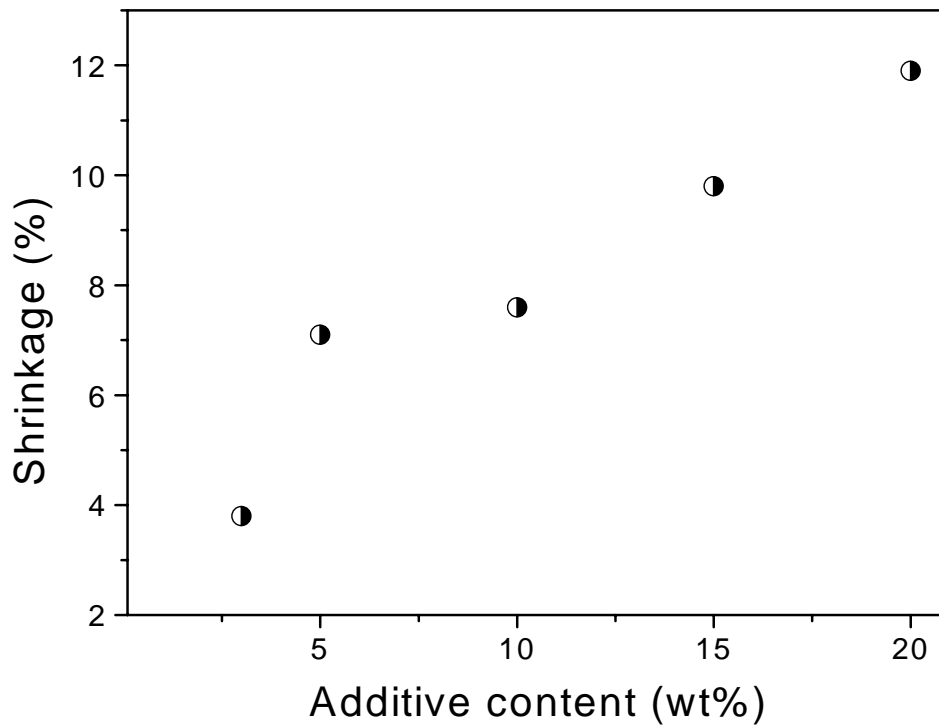


**Fig. 5.2:** Linear shrinkage versus additive content in dilatometer experiments, after a holding time of 5 min at 1500 °C.

The presence of  $\text{Li}_2\text{O}$  in the liquid leads to lower melting point and a less viscous liquid phase at a given temperature, which allows faster transport of material through the melt. The redistribution of the liquid and the filling of pores is also facilitated. This allows high density values to be reached at relatively low temperatures (Fig. 5.3). The density of samples with 15 wt% of additive is  $2.84 \text{ g/cm}^3$  at  $1300^\circ\text{C}$  and more than  $2.95 \text{ g/cm}^3$  at  $1350^\circ\text{C}$ . With prolonged heating time, differences in the degree of densification become smaller. The increment in the sintered density likewise diminishes with increased quantity of additives (Fig. 5.4).

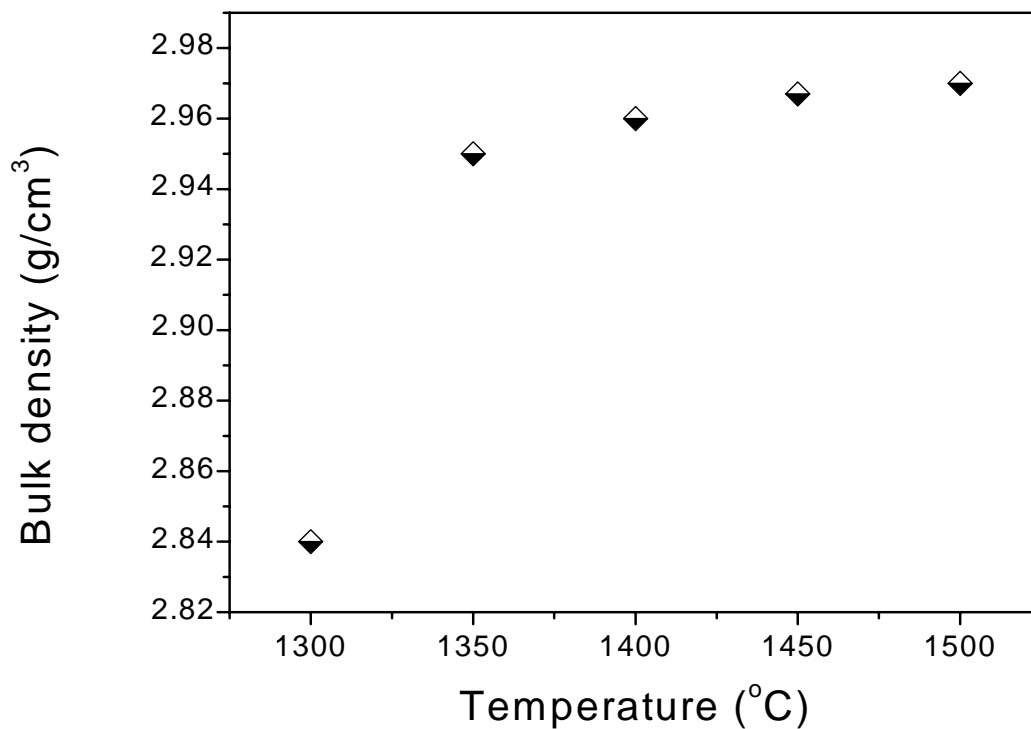


**Fig. 5.3.** Density according to dilatometric measurements of  $\text{Si}_3\text{N}_4$  with 15 wt% of  $\text{LiYO}_2$  additive after a holding time of 5 min at the temperatures indicated.

The densification of  $\text{Si}_3\text{N}_4$  ceramics is enhanced by increasing the liquid content and decreasing the liquid viscosity. The higher the  $\text{LiYO}_2$  additive content in the liquid, the higher the oxygen content and therefore the lower the viscosity of liquid phase. On the other hand, dissolution of some  $\text{Si}_3\text{N}_4$  into the liquid increases the viscosity of silicon-oxynitride glasses due to increasing nitrogen content. This also influences the shrinkage rate during densification (Fig. 5.5).

The results show that all materials were not fully dense after dilatometric measurements up to  $1500^\circ\text{C}$ . The best results were obtained for samples with 15 or 20 wt% of additive (Fig. 5.4).

In view of the materials' properties that can be expected, 15 wt% additive content may be considered as an auspicious compromise.

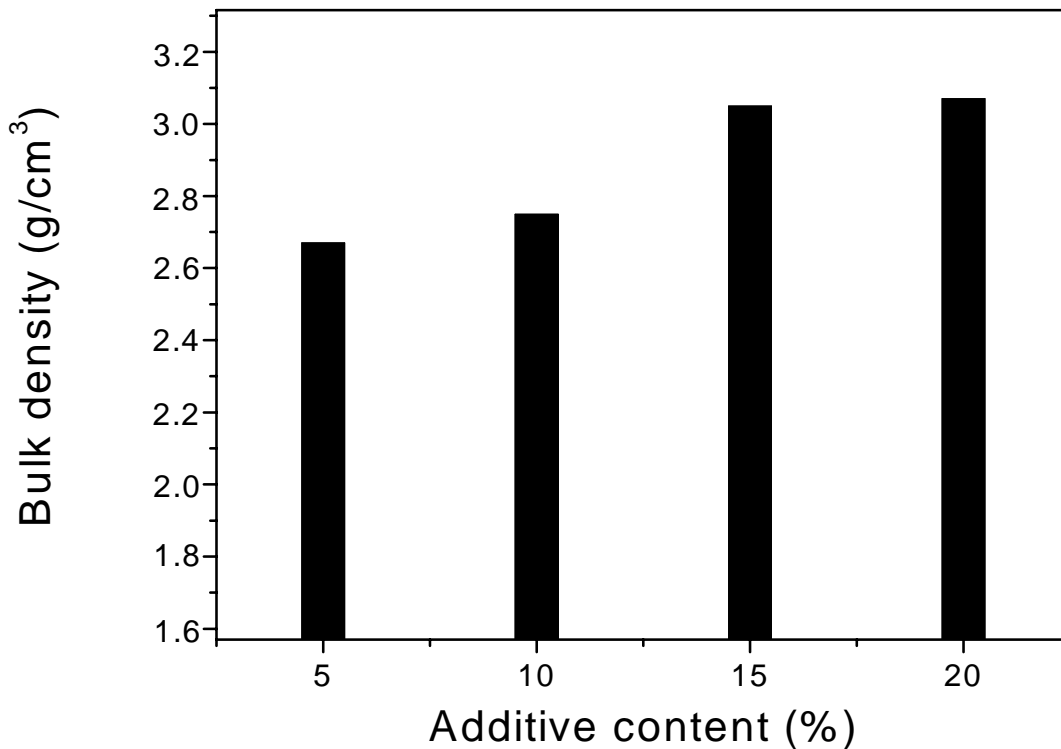


**Fig. 5.4:** Influence of the amount of  $\text{LiYO}_2$  on the densification of  $\text{Si}_3\text{N}_4$  samples fired at  $1500^\circ\text{C}$  with a holding a time of 5 min.

The change in length and rate of shrinkage are shown in Fig. 5.5 (a) and (b) respectively. It can be seen that the shrinkage curve has a sigmoidal shape. As mentioned earlier, shrinkage starts at about  $1200^\circ\text{C}$  and proceeds rapidly above  $1275^\circ\text{C}$ . The shrinkage continues during the first 30 min of isothermal annealing at  $1500^\circ\text{C}$ , after which a plateau is reached. The total linear shrinkage is about 11% immediately after reaching  $1500^\circ\text{C}$  and 12.5% after annealing for 2 h at this temperature.

The shrinkage velocity curve shows three maxima at  $1275^\circ\text{C}$ ,  $1364^\circ\text{C}$  and  $1453^\circ\text{C}$  (points 2 to 4). The appearance of the liquid in the sample starts at  $1180^\circ\text{C}$  (point 1). Point 1 agrees with the melting temperature in the  $\text{Li}_2\text{O-SiO}_2$  system [142]. The maximum at  $1275^\circ\text{C}$  (point 2) is related to an increasing amount of liquid phase, which surrounds the silicon nitride particles completely, favoring grain rearrangement [143]. The XRD pattern of the sample quenched at this temperature shows crystalline yttrium-silicon oxynitride  $\text{Y}_5(\text{SiO}_4)_3\text{N}$  (“N-apatite”) and lithium-silicon oxynitride ( $\text{LiSiNO}$ ) phases, which indicates the dissolution of some  $\text{Si}_3\text{N}_4$

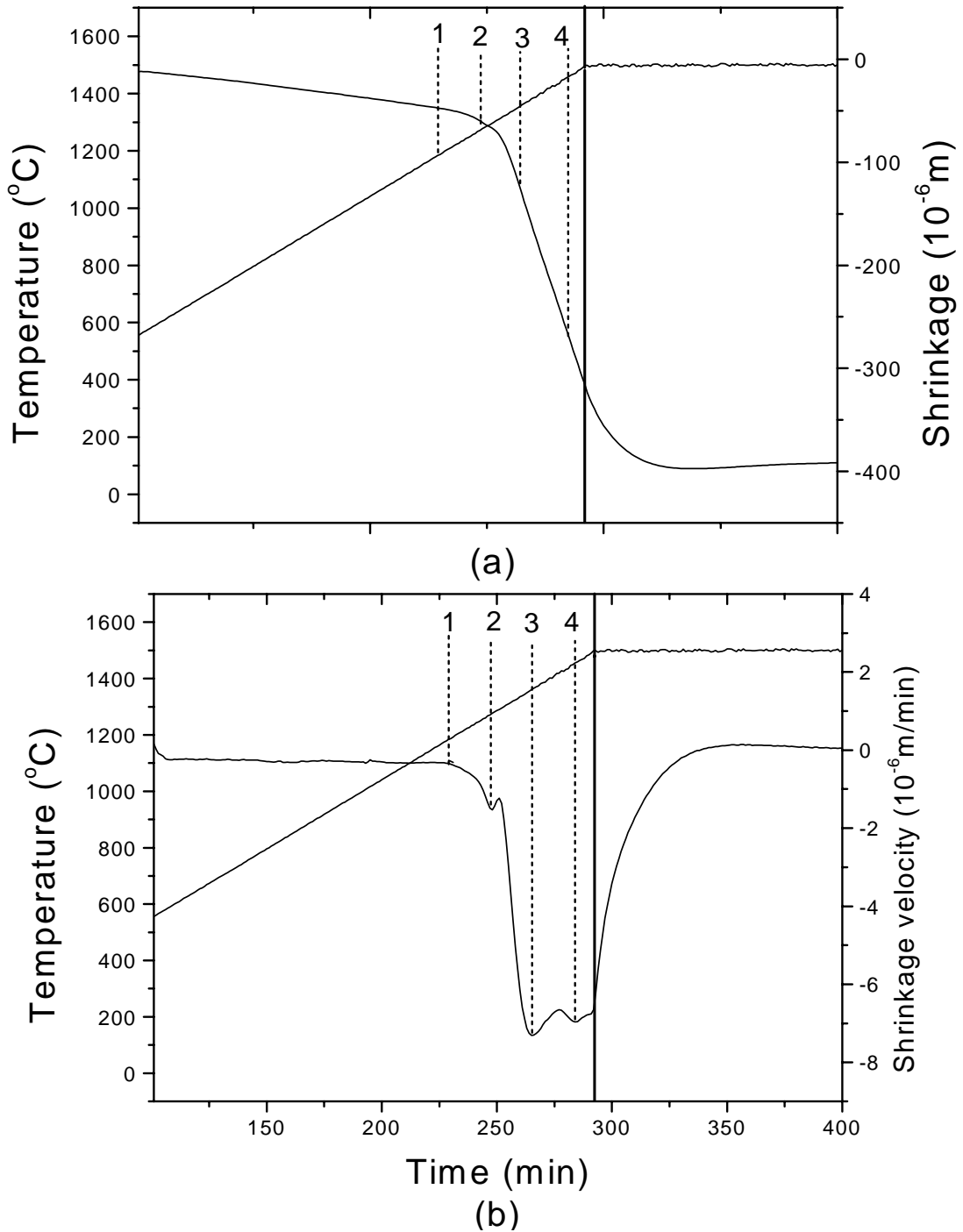


**Fig. 5.5 :** Shrinkage (a) and shrinkage velocity (b) of a silicon nitride green body with 15% LiYO<sub>2</sub> additive showing characteristic features at (1) 1180 °C; (2) 1275 °C; (3) 1364 °C and (4) 1453 °C.

into the liquid (Table 5-I). This confirms that LiYO<sub>2</sub> acts as a very good flux and a solvent for Si<sub>3</sub>N<sub>4</sub> which is also a prerequisite for a good sintering additive [144].

The XRD pattern of the sample quenched at 1364°C (point 3) shows the disappearance of the LiSiNO phase resulting in an increasing amount of the liquid phase and consequently, an accelerated shrinkage. The maximum at 1453°C corresponds to the onset of the phase transformation from  $\alpha$ -Si<sub>3</sub>N<sub>4</sub> to  $\beta$ -Si<sub>3</sub>N<sub>4</sub>. The densification rate decreases from this point, coinciding with a significant degree of  $\alpha$ → $\beta$  transformation.

*Table 5-I : Phase contents of the samples quenched at different temperatures.*

Temperature (°C)	Phase Content (wt %)	Remarks
1180	$\beta$ -Si <sub>3</sub> N <sub>4</sub> 21 %	onset of shrinkage
1275	$\beta$ -Si <sub>3</sub> N <sub>4</sub> 22 % LiSiNO, Y <sub>5</sub> (SiO <sub>4</sub> ) <sub>3</sub> N	1 <sup>st</sup> maximum of shrinkage velocity
1364	$\beta$ -Si <sub>3</sub> N <sub>4</sub> 23 % Y <sub>5</sub> (SiO <sub>4</sub> ) <sub>3</sub> N	2 <sup>nd</sup> maximum of shrinkage velocity
1453	$\beta$ Si <sub>3</sub> N <sub>4</sub> 26 % Y <sub>5</sub> (SiO <sub>4</sub> ) <sub>3</sub> N	3 <sup>rd</sup> maximum of shrinkage velocity
1500	$\beta$ -Si <sub>3</sub> N <sub>4</sub> 32 % Y <sub>5</sub> (SiO <sub>4</sub> ) <sub>3</sub> N	after annealing for 5 min
1500	$\beta$ -Si <sub>3</sub> N <sub>4</sub> 65 % Y <sub>5</sub> (SiO <sub>4</sub> ) <sub>3</sub> N	after annealing for 2 h

#### **5.1.1.2. Si<sub>3</sub>N<sub>4</sub>-Li<sub>2</sub>O-Al<sub>2</sub>O<sub>3</sub>-SiO<sub>2</sub> system**

The dilatometric data (Fig. 5.6) show that shrinkage first occurs at 1080°C and increases somewhat at 1270°C for all samples, except for that with 5 wt% of additive. The shrinkage continues during the isothermal annealing at 1500°C. The onset of shrinkage is related to liquid formation in the sample compacts.

The effect of additive content on the linear shrinkage of the samples is shown in Fig. 5.7. Linear shrinkage increases significantly from 3 to 8% for the samples containing 5 and 10% of additives respectively. However, with further increasing additive content, linear shrinkage remains nearly constant. Linear shrinkage values ranging from 8.1 to 8.5% are obtained for samples containing 10, 15 and 20 wt% of additives.

The remarkably low shrinkage of samples with 5 wt% of additive could be attributed to an insufficient liquid formation. In general, more liquid is formed when the amount of additive is increased. In spite of growing additive content, it is found that the shrinkage reaches nearly the same value in the range of 10 to 20 wt% of additives. This indicates that the liquid volume

does not differ much with increasing additive content or the liquid content has not much pronounced influence on densification.

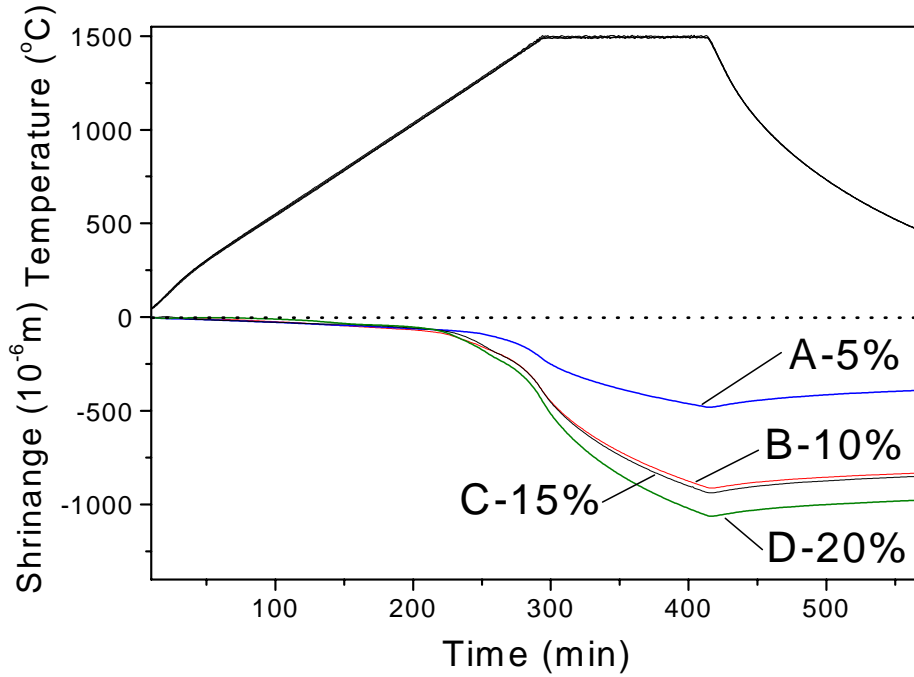


**Fig. 5.6 :** Length change of  $\text{Si}_3\text{N}_4$  green bodies (A-5 wt%, B-10 wt%, C-15 wt%, D-20 wt% of  $\text{LiAlSiO}_4$ ) between room temperature and 1500 °C. A cylinder-shaped test body was examined by dilatometry in nitrogen atmosphere.

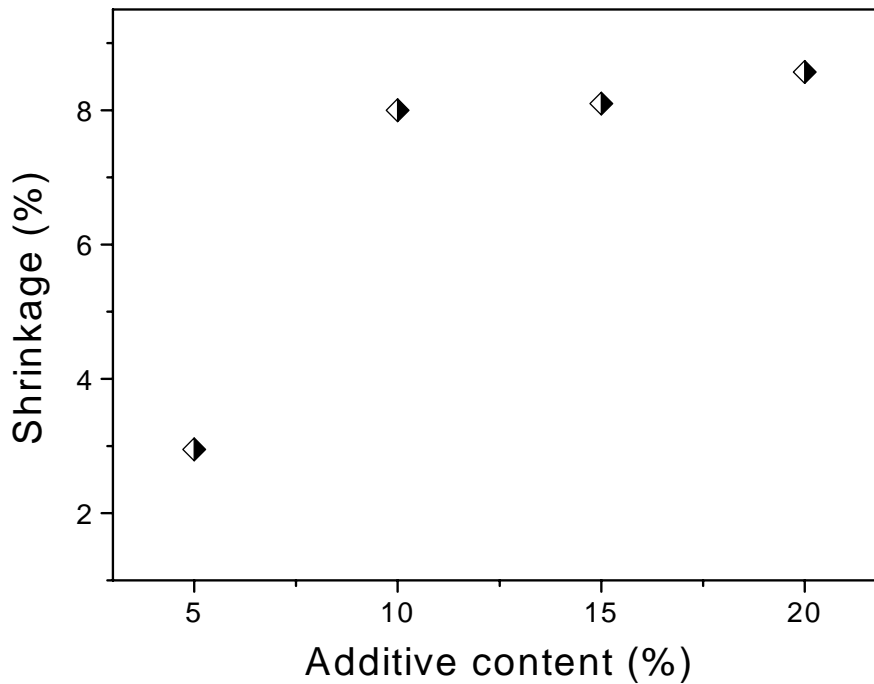


**Fig. 5.7:** Linear shrinkage versus  $\text{LiAlSiO}_4$  additive content in dilatometer experiments, after a holding time of 5 min at 1500 °C.



The maximum achieved density i.e.  $2.65 \text{ g/cm}^3$  is obtained for 10 wt% of additive. Actually, the presence of  $\text{Li}_2\text{O}$  allows for the formation of a liquid phase at very low temperature. In case of samples with 10 wt% of additive the density has already increased to  $2.03 \text{ g/cm}^3$  at  $1080^\circ\text{C}$ , that is nearly 10 % higher than the density of the starting mixture. With prolonged heating time, the density further increases to  $2.65 \text{ g/cm}^3$  at  $1500^\circ\text{C}$  (Fig. 5.8). In spite of the low sintering temperatures all the materials were not fully dense after dilatometric measurements up to  $1500^\circ\text{C}$ . This has to be attributed to the the influence of the furnace atmosphere inside the dilatometer and the small size of the samples.

The influence of the amount of  $\text{LiAlSiO}_4$  additive on the densification of  $\text{Si}_3\text{N}_4$  is shown in Fig. 5.9. The best results were obtained for bodies with 10 or 15 % of additive, with attending of decreasing density upon further increase of the additive content.

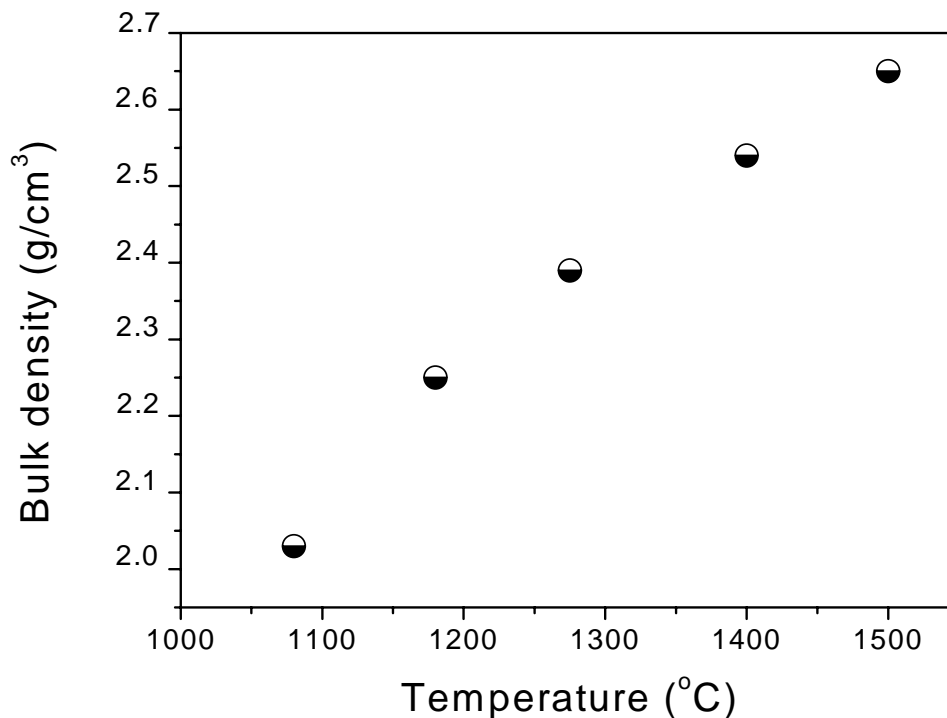


**Fig. 5.8 :** Density according to dilatometric measurements of  $\text{Si}_3\text{N}_4$  with 10 wt% of  $\text{LiAlSiO}_4$  additive after a holding time of 5 min.

The shrinkage and shrinkage rate during densification of a sample with 10 % of additive are shown in Fig. 5.10. The shrinkage rate curve shows three maxima at  $1180^\circ\text{C}$ ,  $1275^\circ\text{C}$  and  $1490^\circ\text{C}$  indicated by three points 2 to 4.

The XRD patterns of the samples quenched at these temperatures show different phase compositions as listed in Table 5-II, indicating that the viscosity and volume of the liquid phase change significantly during heating.

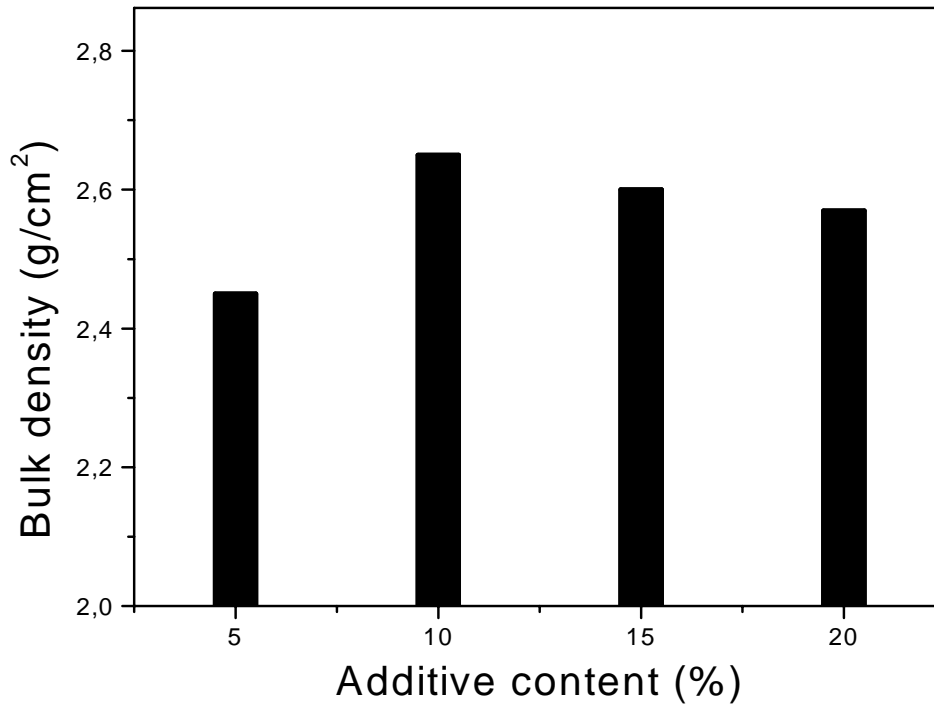


**Fig. 5.9:** Influence of the amount of  $\text{LiAlSiO}_4$  additive on the densification of  $\text{Si}_3\text{N}_4$  samples fired at  $1500^\circ\text{C}$  with a holding a time of 5 min.

The appearance of the liquid in the sample starts at  $1080^\circ\text{C}$  (point 1) corresponding to the eutectic melting point in the  $\text{Li}_2\text{O}-\text{SiO}_2$  phase diagram [142]. The maximum at  $1180^\circ\text{C}$  (point 2) is related to an increasing amount of the liquid phase. Its phase composition shows lowering of the intensity of  $\beta$ -eucryptite i.e.  $\text{LiAlSiO}_4$  phase due to its melting. The presence of coesite ( $\text{SiO}_2$ ) is associated with excess silica which has crystallized from the liquid during cooling. The XRD pattern for the sample quenched at  $1275^\circ\text{C}$  (point 3), shows the disappearance of the  $\beta$ -eucryptite phase but appearance of  $\beta$ -spodumen ( $\text{LiAlSiO}_6$ ) which is a phase with the same cation ratio (Li : Al) as a  $\text{LiAlSiO}_4$  but containing a higher amount of silica. In spite of the total conversion of  $\text{LiAlSiO}_4$  additive into liquid phase the total amount of liquid phase does not increase significantly due to partial crystallization into a new phase ( $\text{LiAlSiO}_6$ ). This leads only to moderate increase of density.

The maximum at 1490°C, which occurs together with a decrease in the XRD intensity of the  $\text{LiAlSiO}_6$  phase and an increase in the intensity of  $\text{SiO}_2$ , corresponds to a increasing volume of the liquid phase.

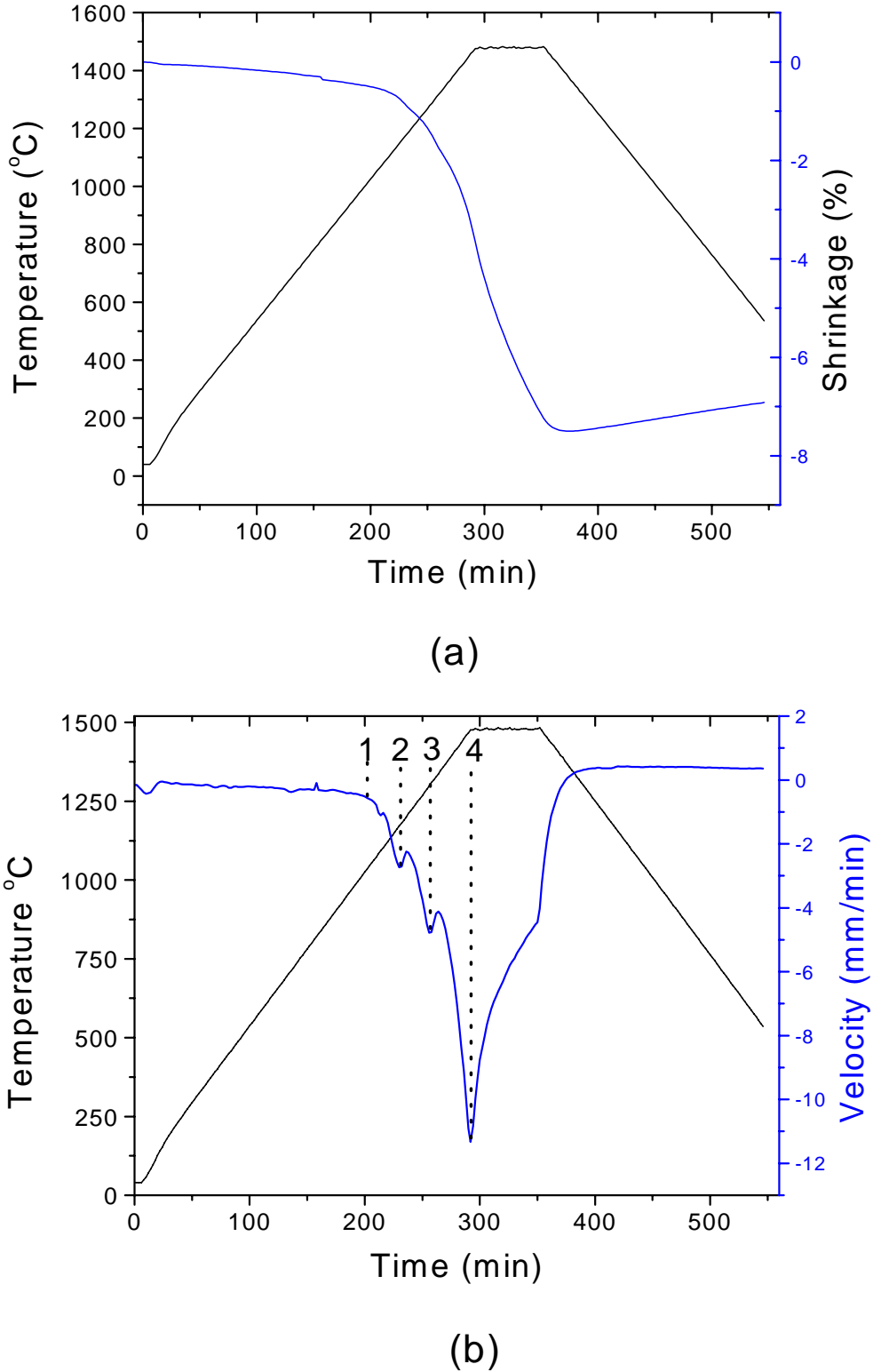


**Fig. 5.10** : Shrinkage (a) and shrinkage velocity (b) of a silicon nitride green body with 15%  $\text{LiAlSiO}_4$  additive showing characteristic features at (1) 1080 °C, (2) 1180 °C; (3) 1275 °C and (4) 1490 °C.

However, the  $\alpha/\beta$ - $\text{Si}_3\text{N}_4$  ratio remains the same up to  $1500^\circ\text{C}$  indicating that no significant transformation takes place during the first stage of sintering. This means that the initial stage is related with the formation of the liquid phase and to the reaction between the sintering additive and the surface silica from  $\text{Si}_3\text{N}_4$  grains.

*Table 5-II : Phase contents of the samples quenched from different temperatures.*

Temperature ( $^\circ\text{C}$ )	Phase content (wt%)	Remarks
1080	$\beta$ - $\text{Si}_3\text{N}_4$ 20 % $\beta$ - $\text{LiAlSiO}_4$	onset of shrinkage
1180	$\beta$ - $\text{Si}_3\text{N}_4$ 20 % $\beta$ - $\text{LiAlSiO}_4$ , $\text{SiO}_2$	1 <sup>st</sup> maximum of shrinkage velocity
1275	$\beta$ - $\text{Si}_3\text{N}_4$ 20 % $\beta$ - $\text{LiAlSi}_2\text{O}_6$ , $\text{SiO}_2$	2 <sup>nd</sup> maximum of shrinkage velocity
1490	$\beta$ $\text{Si}_3\text{N}_4$ 20 % $\beta$ - $\text{LiAlSi}_2\text{O}_6$ , $\text{SiO}_2$	3 <sup>rd</sup> maximum of shrinkage velocity
1500	$\beta$ $\text{Si}_3\text{N}_4$ 20 % $\beta$ - $\text{LiAlSi}_2\text{O}_6$ , $\text{SiO}_2$	after annealing for 5 min
1500	$\beta$ - $\text{Si}_3\text{N}_4$ 35 % $\text{SiO}_2$	after annealing for 2 h

The results from the dilatometric measurements show that materials with both additive systems were not fully dense after heating up to  $1500^\circ\text{C}$ . Densification is more effective with the  $\text{LiYO}_2$  system than with the  $\text{LiAlSiO}_4$  system under the same sintering conditions as shown in Fig. 5.4 and Fig. 5.9. This behavior can not be explained exclusively by the difference in the volume fraction and liquid viscosity of the two systems. Reaction with the reducing gas atmosphere inside the graphite-heated sintering furnace should also be taken into consideration [145].

It was found that the crystallization of the secondary phases from the melt can already occur during sintering especially for compositions on a tie line between one secondary phase and  $\text{Si}_3\text{N}_4$ . In this case, the volume fraction of the liquid phase is strongly reduced and complete densification is impossible [146]. According to the XRD patterns and densities of the samples quenched at particular temperatures during dilatometric measurement, the amount of liquid due to the sequence of chemical reactions increases only slowly with temperature. Hence, the densification may be assumed to take place with less particle rearrangement than is usual in the liquid phase sintering. This explains why the variation in shrinkage and density that is obtained for samples having different additive contents is much smaller than in case of the  $\text{LiYO}_2$  additive.

In the case of the  $\text{LiYO}_2$  system, the density increases monotonically with increasing additive content according to Fig. 5.4. Higher additive content provides a higher volume of liquid needed to fill the porosity. In addition, an appreciable amount of  $\text{Si}_3\text{N}_4$  can be dissolved in the liquid formed, which additionally leads to higher densification [56].

## 5.2 Sintering density

Nonisothermal sintering experiments up to  $1500^\circ\text{C}$  show that the relative densities reached are still too low for high mechanical strength and hardness. In order to further increase the density to above 95%, densification was conducted at different temperatures from  $1550^\circ\text{C}$  to  $1700^\circ\text{C}$  with 50 K intervals for different holding times.

The influence of temperature on densification during sintering at higher temperatures for very short annealing time (5 min) is given in Fig. 5.11. At lower temperatures densification is more

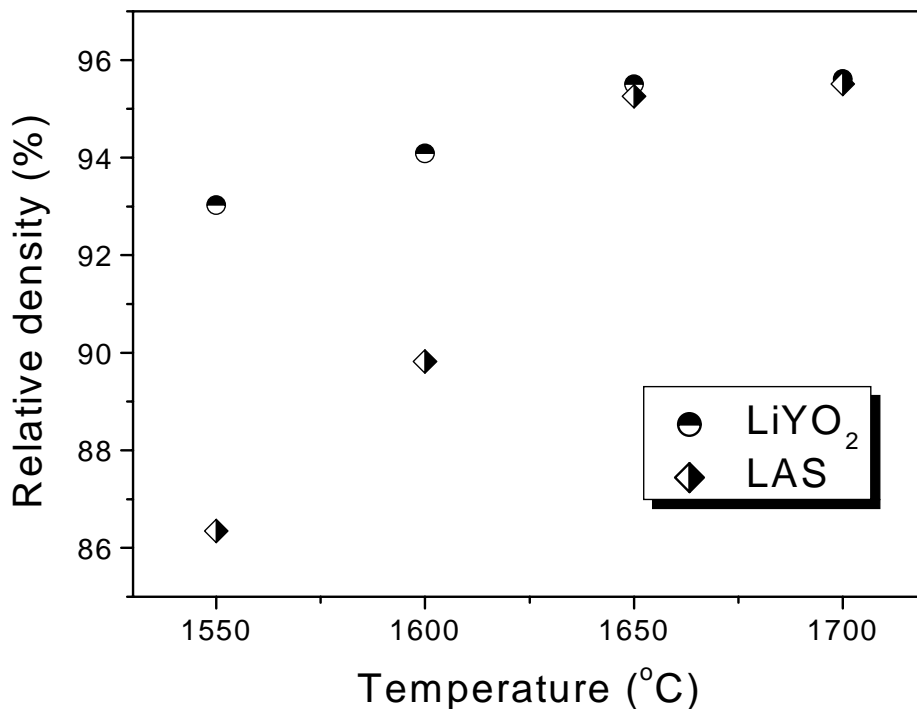


**Fig. 5.11** : The difference in the densification behavior between  $\text{Si}_3\text{N}_4\text{-LiYO}_2$  and  $\text{Si}_3\text{N}_4\text{-LiAlSiO}_4$  ceramics with 15% of additive sintered at different temperatures from  $1500^\circ\text{C}$  up to  $1700^\circ\text{C}$  with a holding time of 5 min.

pronounced for bodies sintered with  $\text{LiYO}_2$  additive. The densification increases monotonically with increasing temperature. In the case of  $\text{LiAlSiO}_4$  additive, with increasing

temperature the increment between the density values gets higher until 1650°C. At 1700°C, > 95% of the theoretical density are obtained with both additive systems.

The densification behavior at 1500°C as a function of annealing time is shown for the  $\text{Si}_3\text{N}_4$ - $\text{LiYO}_2$  and  $\text{Si}_3\text{N}_4$ - $\text{LiAlSiO}_4$  systems in Fig. 5.12 and Fig. 5.13, respectively.

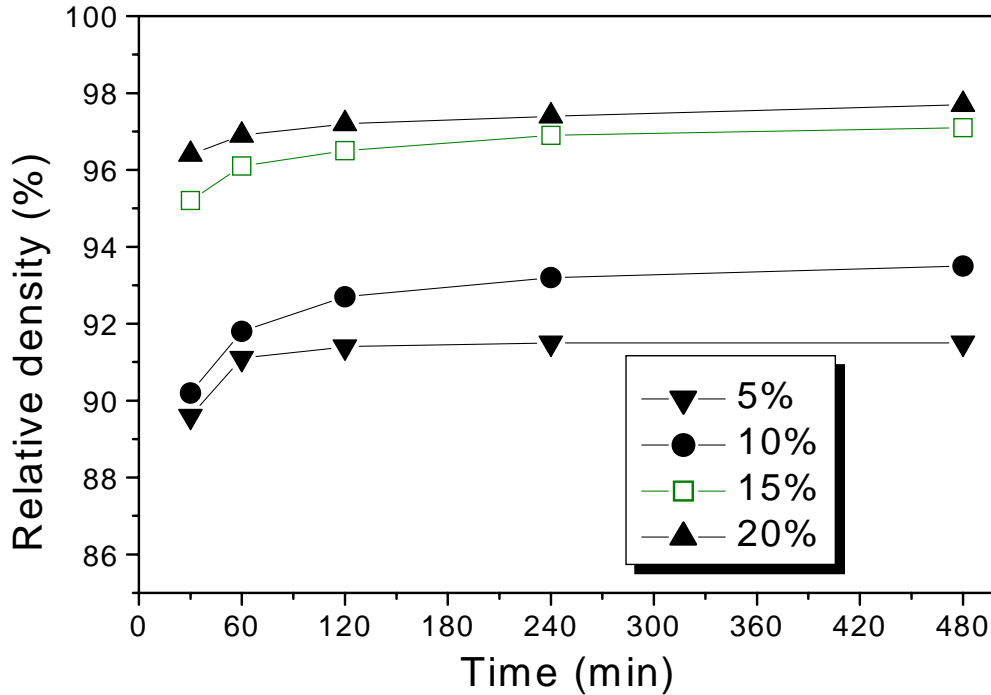


**Fig. 5.12 :** Relative densities at 1500 °C vs. annealing time for  $\text{Si}_3\text{N}_4$  with  $\text{LiYO}_2$  additives (5, 10, 15 and 20%).

At 1500°C, densification is higher by nearly 2% with the  $\text{LiYO}_2$  additive when compared to  $\text{LiAlSiO}_4$ . In the case of  $\text{LiYO}_2$ , the maximum density is obtained for bodies having higher additive content, while in the case of  $\text{LiAlSiO}_4$  additive, the densification is nearly the same for bodies with 10 and 15% of additives. The difference in densification versus additive content is more pronounced in the  $\text{LiYO}_2$  additive system.

The relationships between relative density and sintering temperature for the compositions with different amounts of additives are listed in Table 5-III and Table 5-IV, respectively.

In case of bodies with at least 15 wt% of  $\text{LiYO}_2$  additive, high relative densities are obtained after just 2 h of sintering, while the densities remain nearly constant upon prolonged sintering. However, all samples sintered at higher temperature and longer annealing times show the same trend of decreasing density. The samples sintered at 1550°C were found to exhibit higher densities in comparison with samples sintered at 1600°C and 1650°C.

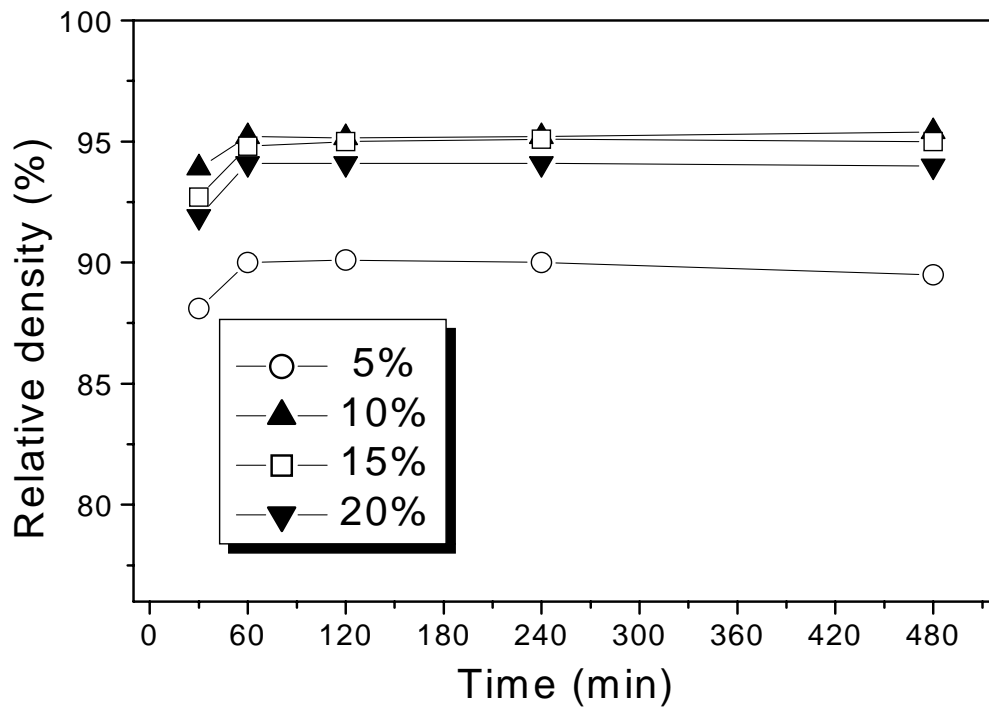


**Fig. 5.13** : Relative densities at 1500 °C vs. annealing time for  $\text{Si}_3\text{N}_4$  with  $\text{LiAlSiO}_4$  additives (5, 10, 15 and 20%).

Higher relative density obtained at lower sintering temperatures may be attributed to the lower partial pressure of evaporating phases at these lower temperatures, especially with respect to lithia and silica. It has been noticed during dilatometric measurement that a significant mass

*Tabele 5-III : Densities after sintering with different amounts of the  $\text{LiYO}_2$  additive.*

Additive content (wt%)	1550°C			1600°C			1650°C		
	2 h	4 h	8 h	2 h	4 h	8 h	2 h	4 h	8 h
5	88.7	88.95	88.1	88.5	88.2	87.8	88.1	80.0	79.6
10	94.9	95.1	95.0	95.2	94.9	94.2	93.7	93.1	92.4
15	98.3	98.3	98.3	98.3	98.1	97.2	98.3	97.8	97.5
20	98.3	98.2	98.3	98.3	97.8	97.8	98.2	97.6	97.5

loss occurred. As shown in Fig. 14,  $\text{Li}_2\text{O}$  starts to evaporate from the samples at temperatures above 1300°C and the Li concentration is drastically reduced after holding times of several hours at 1500°C. After 8 h, the residual  $\text{Li}_2\text{O}$  content is as small as 0.08 wt%. This is in good agreement with published data [147] for the vapor pressure of  $\text{Li}_2\text{O}$  and its evaporation at higher temperatures. In contrast,  $\text{Y}_2\text{O}_3$  is very stable based on thermodynamic calculations

[148] and has no tendency for volatilization under the conditions investigated. Therefore, it can be concluded that  $\text{Li}_2\text{O}$  is removed in gaseous form during sintering, changing the liquid to a comparatively high-melting,  $\text{Y}_2\text{O}_3$ -rich composition. The lowest melting temperature in the system  $\text{Y}_2\text{O}_3$ - $\text{SiO}_2$  is  $1650^\circ\text{C}$  [98]. Thus the liquid phase is mostly transient and this must have a marked influence on the kinetics of densification and phase transformations in the system studied.

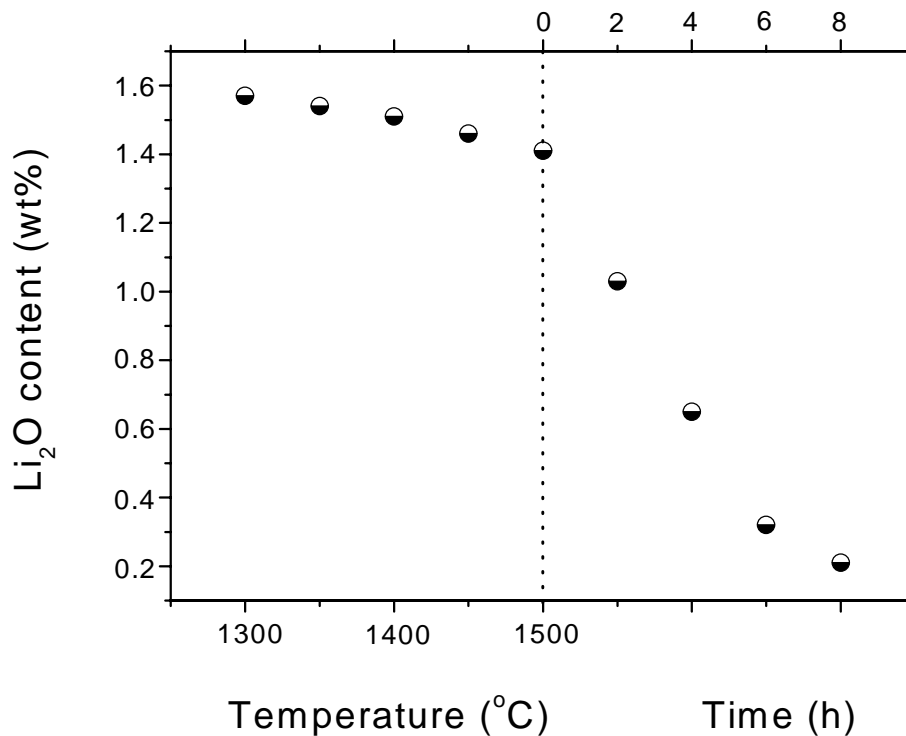


**Fig. 5. 14:** *Lithia losses of  $\text{Si}_3\text{N}_4$  compacts with 15 wt% of  $\text{LiYO}_2$  additive during dilatometric measurement and upon prolonged annealing time at  $1500^\circ\text{C}$ .*

In case of  $\text{LiAlSiO}_4$  additive, the samples sintered with lower additive content exhibit higher densities in comparison with samples containing more additive. The highest value of 98.3% for the density is obtained for bodies with 10% additive content. The densities remain nearly constant on prolonged sintering at all sintering temperatures.



Table 5-IV : Densities after sintering with different amounts of the  $\text{LiAlSiO}_4$  additive.

Additive content (wt%)	1550°C			1600°C			1650°C		
	2 h	4 h	8 h	2 h	4 h	8 h	2 h	4 h	8 h
5	90.1	89.7	89.4	89.5	89.2	89.0	89.1	88.8	87.9
10	98.3	98.3	98.3	98.3	98.1	98.1	98.1	97.7	97.5
15	98.3	98.3	98.1	98.3	97.9	97.2	97.4	97.2	96.8
20	93.6	92.7	92.4	93.0	92.3	92.0	92.3	91.5	91.2

According to XRD patterns (Table 5-II), at 1500°C all of the  $\text{LiAlSiO}_4$  additive is converted into liquid. The liquid phase formed in the  $\text{LiYO}_2$  additive system contains less silica and hence, it is thermodynamically more stable than the liquid phase in the  $\text{LiAlSiO}_4$  system which contains a substantial amount of silica. In other words, a larger amount of the liquid phase in the  $\text{LiAlSiO}_4$  system leads to more evaporation according to the reaction:

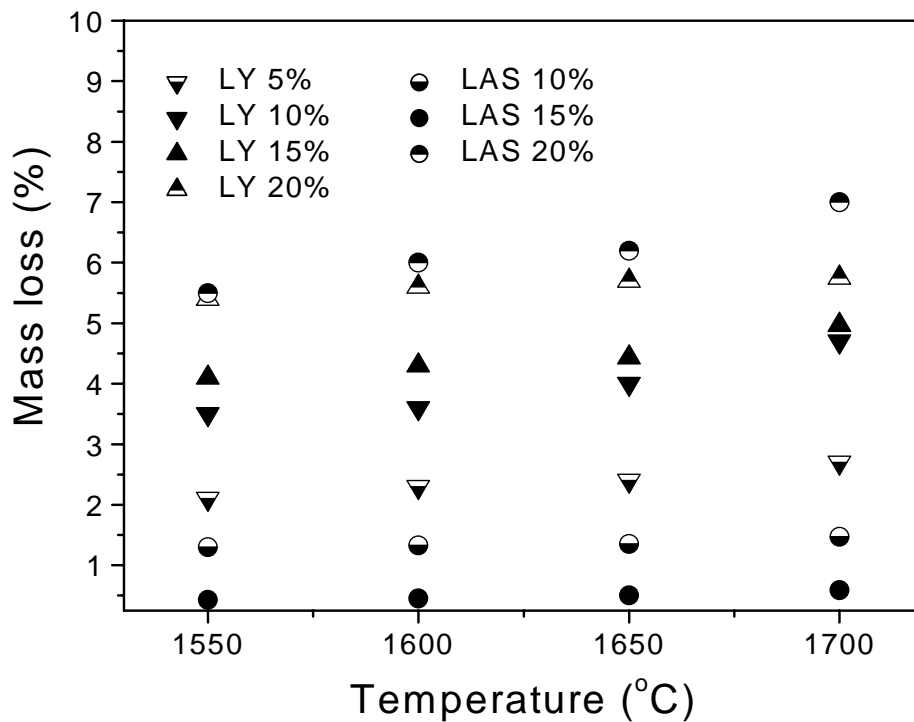
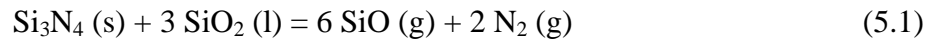
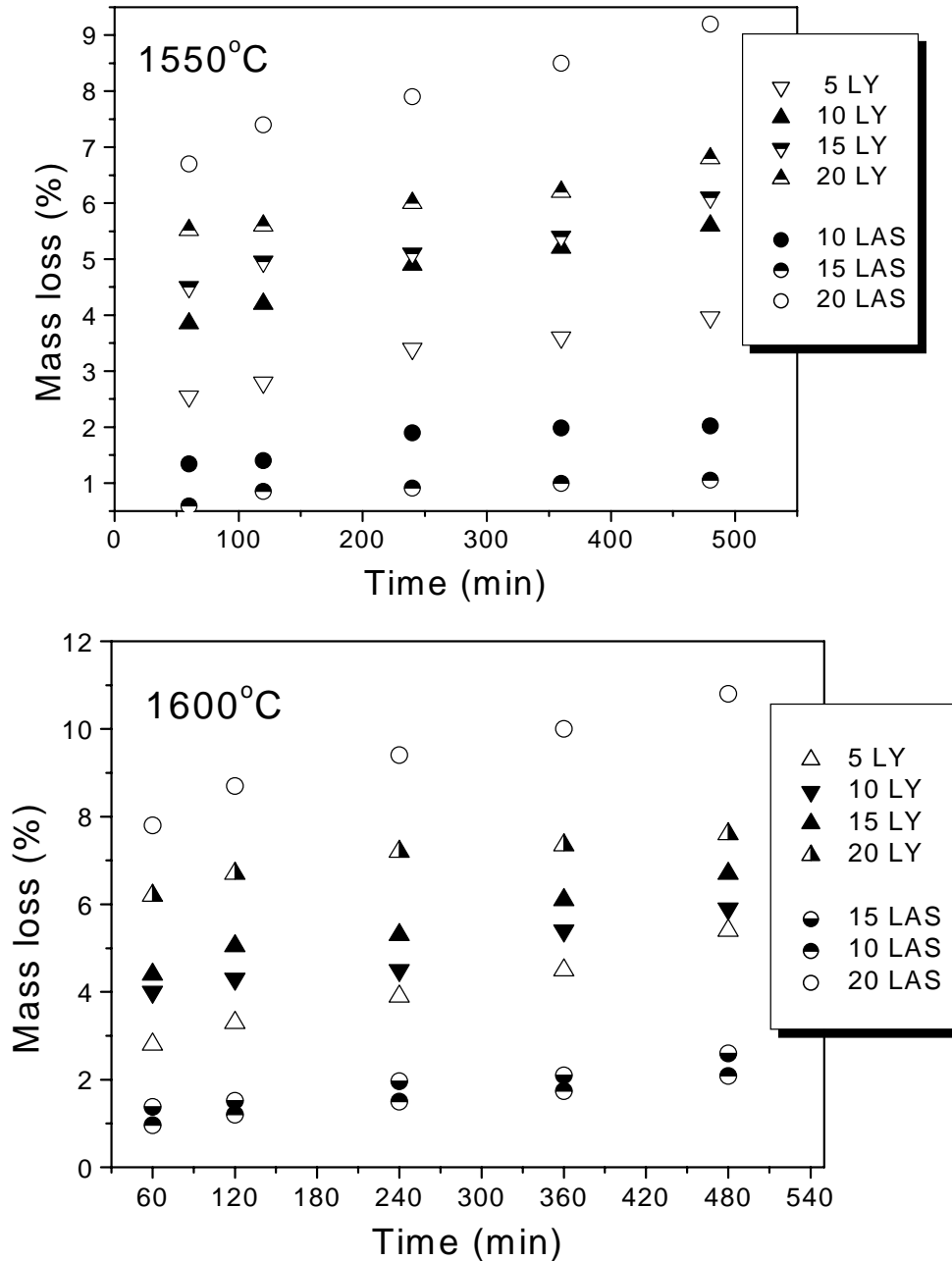


Fig. 5.15 : Mass loss as a function of temperature for  $\text{Si}_3\text{N}_4$  compacts with different amounts of  $\text{LiYO}_2$  and  $\text{LiAlSiO}_4$  additives during sintering with a holding time of 5 min.

High mass loss is harmful to sintering, which is reflected in the observation that the density of samples having 20 % of additive is always smaller than densities of bodies with 10 and 15 % of additive.

The mass loss upon sintering with the  $\text{LiAlSiO}_4$  additive system in comparison to the  $\text{LiYO}_2$  system is shown in Fig. 5.15. The same trend is also observed during isothermal annealing (Fig.5.16 a,b).



**Fig. 5.16 :** Mass loss of  $\text{Si}_3\text{N}_4$  ceramics with the additive systems  $\text{LiYO}_2$  (LY) and  $\text{LiAlSiO}_4$  (LAS), heat-treated at 1550 °C (a) and 1600 °C (b) under 0.1 MPa  $\text{N}_2$  as a function of soaking time.

Reactions between  $\text{Si}_3\text{N}_4$  and the glassy phases are responsible for the instability of  $\text{Si}_3\text{N}_4$  ceramics at elevated temperature. However,  $\text{Al}_2\text{O}_3$  and  $\text{Y}_2\text{O}_3$  are stable based on thermodynamic calculations [148]. In contrast, the high vapor pressure of lithia causes its easy evaporation as mentioned earlier. It is expected on the basis of the vapor pressure data for  $\text{Li}_2\text{O}$  [147] that lithia should volatilize completely at higher temperatures. However, the results of the chemical analysis of the samples are in contradiction with this assumption, especially for  $\text{LiAlSiO}_4$ .

The content of lithium in the  $\text{Si}_3\text{N}_4$  ceramics sintered for 4 h at various temperatures, is indicated in Fig. 5.17. The lithium content in the samples changes slightly in the case of the  $\text{LiAlSiO}_4$  additive. However, with the  $\text{LiYO}_2$  additive the lithium content decreases

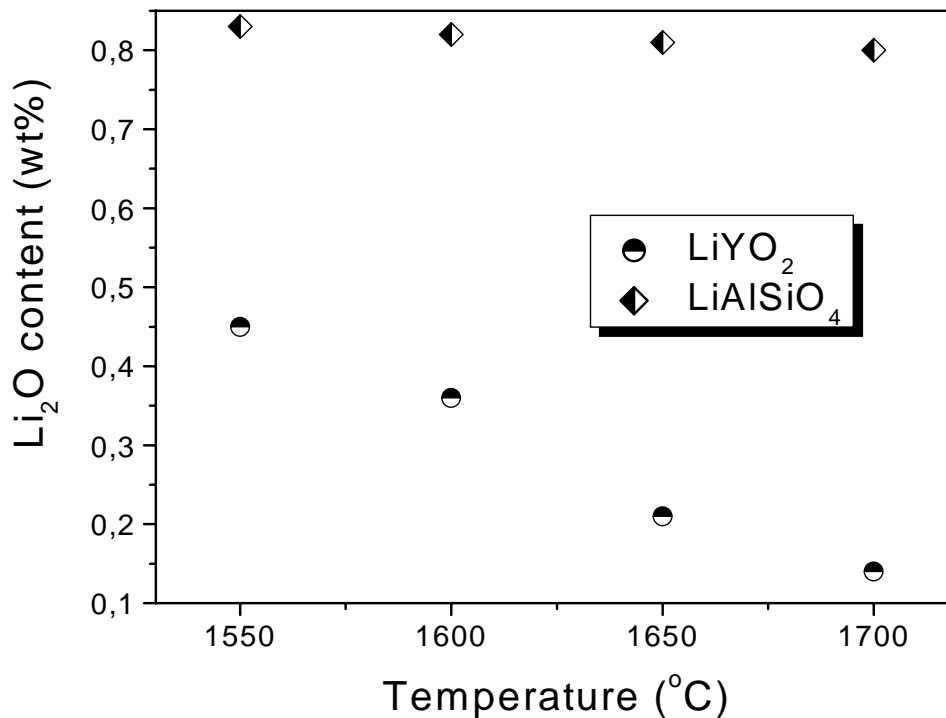


**Fig.5.17** : Mass loss of lithium in  $\text{Si}_3\text{N}_4$  samples sintered at various temperatures.

significantly with temperature. On the basis of these findings, it can be concluded that the major part of the mass loss of the  $\text{Si}_3\text{N}_4$  ceramics during sintering occurs according to the reaction (5.1), as mentioned before. This reaction is well known from thermodynamical and experimental work on the Si-N-O system [149, 150]. Since the silica content in the liquid phase is higher with the  $\text{LiAlSiO}_4$  additive than with the  $\text{LiYO}_2$  additive, the rate of the decomposition reaction (5.1) is faster and consequently the mass loss is high for samples having 20 % of additives. Additionally for higher additive amounts, gas bubbling occurs

caused by an increased formation of gaseous SiO [101]. This is the case with the LiAlSiO<sub>4</sub> additive which has a higher oxygen content than the LiYO<sub>2</sub> additive.

### 5.3 General remarks

The three controlling stages: particle rearrangement, solution-precipitation and grain growth are observed in many Si<sub>3</sub>N<sub>4</sub> systems [2]. The densification is controlled by particle rearrangement and by solution-diffusion-reprecipitation processes. Particle rearrangement contributes to densification at lower temperatures and solution-diffusion-reprecipitation is dominant at higher temperatures. For the LiYO<sub>2</sub> system, the densification depends largely on the sintering additive content. The larger amount of additive means a higher volume of liquid phase, which is favorable for efficient particle rearrangement resulting in the higher value of density. In case of the LiAlSiO<sub>4</sub> additive, it is found that the densification is less dependent on the additive content. Up to 1500°C, densification is not accompanied by  $\alpha \rightarrow \beta$  Si<sub>3</sub>N<sub>4</sub> transformation. Thus, the final density is thought to be reached largely without the intervention of the dissolution-diffusion-reprecipitation mechanism. This means that the overall sintering kinetics at low temperatures is less retarded when using the LiYO<sub>2</sub> additive in comparison to the LiAlSiO<sub>4</sub> additive, resulting in higher densities obtained at lower temperatures and short annealing times. With prolonged heating time, the differences in the degree of densification become smaller. It needs to be pointed out that the transport kinetics are also decisive for the phenomena of phase transformation (see chapter 6) and microstructural development (chapter 7).

## 6 PHASE TRANSFORMATION

The  $\alpha \rightarrow \beta$  phase transformation is a phenomenon which always occurs when  $\alpha$ - $\text{Si}_3\text{N}_4$  containing powders will be liquid phase sintered [151]. This process is substantially influenced not only by the amount but also by the chemistry of the liquid phase. It occurs by solution-diffusion-precipitation. Hence it is of great significance to describe this mechanism, which in turn has an impact on grain growth and microstructural development. In this chapter the various factors influencing the transformation, its kinetic and the relation of phase transformation to densification are dealt with.

### 6.1 Temperature and time dependence

Fig. 6.1 shows the changes in  $\beta$ - $\text{Si}_3\text{N}_4$  phase content as a function of sintering temperature. With both additive systems, the time dependence of the  $\alpha \rightarrow \beta$  phase transformation displays a sigmoidal behaviour. However, the starting temperatures of the phase-transformation are significantly different for the two systems. With the  $\text{LiYO}_2$  additive, the phase transformation

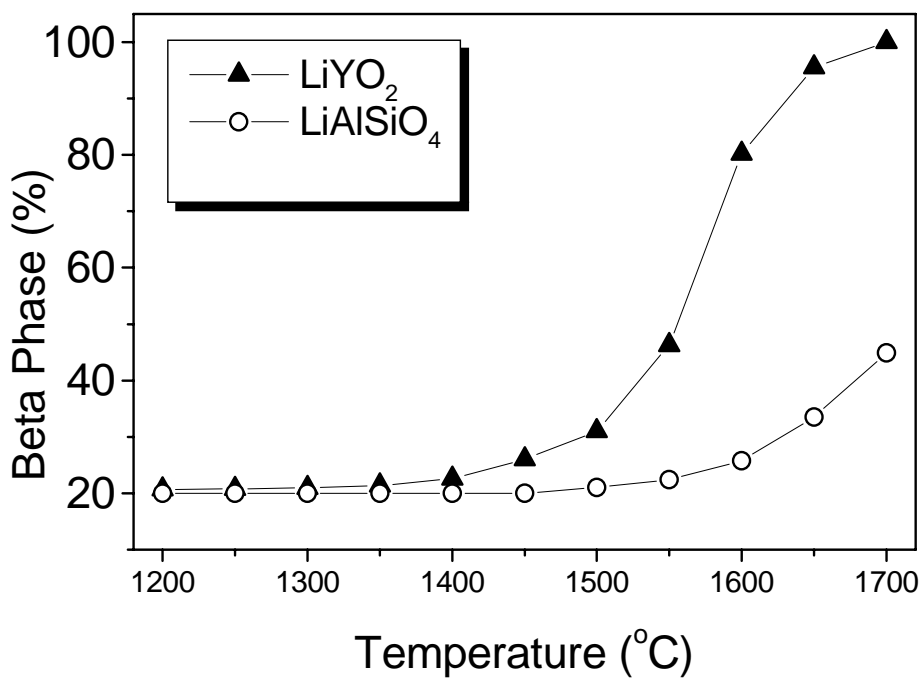


**Fig. 6.1** : The  $\alpha \rightarrow \beta$ - $\text{Si}_3\text{N}_4$  phase transformation as a function of temperature in the  $\text{Si}_3\text{N}_4$ - $\text{LiYO}_2$  and  $\text{Si}_3\text{N}_4$ - $\text{LiAlSiO}_4$  systems for 5 minutes of annealing.

already commences at 1300°C although only a small amount of transformation is observed. For samples with 15 wt% of additives, the transformation accelerates at 1500°C and is terminated at 1700°C after 5 minutes of annealing time.

In the case of the  $\text{LiAlSiO}_4$  additive system the transformation starts at 1500°C and increases only slightly with temperature (Fig. 6.1). The crystalline lithium aluminum silicate phase  $\beta$ -spodumene ( $\text{LiAlSiO}_6$ ) remains stable as long as the temperature is lower than 1500°C. In this stage, the liquid content is limited in the system. The  $\beta$ -spodumene phase, however, starts to dissolve into the liquid as the temperature exceeds 1500°C. This increases the amount of liquid. The maximum degree of  $\alpha \rightarrow \beta$ - $\text{Si}_3\text{N}_4$  transformation for samples with 15 wt% of additive was about 45% at 1700°C after 5 minutes of sintering time.

However, with prolonged annealing time the degree of phase transformation significantly increases in both cases (Fig. 6.2). With the  $\text{LiYO}_2$  additive the phase transformation is finished at 1500°C after 1 hour of sintering, while a higher temperature of 1600°C is necessary to convert all  $\alpha$ - $\text{Si}_3\text{N}_4$  phase in the  $\text{LiAlSiO}_4$ -containing system. The delayed phase transformation in the

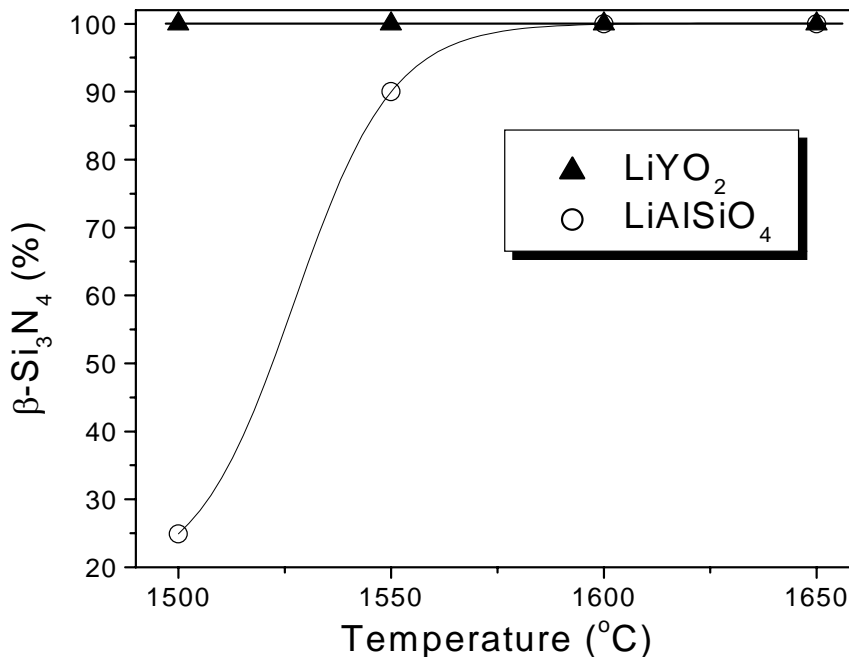


**Fig. 6.2 :** The phase transformation as a function of temperature in the  $\text{Si}_3\text{N}_4$ - $\text{LiYO}_2$  and the  $\text{Si}_3\text{N}_4$ - $\text{LiAlSiO}_4$  systems (15 wt%) for 1 hour of annealing.

LiAlSiO<sub>4</sub>-containing system suggests that phase transformation is sensitive to the liquid viscosity.

## 6. 2 Influence of additive content

The sintering experiments showed that the densification process is accompanied by the  $\alpha \rightarrow \beta$  Si<sub>3</sub>N<sub>4</sub> phase transformation with LiYO<sub>2</sub> at low temperatures (below 1500°C), while the action of the dissolution-diffusion-precipitation mechanism is retarded with the LiAlSiO<sub>4</sub> additive at the same temperatures. Thus the phase transformation is faster in the LiYO<sub>2</sub>-SiO<sub>2</sub> system. Particularly, in the Si<sub>3</sub>N<sub>4</sub>-LiYO<sub>2</sub> system the degree of phase transformation increases with increasing additive content. This can be explained by the fact that increasing volume fraction of the liquid the amount of solute transported through the intergranular liquid film increases and a larger amount of phase transformation results.

Fig. 6.3. and Fig. 6.4. show the effect of additive content on phase transformation during sintering of Si<sub>3</sub>N<sub>4</sub>-LiAlSiO<sub>4</sub> ceramics as a function of temperature and the annealing time, respectively.

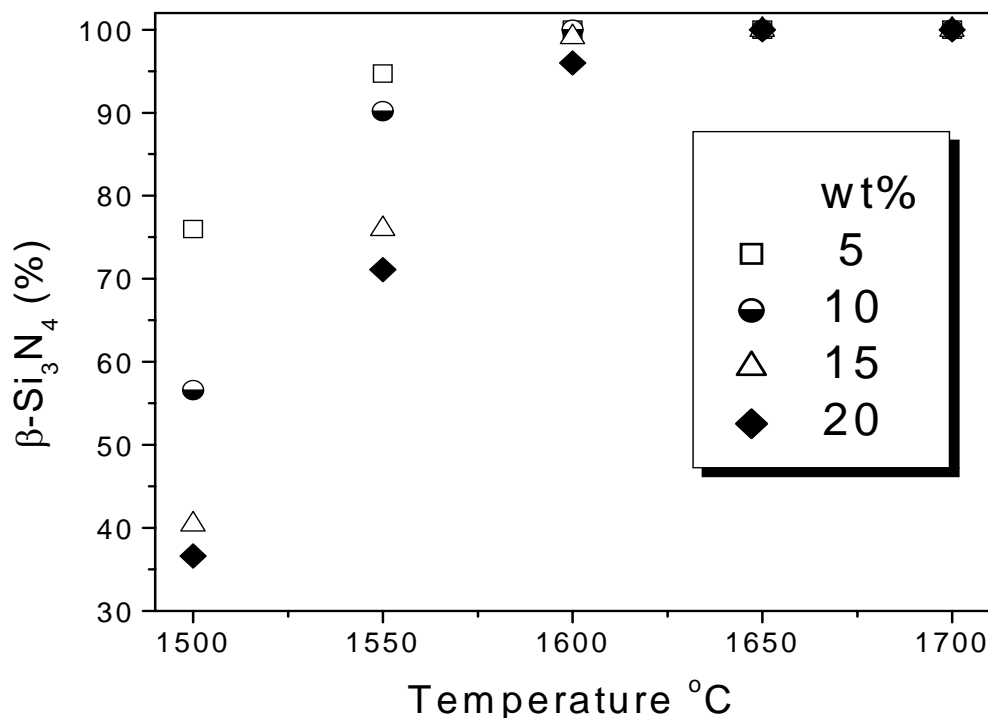


**Fig. 6.3 :** The effect of additive content on  $\alpha \rightarrow \beta$ -Si<sub>3</sub>N<sub>4</sub> phase transformation during the sintering of Si<sub>3</sub>N<sub>4</sub>-LiAlSiO<sub>4</sub> ceramics for 1 h at different temperatures.

In case of the Si<sub>3</sub>N<sub>4</sub>-LiAlSiO<sub>4</sub> system increasing the additive content leads a decreasing degree of phase transformation. The large additive content increases resulting in the longer

distance and larger difficulty for the diffusion of Si and N along the liquid phase and therefore the phase transformation is retarded with increasing additive content.

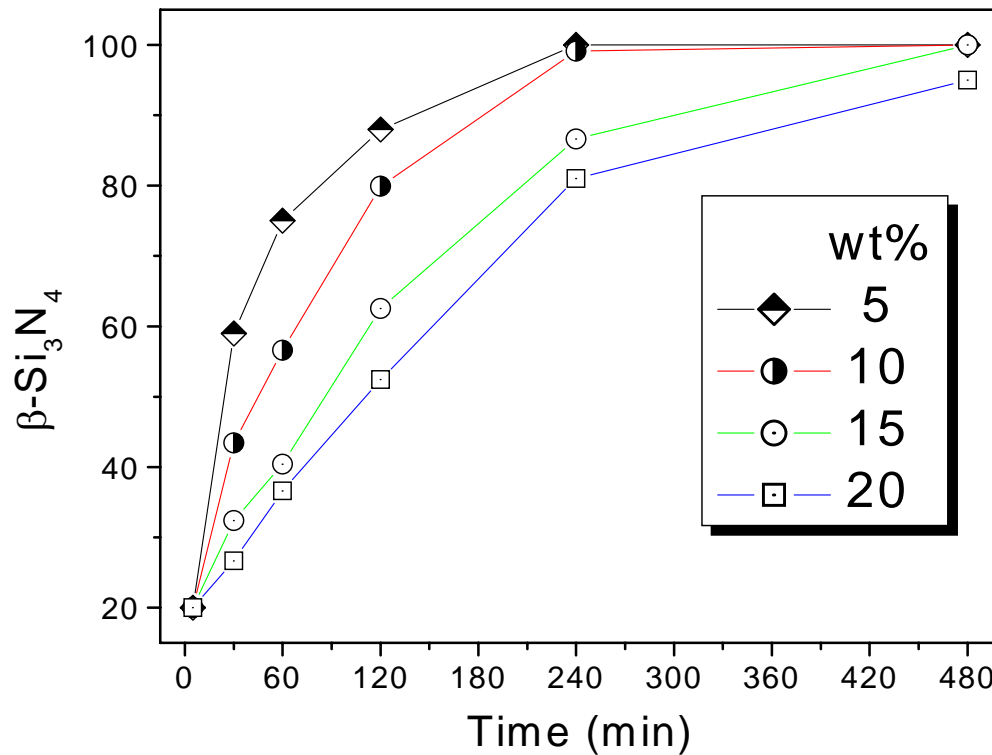


**Fig. 6.4 :** The effect of additive content on  $\alpha \rightarrow \beta$ -Si<sub>3</sub>N<sub>4</sub> phase transformation during the sintering of Si<sub>3</sub>N<sub>4</sub>-LiAlSiO<sub>4</sub> ceramics at 1500 °C.

### 6. 3 Kinetics of phase transformation

The curves for the time dependence of the  $\alpha \rightarrow \beta$  transformation suggest that the conversion kinetics is of first order. This can be described by the equation:

$$\frac{d\alpha}{dt} = -K\alpha \quad (6.1)$$

where  $K$  is a rate constant which accounts for the influence of temperature and  $\alpha$  is the concentration of the  $\alpha$ - Si<sub>3</sub>N<sub>4</sub> phase in the sintered samples. The transformation rate depends not only on the concentration of the  $\alpha$ -phase, but also on the composition and amount of liquid phase as given by the parameter  $K$ . The volume and viscosity of the vitreous phase will determine the extent to which compositional gradients and the nitrogen supersaturation in the



$\alpha$ - $\text{Si}_3\text{N}_4$ /liquid interface are maintained. The plots of  $\log(\alpha)$  against time are linear (Fig. 6.5. and Fig. 6.6) which supports the validity of equation (6.1).

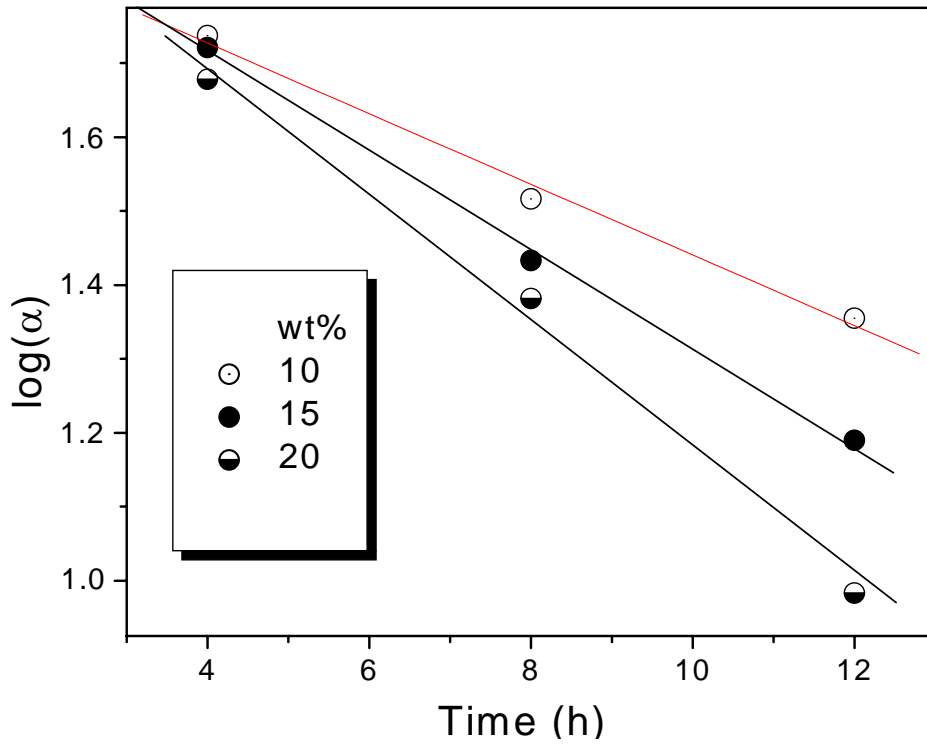


**Fig. 6.5 :** Linear dependence of the logarithm of the  $\alpha$ - $\text{Si}_3\text{N}_4$  concentration on time for  $\text{Si}_3\text{N}_4$  containing various amounts of  $\text{LiYO}_2$  additive at  $1450^\circ\text{C}$ .

In the  $\text{LiYO}_2$  system, the transformation rate constant increases with increasing additive content while the opposite behavior is observed in the  $\text{LiAlSiO}_4$  additive system, i.e. the rate constant decreases with higher additive content. The addition of  $\text{Y}_2\text{O}_3$  to silica produces an important accelerating effect on both the phase transformation and the densification of  $\text{Si}_3\text{N}_4$  ceramics [152]. In this case, a higher additive content creates a higher volume of liquid phase, and as a result, faster  $\alpha \rightarrow \beta$  phase transformation and higher densities are obtained (chapter 5). In the  $\text{LiAlSiO}_4$  additive system the more the liquid phase is present, the longer it will take to reach the total  $\alpha \rightarrow \beta$  conversion.

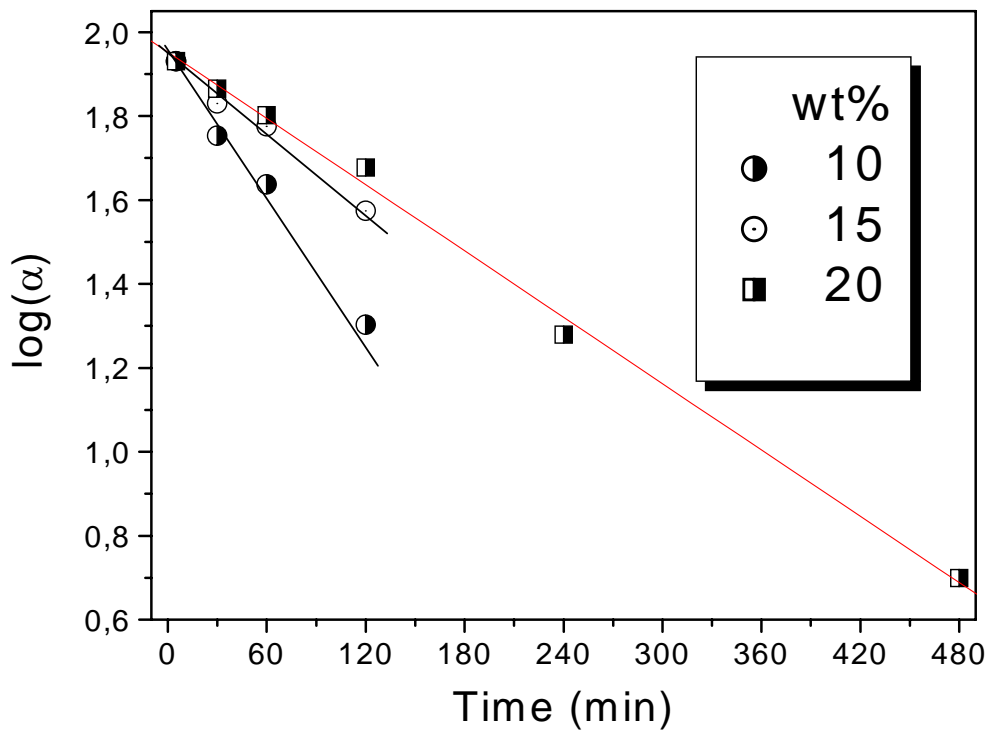


**Fig.6.6 :** Linear dependence of  $\log \alpha$ -phase content on time for  $\text{Si}_3\text{N}_4$  containing various amounts of the  $\text{LiAlSiO}_4$  additive at  $1500\text{ }^\circ\text{C}$ .

#### 6. 4 Transformation mechanism

The main factor that determines the kinetics of phase transformations is the diffusion of Si and N atoms in the liquid phase. The phase transformation is rate-controlled by interfacial reactions if the diffusion velocity is high and by material transport if the diffusion velocity is low. Sintering additives affect this behaviour by changing the viscosity and amount of the liquid phase [153,154]. The rate transformation is strongly influenced by changing liquid phase content in the case of the diffusion mechanism. In contrast, it is independent of the liquid volume in the case of interface reaction control [155].

In this study, the phase transformation is very much affected by changing the additive content for both systems. Thus, it can be concluded that the phase transformation with  $\text{LiYO}_2$  additive as well as with the  $\text{LiAlSiO}_4$  additive is mainly diffusion-controlled. The difference in transformation rate between the two additive systems can be explained by the fact that the yttrium ion is primarily a network modifier in a Y-Si-O-N glass [156], i.e. it perturbs Si-O bonds thus allowing rapid diffusion of ions through the liquid phase. On the other side Si has a different behaviour, i.e. it is a glass-former and the liquid phase is more rigid compared to

the Y-Si-O-N glass. The nominal amount of Si in the material with  $\text{LiAlSiO}_4$  additive is much higher than in the material with  $\text{LiYO}_2$  resulting in slower mass transport.

### 6.5 Relation of transformation to densification

Densification and  $\alpha \rightarrow \beta$  phase transformation are two important phenomena which occur during the sintering of  $\text{Si}_3\text{N}_4$  ceramics. However, it is difficult to determine the relationship between them. There have been reports in the literature that both occur nearly simultaneously [157], but the existence of a lag between the two reactions has also been observed [158].

The present study shows that the phase transformation and densification do not have a straightforward relationship with each other. This is illustrated in Fig. 6.7 where the extent of densification and  $\alpha \rightarrow \beta$  phase transformation is compared as a function of sintering temperature.

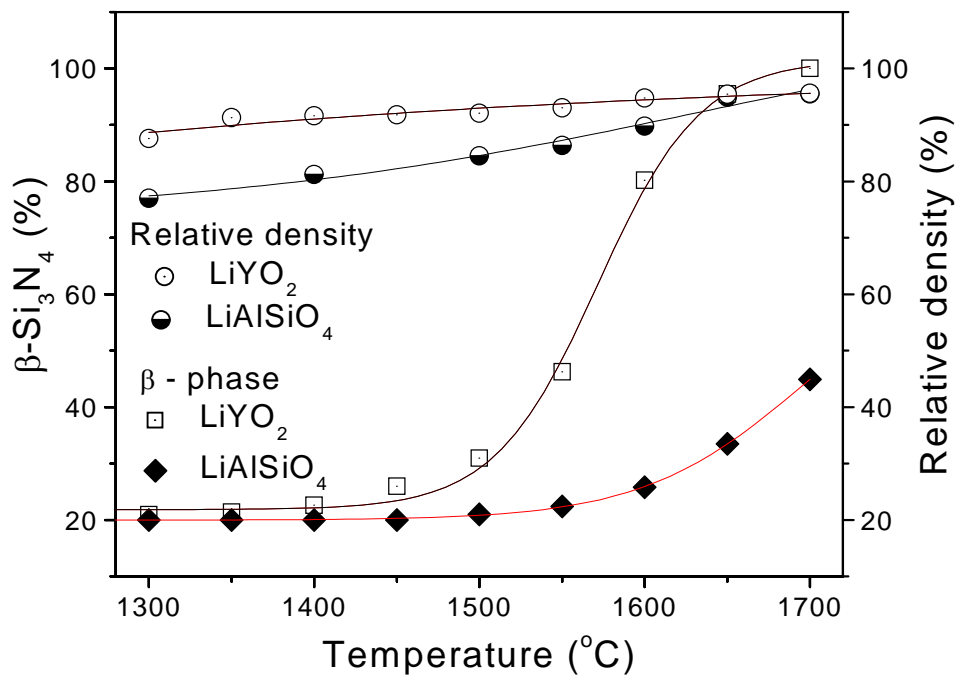


**Fig. 6.7 :** Densification and phase transformation as a function of sintering temperature for  $\text{LiYO}_2\text{-Si}_3\text{N}_4$  and  $\text{LiAlSiO}_4\text{-Si}_3\text{N}_4$  systems after a holding time of 5 min.

In both systems, there is a lag between densification and phase transformation showing that the major amount of transformation occurs in a later sintering stage. At  $1400^\circ\text{C}$ , almost no

transformation is observed, while more than 90 % and 80 % of the theoretical density have already been reached for the  $\text{LiYO}_2$  and  $\text{LiAlSiO}_4$  additives, respectively. At higher temperatures, the differences in the degree of densification and phase transformation become smaller in case of the  $\text{LiYO}_2$  additive, while it is at  $1700^\circ\text{C}$  still present in case of the  $\text{LiAlSiO}_4$  additive.

Fig. 6.8 depicts the relationships between densification and phase transformation as a function of sintering time for both types of materials. In both cases, the differences in the degree of densification and phase transformation diminish with prolonged heating time. Both processes are particularly fast in the  $\text{LiYO}_2\text{-Si}_3\text{N}_4$  system where the densification and phase transformation have gone to completion after 60 minutes already.

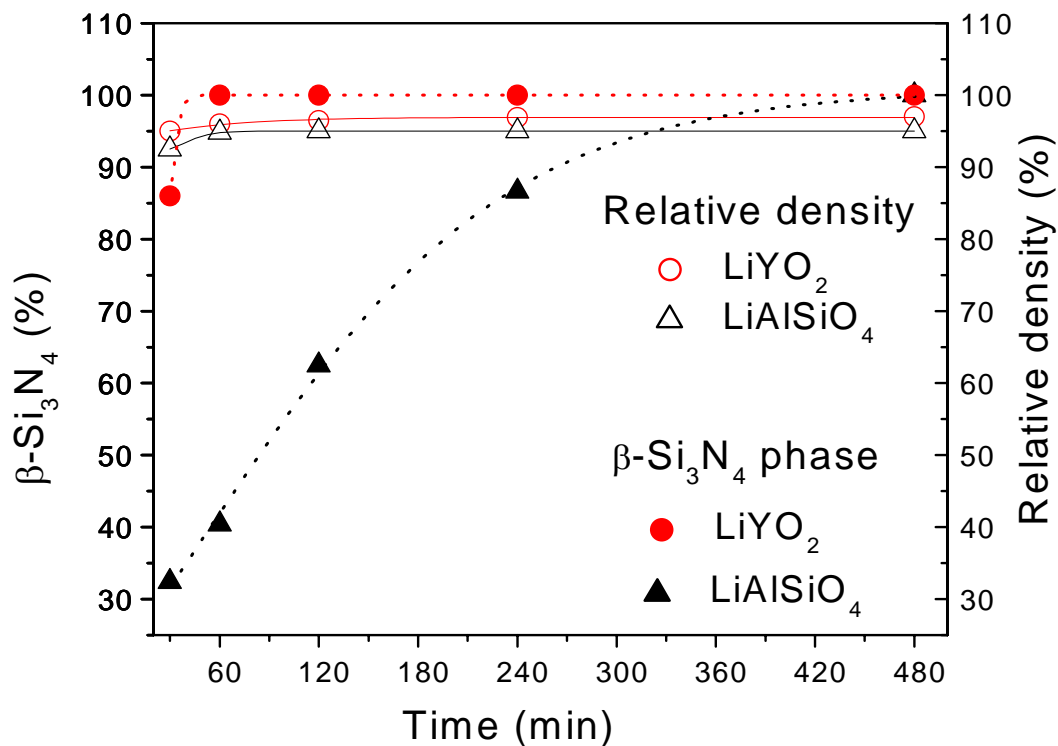


**Fig. 6.8 :** The relationship between densification and phase transformation as a function of sintering time for  $\text{LiYO}_2\text{-Si}_3\text{N}_4$  and  $\text{LiAlSiO}_4\text{-Si}_3\text{N}_4$  additive systems (with 15 wt% of additive and at a sintering temperature of  $1500^\circ\text{C}$ ).

The addition of  $Y_2O_3$  to silica produces an important accelerating effect on both, transformation and densification of  $Si_3N_4$  ceramics [152]. In this case, higher additive content creates a less viscous liquid phase resulting in faster  $\alpha \rightarrow \beta$  phase transformation and higher densities obtained (chapter 5). In the  $LiAlSiO_4$  system the densification and transformation behavior is more complicated and it needs more work to clarify the details.

## 7 MICROSTRUCTURE

The microstructure has a crucial influence on the particular properties of a final material. Thus, the improvement of mechanical properties by microstructural control has been one of the main topics of interest in the development of  $\text{Si}_3\text{N}_4$  ceramics. [159, 160]. The amount, size and morphology of the  $\alpha$ - and  $\beta$ - $\text{Si}_3\text{N}_4$  grains are the key factors for the microstructure development. Generally, the microstructure is characterized by the three features:  $\text{Si}_3\text{N}_4$  grains, the secondary crystalline phases and the amorphous grain boundary films. Their distribution and arrangement contribute to the quality of the actual microstructure and the reliability of the material. In this chapter the various factors influencing the microstructure development, grain growth and the relation of phase transformation to microstructure are dealt with.

### 7.1 Microstructural observation in systems sintered with $\text{LiYO}_2$ additive

The microstructures of LPS- $\text{Si}_3\text{N}_4$  sintered with  $\text{LiYO}_2$  additive at  $1500^\circ\text{C}$  for different annealing time are shown in Fig. 7.1. Upon variation of the annealing time the grain size and morphology of the growing  $\beta$ - $\text{Si}_3\text{N}_4$  particles are significantly changed from equiaxed to elongated. Typically, the fraction of small grain sections is reduced, which indicates the dissolution of small particles parallel to the growth of the elongated  $\text{Si}_3\text{N}_4$ -matrix with increasing annealing time. According to these results it is suggested that the mechanism of Ostwald ripening is predominantly responsible for grain growth in the  $\text{Si}_3\text{N}_4$  material. This is independent of whether this growth mechanism is reaction or diffusion controlled [161]. Since the phase transformation is completed after 1 h of annealing at  $1500^\circ\text{C}$  (Fig. 6.1), the further grain growth of  $\beta$ - $\beta$ - $\text{Si}_3\text{N}_4$  should be restricted, resulting in a relatively stable microstructure [162]. However, in spite of the absence of  $\alpha$ - to  $\beta$ - $\text{Si}_3\text{N}_4$  transformation during prolonged annealing, there is still substantial grain growth of the  $\beta$ - $\text{Si}_3\text{N}_4$  (Fig. 7.1. c). This indicates ongoing solution-precipitation reaction [163]. Ongoing solution-precipitation process may attributed to the fact that the  $\text{LiYO}_2$  melt is such a good solvent for  $\text{Si}_3\text{N}_4$ . Fig. 7.2 taken at higher magnification shows that the precipitation takes place preferentially on pre-existing  $\beta$ - $\text{Si}_3\text{N}_4$  nuclei (of which the starting powder already contains 20 wt%).

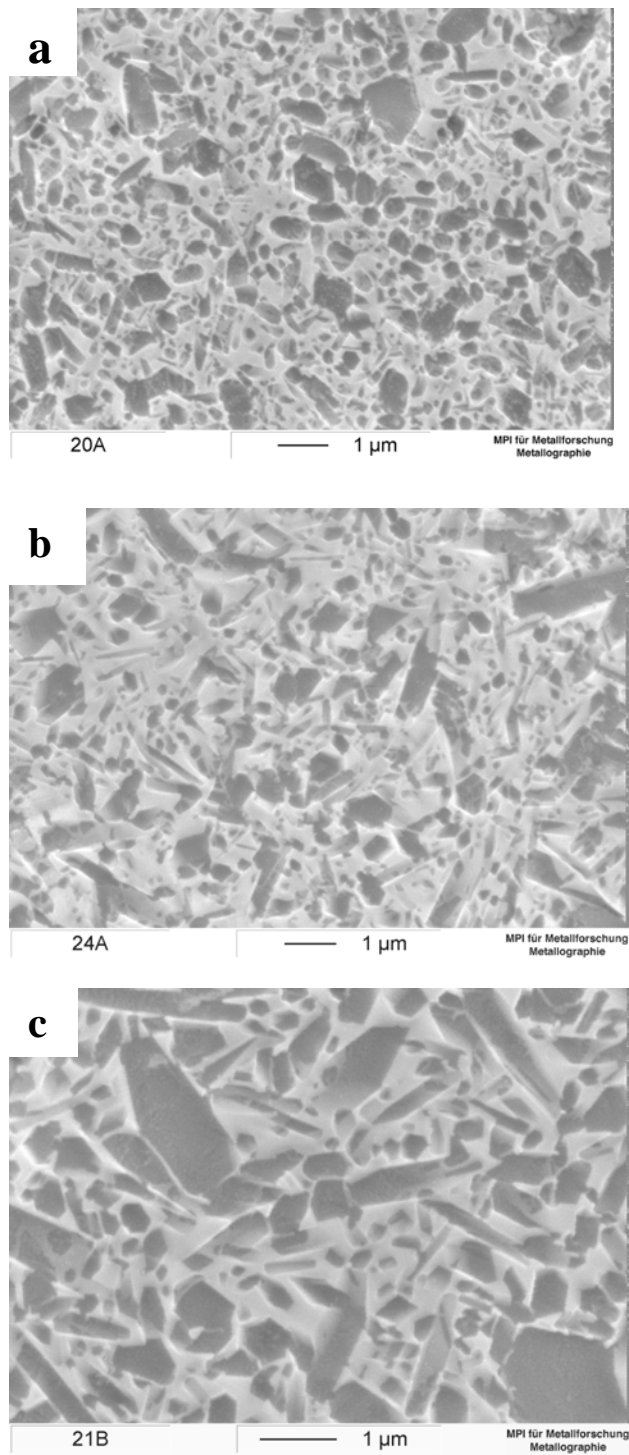


**Fig. 7.1:** SEM micrograph of polished and plasma etched sections of samples with 15 wt% additive sintered at 1500 °C for 0.5 h (a), 2 h (b) and 8 h (c); Magnifications 10000x.

The observation that  $\beta$ - $\text{Si}_3\text{N}_4$  undergoes a solution-precipitation mechanism similar to what was previously reported for  $\alpha$ - $\text{Si}_3\text{N}_4$  is also in good agreement with model predictions for anisotropic Ostwald ripening process [164].

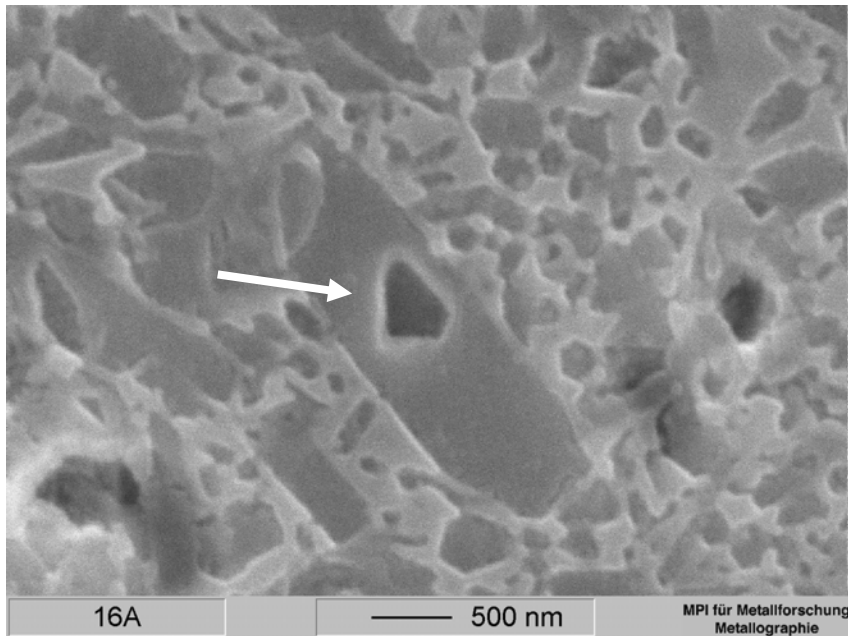


**Fig. 7.2:** SEM image of polished and  $\text{CF}_4$  plasma-etched cross section of the sintered  $\text{Si}_3\text{N}_4$  material doped with  $\text{LiYO}_2$  additive. The arrow shows  $\beta$ - $\text{Si}_3\text{N}_4$  material precipitated on a  $\beta$ - $\text{Si}_3\text{N}_4$  particle acting as a nucleus. The sample was sintered at  $1500^\circ\text{C}$  for 2 h; Magnification  $23000\times$ .

Since the densification as well as the phase transformation is influenced by the additive content, the same has to be true for the microstructure development. Fig. 7.3 shows SEM micrographs with varying additive content. It can be seen that the number and aspect ratio of elongated  $\beta$ -grains increases with increasing  $\text{LiYO}_2$  content. The material with a large additive content is mainly composed of elongated grains. In contrast, with a small additive content, microstructure consists of coarse  $\beta$ -grains within a fine grain matrix. Thus, with increasing additive content, the aspect ratio distribution is shifted to higher values.



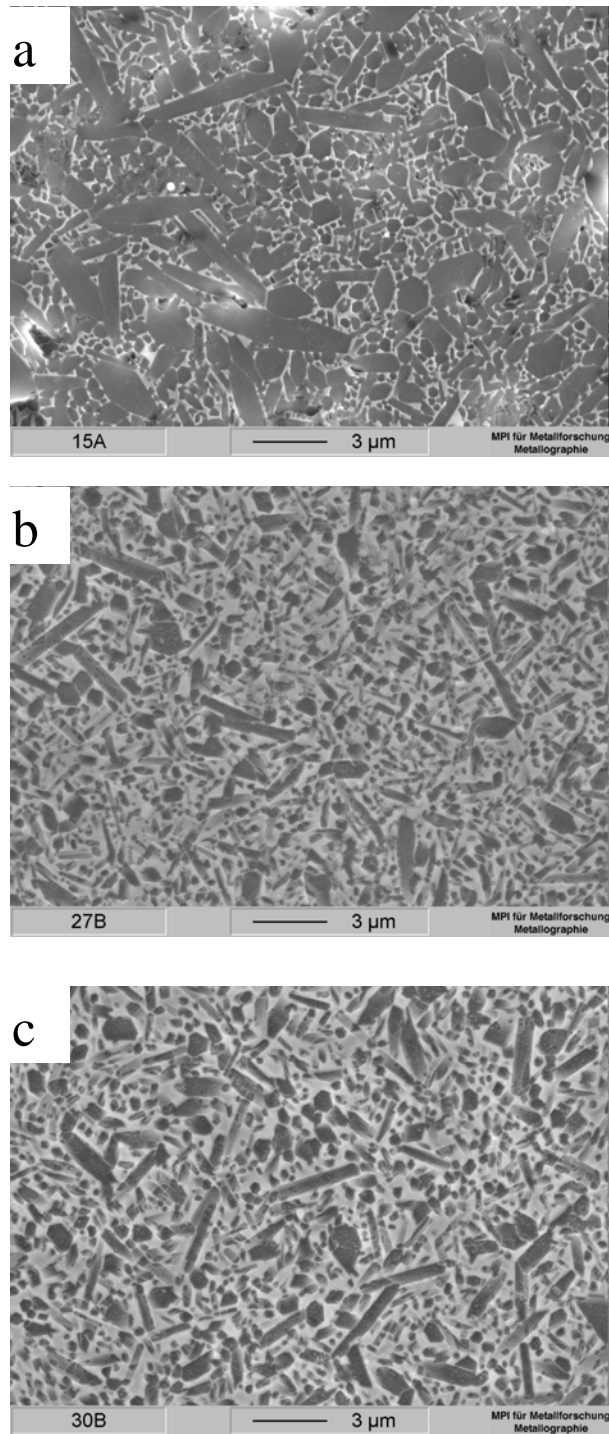


**Fig.7.3:** SEM microstructure of  $\text{Si}_3\text{N}_4$  ceramics with total  $\text{LiYO}_2$  additive content of (a) 5 wt%, (b) 15 wt%, (c) 20 wt%, respectively. The samples were sintered at 1600 °C for 4 h.

The microstructure of  $\text{Si}_3\text{N}_4$  with 15 wt% of additive sintered at  $1600^\circ\text{C}$  for 8 h is characterized by a homogeneous distribution of elongated  $\beta\text{-Si}_3\text{N}_4$  grains (dark) and glassy phase (light) located in thin layers at grain boundaries and triple points (Fig. 7.4). The  $\beta\text{-Si}_3\text{N}_4$  grains are surrounded by a glassy phase at almost all grain contacts indicating a good wetting behavior. The different types of neighbour-neighbour contact situations can be attributed to the grain growth anisotropy of  $\text{Si}_3\text{N}_4$  such as interlocking of a growing plane by the plane of a neighboring grain (a) and interlocking of a plane growing through the intergranular phase (b) and rounded edges due to edge-on-plane contact with an adjacent grain can also be seen (c).

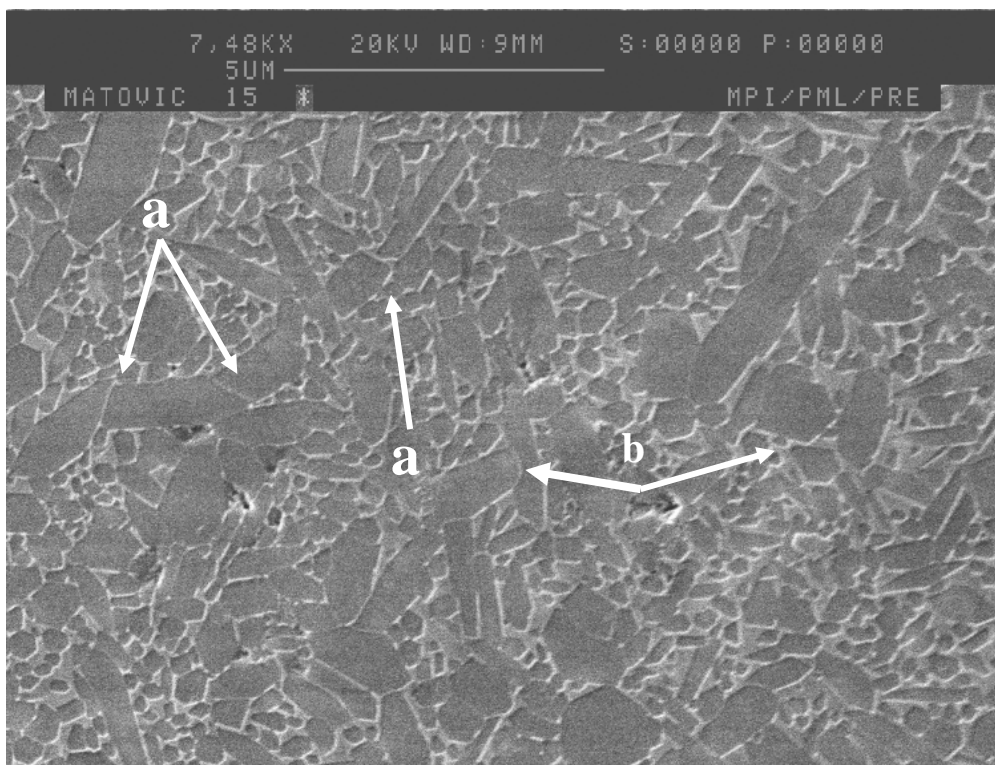


**Fig. 7.4:** SEM micrograph of polished and plasma etched section of a sample with 15 wt% additive sintered at  $1600^\circ\text{C}$  for 8 h. Motion of basal and prism planes : (a) interlocking of two prism planes, (b) rounded planes contacting each other.

X-ray diffraction patterns of samples sintered at  $1600^\circ\text{C}$  for 8 h show only the presence of  $\beta\text{-Si}_3\text{N}_4$  and no other crystalline phases (Fig. 7.5). This indicates that the remainder of the secondary phase, after evaporation of virtually all of the lithium originally present in the

sample, has been completely converted into a glass and that total conversion of  $\alpha$ - $\text{Si}_3\text{N}_4$  to  $\beta$ - $\text{Si}_3\text{N}_4$  has taken place.

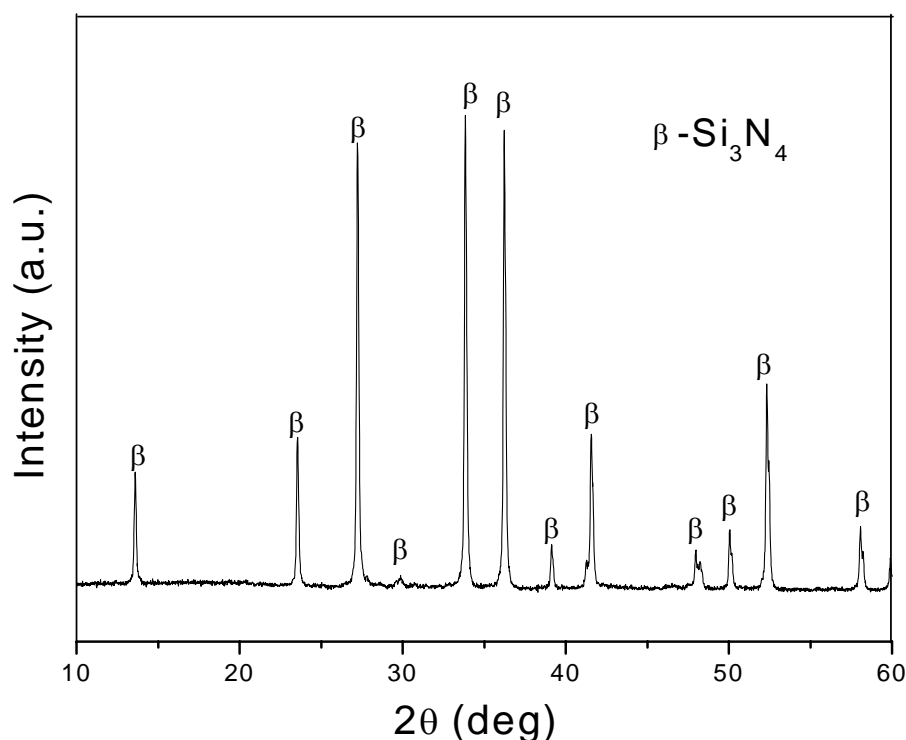


**Fig. 7.5:** XRD pattern of a sample with 15 wt% of additive sintered at 1600 °C for 8 h.

The amorphous phase in the  $\text{Si}_3\text{N}_4$  materials is well-established to remain as a stable film at the grain boundaries [165], with an increasing additive content only causing an enlargement of the multi-grain junctions. For the present materials, the chemistry of the intergranular phase and  $\beta$ -grain was analysed by energy dispersive microanalysis (EDX) with the SEM (Fig. 7.6 and Fig. 7.7). Backscattered electron (BSE) images are shown for reference. EDX analysis on the basal plane of a  $\beta$ - $\text{Si}_3\text{N}_4$  grain (denoted by cross in the Fig. 7.6) shows Si and N, but no Y. This is because Y is insoluble in  $\text{Si}_3\text{N}_4$  [132]. Consequently,  $\text{Y}_2\text{O}_3$  is localized in the grain-boundary glassy phase. Lithium is not detected by this method because it is a light element. However, chemical analyzes show that almost all of the  $\text{Li}_2\text{O}$  from the samples evaporates during sintering for 8 h at 1500°C (Fig. 5.14). Thus, at higher temperatures than 1500°C there is no lithium and the intergranular phase consists of Y, Si, N and O. This is in good agreement with chemical analyses from the big pocket in the Fig. 7.7, after 1 h at 1650°C

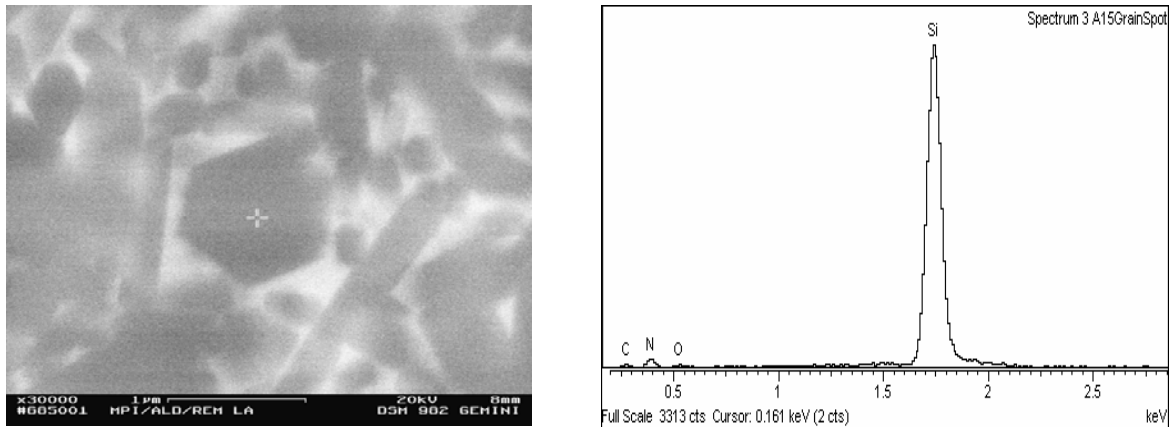


**Fig. 7.6:** Backscattered electron image and EDX of  $\beta$ - $\text{Si}_3\text{N}_4$  grain (+). Sample sintered at  $1650^\circ\text{C}$  for 1 h.

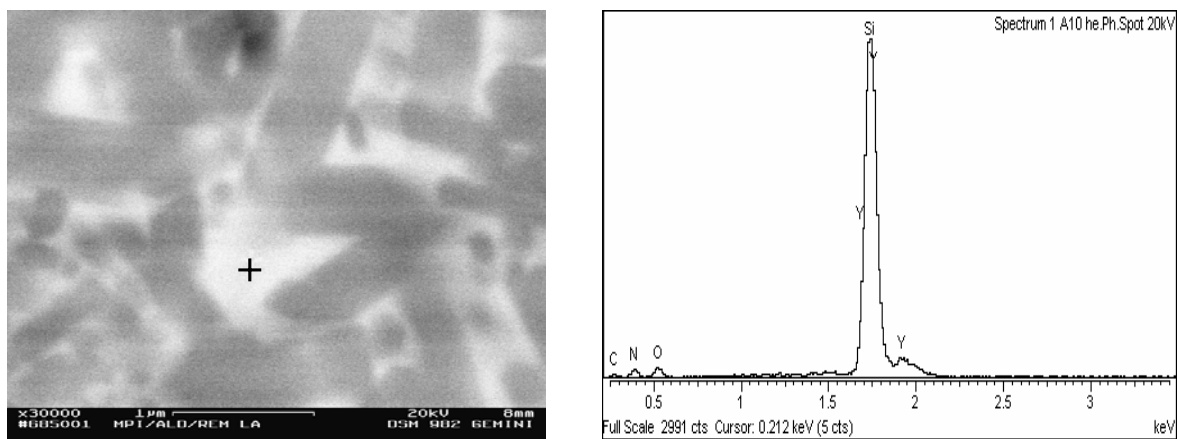


**Fig. 7.7:** Backscattered electron image and EDX of intergranular phase (+). Sample sintered at  $1650^\circ\text{C}$  for 1 h.

## 7.2 Microstructural observation in systems sintered with $\text{LiAlSiO}_4$ additives

Fig. 7.8 shows a SEM micrograph of a  $\text{Si}_3\text{N}_4$  ceramic doped with 15 wt% of  $\text{LiAlSiO}_4$  sintered at  $1500^\circ\text{C}$  for 8 h. The microstructure consists of  $\text{Si}_3\text{N}_4$  grains separated by glassy phase. Although the  $\alpha \rightarrow \beta$   $\text{Si}_3\text{N}_4$  phase transformation is completed at  $1500^\circ\text{C}$  after 8 h of annealing time (Fig. 6.4), there are no bimodal grains. The morphology of the grains is mostly globular. Plasma etched samples reveal a typical core and rim structure which indicates the dissolution of small particles and reprecipitation on more stable bigger ones.

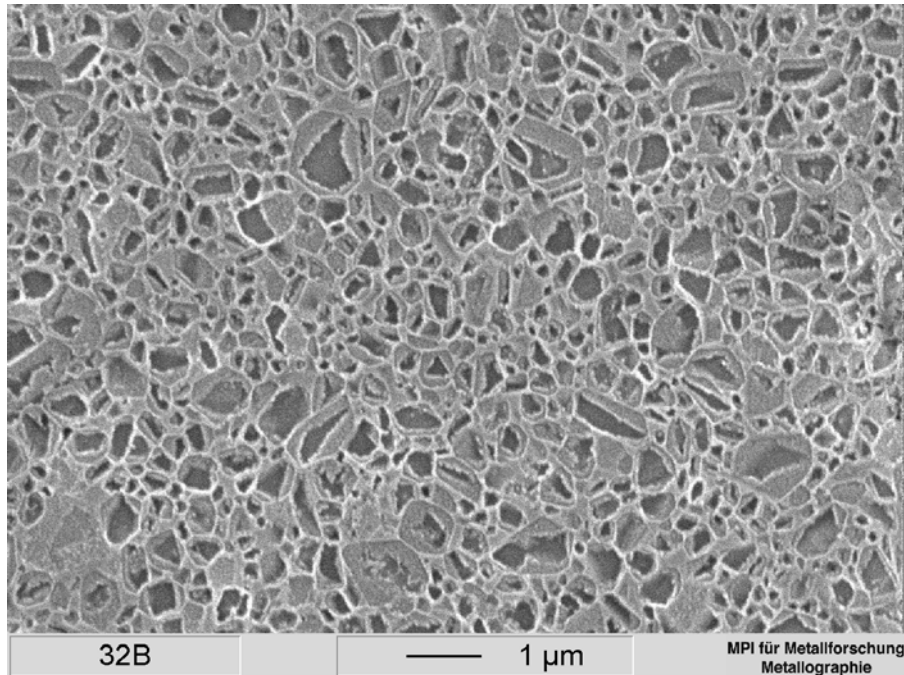


**Fig. 7.8:** SEM micrograph of polished and plasma etched section of a sample with 15 wt% of  $\text{LiAlSiO}_4$  additive sintered at 1500 °C for 8 h.

The microstructure of  $\text{Si}_3\text{N}_4$  sintered at 1550°C for 8 h is characterized by both equiaxed  $\beta$ - $\text{Si}_3\text{N}_4$  grains and elongated  $\beta$ - $\text{Si}_3\text{N}_4$  grains together with a glassy phase (white) located in thin layers at grain boundaries. During processing at 1600°C significant differences in the microstructures of the ceramics were developed. Higher temperature enhances the grain growth resulting in a microstructure with elongated  $\beta$ - $\text{Si}_3\text{N}_4$  grains (Fig. 7.9, 7.10). Materials with larger additive content (15 wt%) exhibit finer microstructure. The number of coarse elongated  $\beta$ - $\text{Si}_3\text{N}_4$  grains decreases with the increase in  $\text{LiAlSiO}_4$  content. It seems that the growth of  $\text{Si}_3\text{N}_4$  grains during sintering is restrained by the higher  $\text{LiAlSiO}_4$  content.

At 1650°C it is noticed that the amount of residual glass is become very low, indicating that aluminum and/or oxygen has been incorporated into the  $\beta$ -grains (Fig. 7.1).

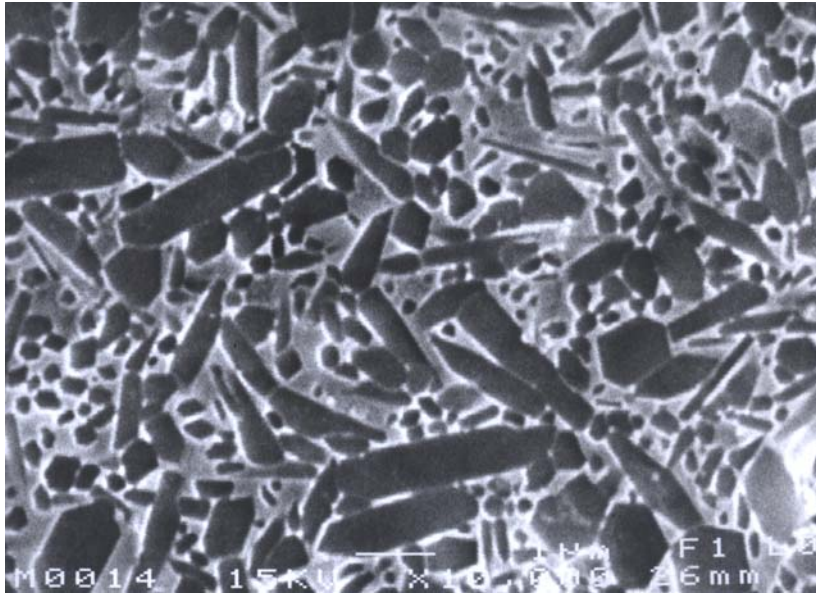


*Fig. 7.9 : SEM micrograph of a polished and plasma etched section of a sample sintered with 10 wt% of additive at 1600 °C for 8 h.*

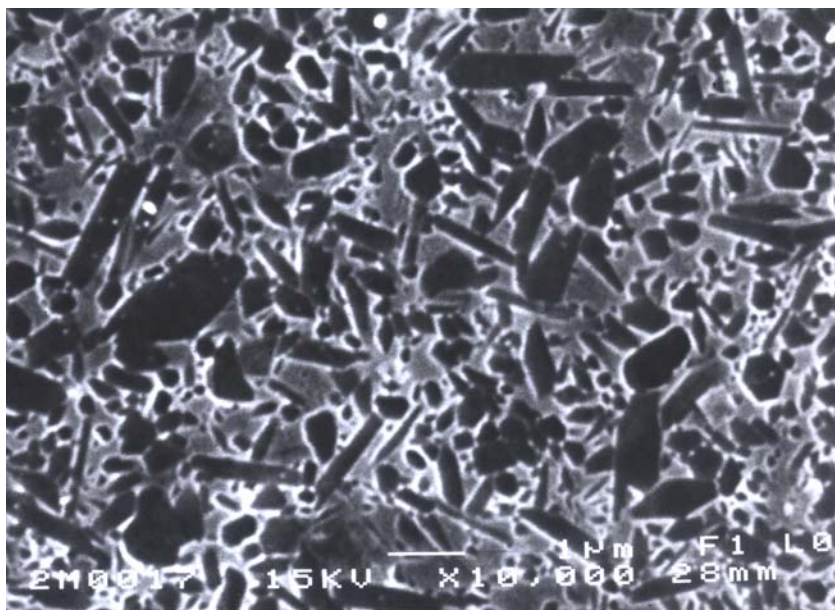


*Fig. 7.10 : SEM micrograph of a polished and plasma etched section of a sample sintered with 15 wt% of additive at 1600 °C for 8 h.*

EDX analysis of the sample sintered at 1650°C for 1 h showed that Al was dissolved in the  $\beta$ - $\text{Si}_3\text{N}_4$  grains. This process consumes the constituents of the liquid phase, thereby reducing the volume of the liquid phase as well as altering its composition. The liquid phase shifts to a more

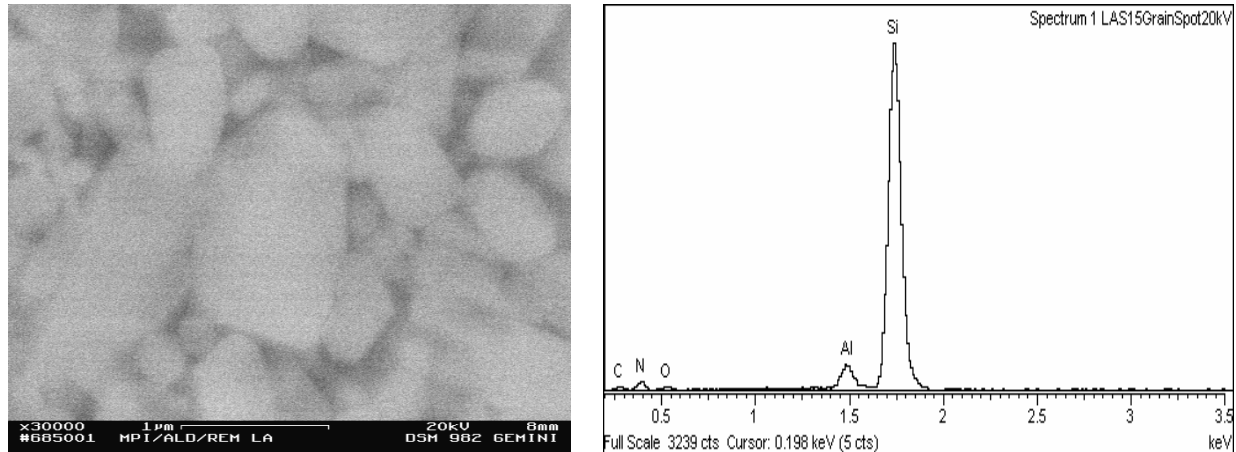


**Fig. 7.11:** Backscattered electron images and EDX of  $\beta$ - $\text{Si}_3\text{N}_4$  grain. Sample is sintered at 1650°C for 1 h.

siliceous composition and hence to higher viscosity. Thus higher viscosity leads to a retardation of the grain-boundary diffusion processes, and therefore limits mass transport. This reduction in mass transport results in a retarded grain growth and the microstructure do not change in the case of the samples sintered at 1650°C even for extended time intervals (Fig. 7.11).

To conclude, the material sintered with the  $\text{LiAlSiO}_4$  additive forms a  $\beta$ -Sialon due to the incorporation of  $\text{Al}_2\text{O}_3$  in the  $\beta$ - $\text{Si}_3\text{N}_4$  structure. This is expected to have a marked influence on the properties especially of the material sintered at higher temperatures (>1600°C).

## 8 PROPERTIES

$\text{Si}_3\text{N}_4$  based ceramics have a broad variety of interesting properties such as low specific weight, good mechanical and thermomechanical behavior. They are also non-magnetic and good electrical insulation material. These unique properties allow fabrication of a wide range of materials with specified property combination.

### 8.1 Fracture toughness and hardness

The hardness and indentation fracture toughness of both types of materials were measured and plotted against the annealing time (Fig. 8.1).

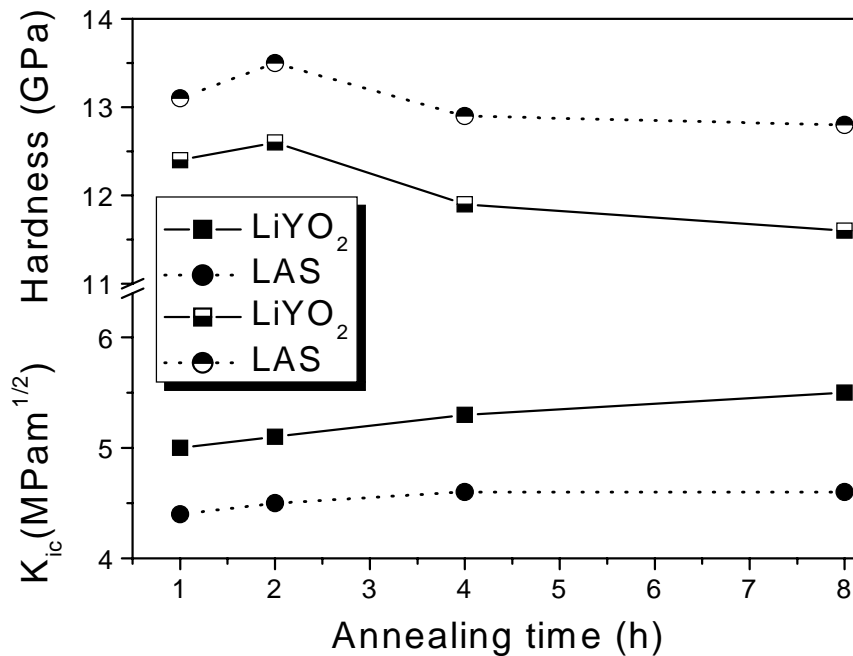


**Fig. 8.1:** Variation of fracture toughness and hardness as a function of the annealing time in  $\text{Si}_3\text{N}_4$  ceramics sintered with  $\text{LiYO}_2$  and  $\text{LiAlSiO}_4$  additive systems, respectively at  $1500\text{ }^\circ\text{C}$ .

In both compositions, the fracture toughness and hardness initially increase with increasing annealing time, whereas decreasing hardness is observed in case of annealing for at least 4 hours. Further prolongation of the sintering time leads to constant or decreasing hardness for both  $\text{LiAlSiO}_4$  and  $\text{LiYO}_2$  additives. On the other side, the fracture toughness continuously grows during prolonged annealing time for the  $\text{LiYO}_2$  additive, while this behaviour is less



pronounced in case of  $\text{LiAlSiO}_4$  additive. In this case it becomes constant after 4 hours of annealing.

Variations in the fracture toughness of  $\text{Si}_3\text{N}_4$  materials sintered with  $\text{LiYO}_2$  and  $\text{LiAlSiO}_4$  additives should be related to the microstructures and glassy phase contents. Fracture toughness is improved when large elongated grains are formed in a fine matrix [166, 167]. In case of the  $\text{LiYO}_2$  additive the fracture toughness increased with sintering time as a result of the continuous growth of elongated grains (Fig. 7.1). On the other hand, materials sintered with  $\text{LiAlSiO}_4$  additive at  $1500^\circ\text{C}$  exhibit fine and predominantly equiaxed  $\beta\text{-Si}_3\text{N}_4$  grains which do not change during long annealing times (Fig. 7.8 ) resulting in a constant value of fracture toughness.

The microstructural effects on the fracture toughness are well illustrated by crack paths generated by indentation, as shown in Figs. 8.2 and 8.3.

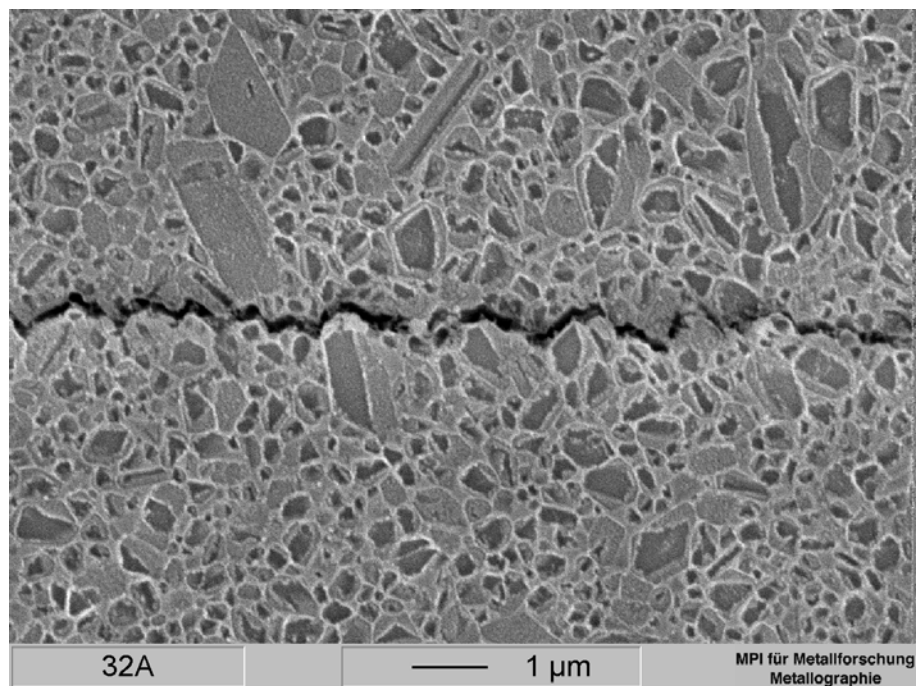


**Fig. 8.2:** Microstructure and crack path in  $\text{Si}_3\text{N}_4$  ceramic sintered with 15 wt% of  $\text{LiAlSiO}_4$  additive at  $1500^\circ\text{C}$  for 8 h.

Materials with globular grain structure reveal crack propagation with few signs of toughening mechanisms, such as crack deflection, grain pullout, debonding and bridging. On the other hand, microstructures with elongated grains that can act as a reinforcing phase promote crack bridging processes and consequently toughen the ceramics. Such mechanisms are operative in

both the cases of  $\text{LiYO}_2$  and  $\text{LiAlSiO}_4$  additives, for samples sintered at  $1600^\circ\text{C}$ , due to their similar microstructures (see chapter 7).

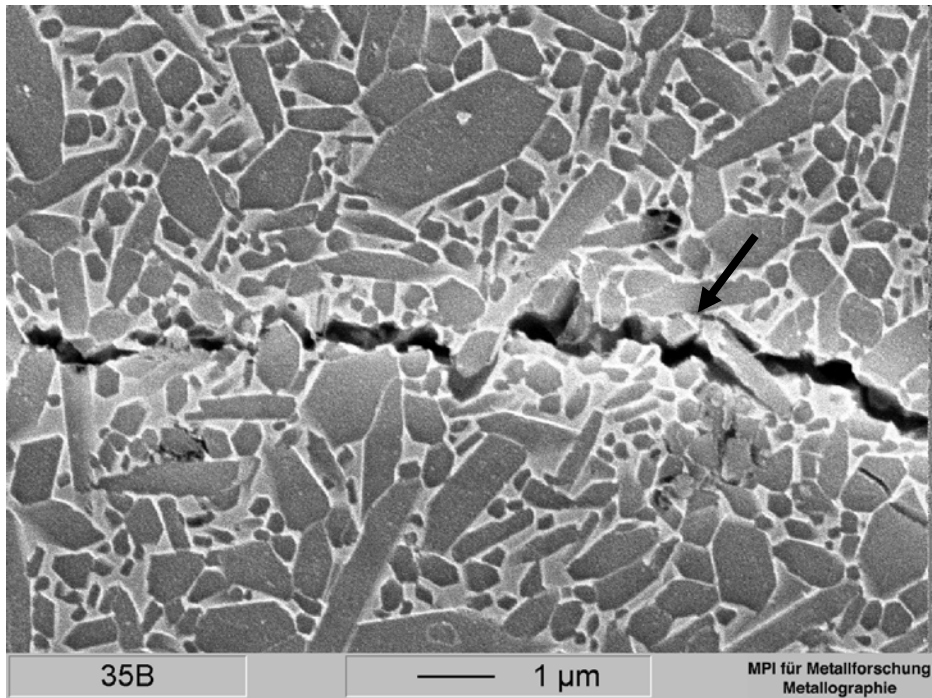


**Fig. 8.3:** Microstructure and crack path in  $\text{Si}_3\text{N}_4$  ceramic sintered with 15 wt% of  $\text{LiYO}_2$  additive at  $1600^\circ\text{C}$  for 8 h. The crack is bridged by an elongated grain (arrow,) which was pulled out of the matrix on the upper side of the crack as the crack opened.

The maximum values of fracture toughness obtained are  $6.8$  and  $6.2 \text{ MNm}^{3/2}$  for the materials sintered with  $\text{LiYO}_2$  and  $\text{LiAlSiO}_4$  additives, respectively, at  $1600^\circ\text{C}$  for 8 h.

## 8.2 Thermal conductivity

Both thermal and mechanical properties are important for high-temperature structural application of  $\text{Si}_3\text{N}_4$  ceramics. High thermal conductivity is a necessary prerequisite for good thermal shock resistance. Controlling factors for the heat conductivity of  $\text{Si}_3\text{N}_4$  based materials have been proposed by numerous researchers [168]. The factors are divided into two groups : (a) microstructure effects and (b) crystalline perfection. Since the  $\text{LiYO}_2$  additive is not soluble in  $\text{Si}_3\text{N}_4$ , as it is the case with  $\text{LiAlSiO}_4$  additive, ceramics sintered with these additives should be significantly different.

The influence of additive composition on thermal diffusivity of the sintered  $\text{Si}_3\text{N}_4$  materials is shown in Fig. 8.5 a and b. The thermal conductivity with the  $\text{LiYO}_2$  additive is higher in comparison with the  $\text{LiAlSiO}_4$  additive. Since the thermal conductivity of covalent materials is mainly due to phonons, it is controlled by the type and amount of crystal defects inside the grains.

EDX analyses of the sample sintered with  $\text{LiAlSiO}_4$  at  $1650^\circ\text{C}$  for 1 h showed that Al was dissolved in the  $\beta\text{-Si}_3\text{N}_4$  grains (Fig. 7.11). Dissolved Al and O act as point defects scattering phonons [169] and hence decrease the thermal conductivity. The thermal diffusivity significantly decrease with increasing temperature in both sintered materials (Fig. 8.5). The main reason is increasing phonon scattering due to the higher vibrational energy. However, the decrease in thermal diffusivity and conductivity is more pronounced in case of the  $\text{LiAlSiO}_4$  additive due to a higher phonon density of states associated with partially occupied interstitial sites in  $\beta\text{-Sialon}$ .

The effect of additive content on the thermal conductivity of  $\text{Si}_3\text{N}_4$  ceramics sintered with 5-20 wt% of  $\text{LiYO}_2$  additive at  $1650^\circ\text{C}$  for 4 h is tabulated in Table 8-I.

*Table 8-I: The effect of additive amount on the thermal conductivity of  $\text{Si}_3\text{N}_4$  ceramics sintered with  $\text{LiYO}_2$  additive.*

Additive content (wt%)	Density ( $\text{g}/\text{cm}^3$ )	Thermal conductivity ( $\text{W}/\text{m}\cdot\text{K}$ )
5	2.85	38.6
10	3.12	29.1
15	3.21	29.7
20	3.20	26.8

In spite of the low density (high porosity), a higher value of thermal conductivity is obtained for materials sintered with only 5 wt% of additive. Increasing the additive content reduces the thermal conductivity. Since the phase composition and grain-boundary phase are the same, the difference in the thermal conductivity is attributed to the variation in the microstructure.

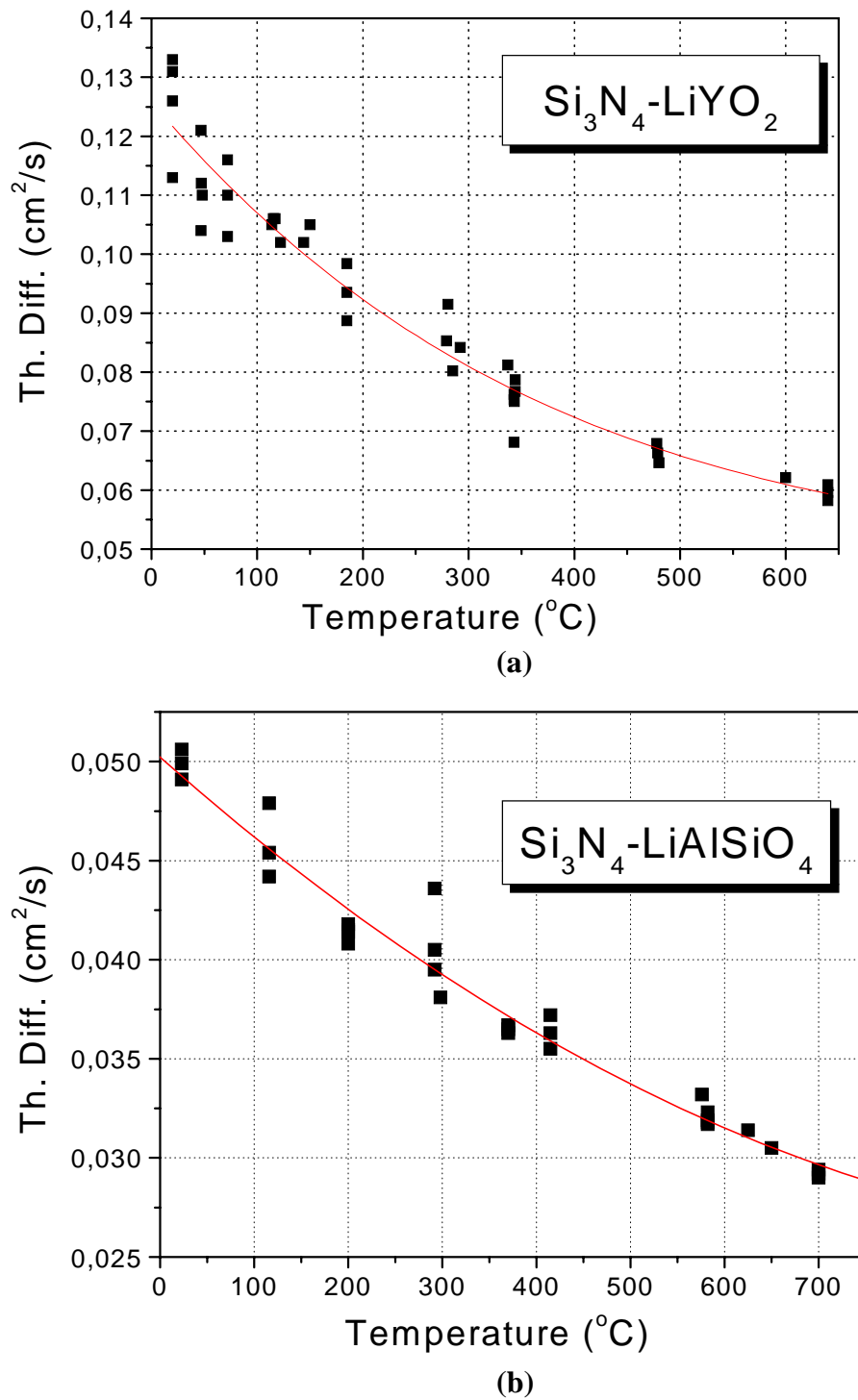


**Fig. 8.5:** Temperature dependence of thermal diffusivity of  $\text{Si}_3\text{N}_4$  ceramics sintered with 15 wt% of  $\text{LiYO}_2$  (a) and  $\text{SiAlSiO}_4$  (b) additive.

Considering the thermal conductivity of  $\text{SiO}_2$  based glasses, the thermal conductivity of the intergranular phase is much lower than that of  $\text{Si}_3\text{N}_4$  grains, ranging from 0.1 to 0.7 W/m·K

[170]. Thus,  $\text{Si}_3\text{N}_4$  ceramics can be considered as a two-phase materials composed of the  $\text{Si}_3\text{N}_4$  grains with high thermal conductivity and the intergranular phase with low thermal conductivity. The thermal conductivity of two-phase materials depends on the individual thermal conductivity of the phases and on their distribution. In the case of higher additive contents, the amount of glassy phase in the grain-junction is higher which results in a decreasing overall thermal conductivity.

## CONCLUSIONS

Pressureless sintering of  $\text{Si}_3\text{N}_4$  with two new additives based on the  $\text{Li}_2\text{O}-\text{Y}_2\text{O}_3$  system ( $\text{LiYO}_2$ ) and on the  $\text{Li}_2\text{O}-\text{Al}_2\text{O}_3-\text{SiO}_2$  system ( $\text{LiAlSiO}_4$ ) were investigated in this study. Experiments were conducted in the areas of powder processing, sintering optimization, phase transformation characterization and microstructural development. Sintered materials were characterized by fracture toughness and thermal diffusivity measurements. The experimental results are summarized in the following:

1. Using three different mechanical mixing processes (attrition milling, ball milling and vibratory milling) for the introduction of additives ( $\text{LiYO}_2$ ) into  $\text{Si}_3\text{N}_4$  powders, the best results are obtained for attrition milling. This method yields a good dispersion of the additive powder in fine unagglomerated  $\text{Si}_3\text{N}_4$  without contamination. It also yields good sintering characteristics.
2. For the  $\text{LiYO}_2$  system, the densification depends largely on the content of sintering additive. A larger amount of additive means a higher volume of liquid phase, which is favorable for efficient particle rearrangement resulting in higher values of density rate. In case of the  $\text{LiAlSiO}_4$  additive, it is found that the densification is less dependent on the additive content.
3. The overall sintering kinetics at the low temperatures is less retarded when using the  $\text{LiYO}_2$  additive in comparison to the  $\text{LiAlSiO}_4$  additive, resulting in higher densities obtained at lower temperatures and shorter annealing times. With prolonged heating time, the differences in the degree of densification become smaller.
4. The kinetics of phase transformation in the both systems are found to be of first order.
5. In the  $\text{LiYO}_2$  system, the transformation rate constant increases with increasing additive content. While the opposite behavior is noticed in case of the  $\text{LiAlSiO}_4$  additive, i.e. the rate constant decreases with higher additive content.
6. The phase transformation is always completed at a later stage than the densification. The lag between the two phenomena in the sintering process is more pronounced with the  $\text{Li}_2\text{O}-\text{Al}_2\text{O}_3-\text{SiO}_2$  additive system.

7. The  $\alpha \rightarrow \beta$   $\text{Si}_3\text{N}_4$  transformation is accompanied by grain growth. Upon prolongation of the annealing time the grain size and the morphology of the growing  $\beta$ - $\text{Si}_3\text{N}_4$  particles are significantly changed from equiaxed to elongated. The grain growth becomes anisotropic, leading to rod-like  $\beta$ - $\text{Si}_3\text{N}_4$  crystals. The growth rate is higher in the  $\text{LiYO}_2$  system than in the  $\text{LiAlSiO}_4$  system.
8. At  $1600^\circ\text{C}$ , the microstructure of  $\text{Si}_3\text{N}_4$  ceramics sintered with both the additives is characterized by a homogeneous distribution of elongated  $\beta$ - $\text{Si}_3\text{N}_4$  grains and glassy phase located in thin layers at grain boundaries and at triple points.
9. The maximum values obtained for fracture toughness are 6.8 and 6.2 for the materials sintered with  $\text{LiYO}_2$  and  $\text{LiAlSiO}_4$  additives, respectively, at  $1600^\circ\text{C}$  for 8 h. The higher value of fracture toughness in the  $\text{LiYO}_2$  system is attributed to its microstructure with a higher aspect ratio of the elongated  $\beta$ - $\text{Si}_3\text{N}_4$  grains
10. Thermal conductivity of the material sintered with the  $\text{LiYO}_2$  additive is higher in comparison to that sintered with  $\text{LiAlSiO}_4$  additive. In the  $\text{LiAlSiO}_4$  system, partial dissolution of  $\text{Al}^{3+}$  in the  $\beta$ - $\text{Si}_3\text{N}_4$  grains results in increasing phonon scattering and hence decreases the thermal conductivity.

## ZUSAMMENFASSUNG

### Niedertemperatur-Sinterzusätze für Siliciumnitrid

$\text{Si}_3\text{N}_4$ -Keramiken sind bekannt für ihre hohe Festigkeit, ihren guten Thermoschockwiderstand auf Grund des geringen thermischen Ausdehnungskoeffizienten, und ihre relativ gute Widerstandsfähigkeit gegenüber Oxidation verglichen mit anderen Hochtemperatur-Strukturmaterialien.

Siliziumnitrid-Keramiken werden für Strukturanwendungen bei Raumtemperatur und bei hohen Temperaturen verwendet. Trotz der exzellenten Eigenschaften von  $\text{Si}_3\text{N}_4$  sind dem Einsatz von Siliciumnitrid-basierten Keramiken derzeit noch Grenzen gesetzt. Den Hauptgrund stellen die hohen Kosten im Hinblick auf Rohmaterial, Zusätze und Produktionsprozeß dar. Die Wirtschaftlichkeit von Siliziumnitrid-Produkten kann durch Senkung der Kosten für Ausgangsmaterialien und durch Erniedrigung der Sintertemperatur verbessert werden.

Diese Arbeit beschäftigt sich mit Sinterzusätzen für das drucklose Sintern von  $\text{Si}_3\text{N}_4$  bei möglich niedrigen Temperaturen mittels einer sogenannten "transient liquid"-Technik. Große Aufmerksamkeit wurde der Entwicklung eines Sinterprozesses geschenkt, der preisgünstiges  $\text{Si}_3\text{N}_4$ -Pulver (Silzot QH, Firma SKW Trosberg, Deutschland) als Ausgangsmaterial benutzt und Sinterzusätze verwendet, die sowohl wirtschaftlich attraktiv sind als auch das Sintern bei tiefen Temperaturen ermöglichen. Zwei neue Zusätze basierend auf dem  $\text{Li}_2\text{O}-\text{Y}_2\text{O}_3$ -System ( $\text{LiYO}_2$ ) und auf dem  $\text{Li}_2\text{O}-\text{Al}_2\text{O}_3-\text{SiO}_2$ -System ( $\text{LiAlSiO}_4$ ) wurden in dieser Arbeit untersucht.

Zunächst wurden verschiedene Prozesse zur Homogenisierung der Pulvergemische untersucht. Dies war notwendig, weil sich die Korngrößen- und Kornformverteilungen des untersuchten  $\text{Si}_3\text{N}_4$ -Pulvers deutlich von normalerweise zum Flüssigphasensintern von  $\text{Si}_3\text{N}_4$  verwendeten Pulvern unterscheiden.

Ausgangsmaterial für die Grünkörperherstellung war das kommerzielle  $\text{Si}_3\text{N}_4$ -Pulver SILZOT HQ (SKW Metallchemie GmbH; mittlere Teilchengröße  $D_{50} = 1.7 \mu\text{m}$ ; spezifische Oberfläche  $3.2 \text{ m}^2/\text{g}$ ;  $\alpha/(\alpha+\beta)\text{-Si}_3\text{N}_4 = 0.8$ ; Masse-% O = 0.5, N > 38.5, freies Si < 0.5, SiC < 0.4). Es handelt sich um ein kostengünstiges Pulver, das durch ein modifiziertes Direktnitridierungsverfahren aus einer hochreinen Silicium-Qualität hergestellt wird.



Das Sinteradditiv  $\text{LiYO}_2$  wurde durch Mischen kommerziell bezogener  $\text{Y}_2\text{O}_3$  und  $\text{Li}_2\text{CO}_3$ -Pulver und Calcinieren bei  $1400^\circ\text{C}$  für 4 h synthetisiert. Durch Röntgen-Pulverdiffraktometrie (XRD) des calcinierten Pulvers wurde nachgewiesen, dass es sich um phasenreines  $\text{LiYO}_2$  handelte.

Das Additiv  $\text{LiAlSiO}_4$  wurde über eine Ionenaustauschreaktion aus Zeolithen hergestellt. Diese kostengünstige Methode führt zu einem amorphen Produkt, das im Vergleich zu entsprechenden kristallinen Phasen eine hohe chemische Reaktivität besitzt.

Pulvermischungen wurden mit einer Planetenkugelmühle, einer Vibrationskugelmühle und durch Attritieren für unterschiedliche Zeiten mit  $\text{Si}_3\text{N}_4$ -Mahlmedien in Isopropanol erzeugt. Die so entstandenen Schlicker wurden mit Hilfe eines Rotations-Vakuumevaporators von den Mahlmedien abgetrennt. Vollständig getrocknete Pulver wurden nach 16 h im Trockenschrank bei  $65^\circ\text{C}$  erhalten. Sie wurden noch einmal gesiebt, um Pressgranulate mit einer maximalen Größe von  $160\ \mu\text{m}$  zu erhalten. Die Granulate wurden sodann durch kaltisostatisches Pressen mit 240 MPa zu Grünkörpern kompaktiert.

Unter den drei genannten Misch- und Mahlprozessen zum Einbringen der Sinteradditive lieferte das Attritieren die besten Resultate. Es führte zur homogenen Verteilung der Additive in einer feinkörnigen, unagglomerierten  $\text{Si}_3\text{N}_4$ -Matrix ohne chemische Verunreinigungen und zu guten Sintereigenschaften.

Im Falle des  $\text{LiYO}_2$ -Additivs beginnt die Sinterschwindung bei etwa  $1180^\circ\text{C}$  und schreitet oberhalb  $1275^\circ\text{C}$  rasch voran. Die Schwindung setzt sich während der ersten 30 min des isothermen Sinterns bei  $1500^\circ\text{C}$  fort; danach wird ein Plateau erreicht. Die gesamte lineare Schwindung liegt unmittelbar nach Erreichen der Sintertemperatur von  $1500^\circ\text{C}$  bei 11 % und steigt nach 2 h bei dieser Temperatur auf 12.5 % an. Die Sinterrate zeigt drei Maxima bei  $1275^\circ\text{C}$ ,  $1364^\circ\text{C}$  und  $1453^\circ\text{C}$ . Schmelze wird erstmals bei  $1180^\circ\text{C}$  gebildet (Punkt 1 in Abbildung 5.5); dieser Wert liegt deutlich oberhalb der eutektischen Schmelztemperaturen im  $\text{Li}_2\text{O-SiO}_2$ -System [142]. Das Ratenmaximum bei  $1275^\circ\text{C}$  lässt sich mit der Erhöhung der Menge an Schmelzphase in Zusammenhang bringen, die schließlich die Siliciumnitridkörner vollständig benetzen kann und dadurch die Umordnung zu höherer Dichte begünstigt [143]. Das XRD-Diagramm der von dieser Temperatur abgeschreckten Probe zeigt das kristalline Yttrium-Silicium-Oxynitrid  $\text{Y}_5(\text{SiO}_4)_3\text{N}$  ("N-Apatit") und Lithium-Silicium-Oxynitridphasen ( $\text{LiSiNO}$ ), was bedeutet, dass sich  $\text{Si}_3\text{N}_4$  in der Schmelze löst (Tabelle 5-I). Diese Eigenschaft ist ebenfalls Vorbedingung dafür, dass  $\text{LiYO}_2$  als sehr gutes Flussmittel und Sinteradditiv für  $\text{Si}_3\text{N}_4$  wirken kann [144].

*Tabelle 5-I: Phasenbestand der von verschiedenen Temperaturen abgeschreckten Proben mit LiYO<sub>2</sub>-Sinteradditiv.*

Temperatur (°C)	Phasenmenge (Masse-%)	Bemerkungen
1180	21 % $\beta$ -Si <sub>3</sub> N <sub>4</sub>	Schwindungsbeginn
1275	22 % $\beta$ -Si <sub>3</sub> N <sub>4</sub> LiSiNO, Y <sub>5</sub> (SiO <sub>4</sub> ) <sub>3</sub> N	1. Maximum der Sinterrate
1364	23 % $\beta$ -Si <sub>3</sub> N <sub>4</sub> Y <sub>5</sub> (SiO <sub>4</sub> ) <sub>3</sub> N	2. Maximum der Sinterrate
1453	26 % $\beta$ -Si <sub>3</sub> N <sub>4</sub> Y <sub>5</sub> (SiO <sub>4</sub> ) <sub>3</sub> N	3. Maximum der Sinterrate
1500	32 % $\beta$ -Si <sub>3</sub> N <sub>4</sub> Y <sub>5</sub> (SiO <sub>4</sub> ) <sub>3</sub> N	Nach 5 min Haltezeit
1500	65 % $\beta$ -Si <sub>3</sub> N <sub>4</sub> Y <sub>5</sub> (SiO <sub>4</sub> ) <sub>3</sub> N	Nach 2 h Haltezeit

Im Falle des LiAlSiO<sub>4</sub>-Additivs erscheint die Flüssigphase schon bei 1080°C, was eher dem niedrigsten Schmelzpunkt im Li<sub>2</sub>O-SiO<sub>2</sub>-Phasendiagramm entspricht [131]. Die Sinterrate weist drei Maxima bei 1180°C, 1275°C und 1490°C auf (Abbildung 5.10). Die XRD-Diagramme der von diesen Temperaturen abgeschreckten Proben zeigen unterschiedliche Phasenzusammensetzungen, wie in Tabelle 5-II dargestellt, und weisen damit darauf hin, dass sich die Viskosität und das Volumen der Flüssigphase während des Aufheizens signifikant ändern.

*Tabelle 5-II: Phasenbestand der von verschiedenen Temperaturen abgeschreckten Proben mit LiAlSiO<sub>4</sub>-Sinteradditiv.*

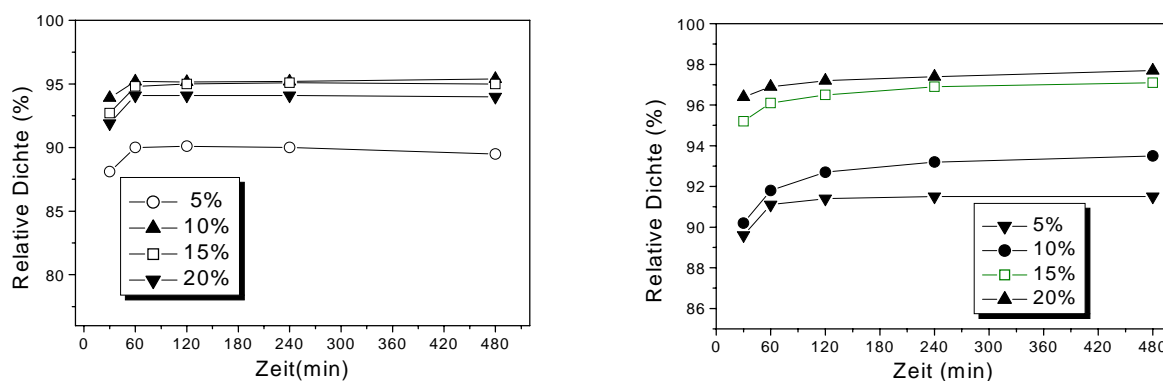
Temperatur (°C)	Phasenmenge (Masse-%)	Bemerkungen
1080	20 % $\beta$ -Si <sub>3</sub> N <sub>4</sub> $\beta$ -LiAlSiO <sub>4</sub>	Schwindungsbeginn
1180	20 % $\beta$ -Si <sub>3</sub> N <sub>4</sub> $\beta$ -LiAlSiO <sub>4</sub> , SiO <sub>2</sub>	1. Maximum der Sinterrate
1275	20 % $\beta$ -Si <sub>3</sub> N <sub>4</sub> $\beta$ -LiAlSi <sub>2</sub> O <sub>6</sub> , SiO <sub>2</sub>	2. Maximum der Sinterrate
1490	20 % $\beta$ -Si <sub>3</sub> N <sub>4</sub> $\beta$ -LiAlSi <sub>2</sub> O <sub>6</sub> , SiO <sub>2</sub>	3. Maximum der Sinterrate
1500	20 % $\beta$ -Si <sub>3</sub> N <sub>4</sub> $\beta$ -LiAlSi <sub>2</sub> O <sub>6</sub> , SiO <sub>2</sub>	Nach 5 min Haltezeit
1500	35 % $\beta$ -Si <sub>3</sub> N <sub>4</sub> SiO <sub>2</sub>	Nach 2 h Haltezeit

Das Ratenmaximum bei 1180°C entspricht einer Erhöhung der Menge an Schmelzphase. In der Phasenzusammensetzung der von dieser Temperatur abgeschreckten Probe zeigt sich eine

Verringerung der Intensität von  $\beta$ -Eucryptit ( $\text{LiAlSiO}_4$ ), die auf dem Schmelzen dieser Phase beruht. Die Anwesenheit von Coesit ( $\text{SiO}_2$ ) ist durch Kristallisation aus der Schmelze beim Abkühlen erklärlich. Im XRD-Diagramm der von  $1275^\circ\text{C}$  abgeschreckten Probe zeigt sich, dass  $\beta$ -Eucryptit verschwunden ist und durch  $\beta$ -Spodumen ( $\text{LiAlSi}_2\text{O}_6$ ) ersetzt wurde. Diese Phase besitzt das gleiche Kationenverhältnis ( $\text{Li}:\text{Al} = 1:1$ ) wie  $\beta$ -Eucryptit, weist jedoch einen höheren  $\text{SiO}_2$ -Anteil auf. Obwohl also das Additiv  $\text{LiAlSiO}_4$  vollständig aufschmilzt, erhöht sich die Gesamtmenge an Flüssigphase bei Temperaturerhöhung im Bereich bis  $1275^\circ\text{C}$  wegen der Auskristallisation der neuen Phase  $\text{LiAlSi}_2\text{O}_6$  nicht signifikant. Dies führt zu einer nur moderaten Dichteerhöhung. Das Maximum bei  $1490^\circ\text{C}$ , das mit einer Verringerung des  $\text{LiAlSi}_2\text{O}_6$ -Phasenanteils einhergeht, entspricht einer Erhöhung des Volumenanteils der Flüssigphase.

Im Gegensatz dazu bleibt jedoch das  $\alpha/\beta$ - $\text{Si}_3\text{N}_4$ -Verhältnis in der Röntgenbeugung bis  $1500^\circ\text{C}$  konstant, was bedeutet, dass während des Anfangsstadiums des Sinterns keine Phasenumwandlung von  $\alpha$ - zu  $\beta$ - $\text{Si}_3\text{N}_4$  auftritt. Die Ausbildung der Schmelze beruht also nur auf der Reaktion zwischen dem Sinteradditiv und dem an der Oberfläche der  $\text{Si}_3\text{N}_4$ -Körner vorhandenen  $\text{SiO}_2$ .

Das Verdichtungsverhalten der Materialsysteme  $\text{Si}_3\text{N}_4$ - $\text{LiYO}_2$  und  $\text{Si}_3\text{N}_4$ - $\text{LiAlSiO}_4$  als Funktion der Auslagerungsdauer bei  $1500^\circ\text{C}$  ist in den Abbildungen 5.12 und 5.13 gezeigt.



Abbildungen 5.12, 5.13: Relative Dichte bei  $1500^\circ\text{C}$  als Funktion der Auslagerungsdauer für  $\text{Si}_3\text{N}_4$  mit verschiedenen Anteilen der Sinteradditive  $\text{LiYO}_2$  (links) und  $\text{LiAlSiO}_4$  (rechts).

Das Verhältnis zwischen Sinterparametern und relativer Dichte ist für verschiedene Materialzusammensetzungen in den Tabellen 5-III ( $\text{LiYO}_2$ -Additiv) und 5-IV ( $\text{LiAlSiO}_4$ -Additiv) dargestellt. Für Sinterkörper mit wenigstens 15 Masse-% des Additivs  $\text{LiYO}_2$  werden schon nach 2 h Sinterzeit bei  $1550^\circ\text{C}$  hohe relative Dichten erreicht, die dann bei weiterer Verlängerung der Sinterzeit im wesentlichen konstant bleiben. Bei gleichzeitiger

Erhöhung der Sintertemperatur und der Sinterzeit gehen die Dichtewerte dagegen deutlich zurück. Die reduzierte Sinterdichte bei Erhöhung der Sintertemperatur kann den hohen Dampfdrücken vor allem des Lithiumoxids und des Siliciumdioxids zugeschrieben werden.

*Tabelle 5-III: Sinterdichten mit unterschiedlichen Mengen an LiYO<sub>2</sub>-Additiv.*

Additivgehalt (Masse-%)	1550°C			1600°C			1650°C		
	2 h	4 h	8 h	2 h	4 h	8 h	2 h	4 h	8 h
5	88.7	88.95	88.1	88.5	88.2	87.8	88.1	80.0	79.6
10	94.9	95.1	95.0	95.2	94.9	94.2	93.7	93.1	92.4
15	98.3	98.3	98.3	98.3	98.1	97.2	98.3	97.8	97.5
20	98.3	98.2	98.3	98.3	97.8	97.8	98.2	97.6	97.5

Im Falle des LiAlSiO<sub>4</sub>-Additivs weisen die mit niedrigerem Additivgehalt gesinterten Materialien höhere relative Dichten als die Proben mit höherem Additivgehalt auf (Tabelle 5-IV). Die höchsten Dichten werden für Sinterkörper mit 10 Masse-% Additiv erhalten. Die Dichtewerte dieser Proben bleiben bei Verlängerung der Auslagerungszeiten bei allen Sintertemperaturen nahezu konstant.

*Tabelle 5-IV: Sinterdichten mit unterschiedlichen Mengen an LiAlSiO<sub>4</sub>-Additiv.*

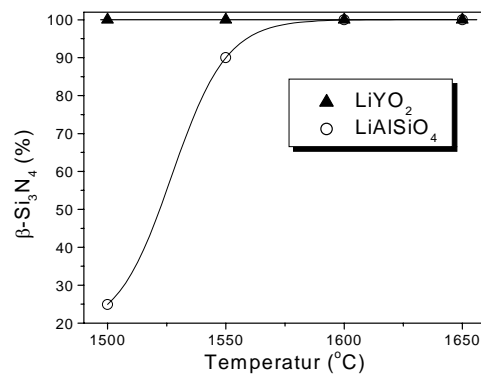
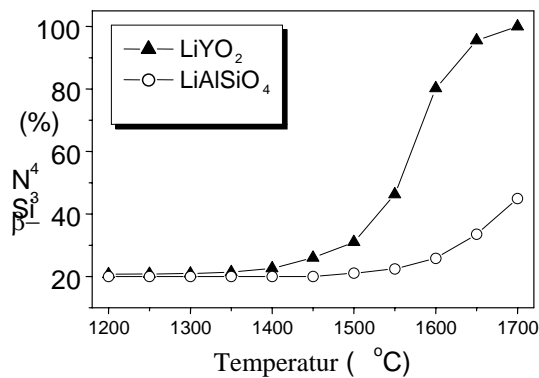
Additivgehalt (Masse-%)	1550°C			1600°C			1650°C		
	2 h	4 h	8 h	2 h	4 h	8 h	2 h	4 h	8 h
5	90.1	89.7	89.4	89.5	89.2	89.0	89.1	88.8	87.9
10	98.3	98.3	98.3	98.3	98.1	98.1	98.1	97.7	97.5
15	98.3	98.3	98.1	98.3	97.9	97.2	97.4	97.2	96.8
20	93.6	92.7	92.4	93.0	92.3	92.0	92.3	91.5	91.2

Das Verdichtungsverhalten wird in beiden Additivsystemen durch Teilchenumordnung und durch Lösungs-Diffusions-Wiederausscheidungsprozesse bestimmt. Teilchenumordnung trägt wesentlich zur Verdichtung bei niedrigeren Temperaturen bei, und Lösung-Diffusion-Wiederausscheidung ist der vorherrschende Mechanismus bei höheren Temperaturen. Beim LiYO<sub>2</sub>-System hängt die Verdichtung stark vom Additivgehalt ab. Ein höherer Gehalt an Sinteradditiv bedeutet einen höheren Volumenanteil an Flüssigphase, was wiederum

Teilchenumlagerungsvorgänge erleichtert. Im Falle der  $\text{LiAlSiO}_4$ -Additive findet man, dass die Enddichte weniger stark vom Additivgehalt abhängt.

Beim  $\text{LiYO}_2$ -Additiv beginnt die Phasenumwandlung von  $\alpha$ - zu  $\beta$ - $\text{Si}_3\text{N}_4$  schon bei  $1300^\circ\text{C}$ , obwohl ihr Umfang unter diesen Bedingungen noch gering bleibt. Für Sinterkörper mit 15 Masse-% Additiv beschleunigt sich die Umwandlung bei  $1500^\circ\text{C}$  und ist nach 5 min Auslagerungszeit bei  $1700^\circ\text{C}$  abgeschlossen (Abbildung 6.2).

Im Falle der  $\text{LiAlSiO}_4$ -Additive wird die Verdichtung hingegen bis  $1500^\circ\text{C}$  nicht von einer Phasenumwandlung begleitet. Darüber setzt sie mit steigender Temperatur sehr zögerlich ein (Abbildung 6.2). Die kristalline Phase  $\beta$ -Spodumen ( $\text{LiAlSi}_2\text{O}_6$ ) bleibt bei Temperaturen unterhalb  $1500^\circ\text{C}$  stabil. In diesem Stadium ist der Gehalt an Schmelze im System beschränkt.  $\text{LiAlSi}_2\text{O}_6$  beginnt jedoch bei Temperaturen oberhalb  $1500^\circ\text{C}$ , sich in der Schmelze aufzulösen. Der maximale  $\alpha$ -zu- $\beta$ -Umwandlungsgrad für Sinterkörper mit 15 Masse-% Additiv beträgt 45 % nach 5 min bei  $1700^\circ\text{C}$ . Mit Verlängerung der Auslagerungszeiten erhöht sich der Umwandlungsgrad dann jedoch zügig, so dass auch mit dem Additiv  $\text{LiAlSiO}_4$  100 %  $\beta$ - $\text{Si}_3\text{N}_4$  erreicht werden (Abbildung 6.3). Die verzögerte Phasenumwandlung beim Additiv  $\text{LiAlSiO}_4$  spricht dafür, dass die Umwandlung sehr empfindlich auf die Viskosität der Schmelze reagiert.



Abbildungen 6.2, 6.3: Die Umwandlung von  $\alpha$ - zu  $\beta$ - $\text{Si}_3\text{N}_4$  als Funktion der Temperatur bei Sinterzeiten von 5 min (links) und 1 h (rechts). Die Additivmenge beträgt jeweils 15 Masse-%

Im Falle des Additivs  $\text{LiYO}_2$  steigt die Umwandlungsrate mit steigender Additivmenge an, während bei  $\text{LiAlSiO}_4$  ein gegenläufiges Verhalten zu beobachten ist, d. h. die Umwandlungsrate wird mit zunehmendem Additivgehalt kleiner. Es ist bekannt, dass  $\text{Y}_2\text{O}_3$ -Zuschläge zum  $\text{SiO}_2$ -Sinteradditiv sowohl die Phasenumwandlung als auch die Verdichtung von  $\text{Si}_3\text{N}_4$ -Keramiken beschleunigen [152]. In diesem Fall generiert die Erhöhung des Gesamt-Additivgehaltes ein größeres Volumen an Flüssigphase und verringert zusätzlich

deren Viskosität, und als Ergebnis werden eine schnellere Umwandlungskinetik und höhere Dichten erhalten. Beim Additiv  $\text{LiAlSiO}_4$  ist es hingegen so, dass bei Erhöhung des Flüssigphasenanteils die Zeitspanne bis zum Erreichen der zur  $\beta\text{-Si}_3\text{N}_4$ -Ausscheidung notwendigen Übersättigung der Schmelze ansteigt.

Die vorliegende Untersuchung zeigt, dass Phasenumwandlungs- und Verdichtungskinetik nicht direkt miteinander gekoppelt sind. Dies ist in Abbildung 6.4 dargestellt, in der der Verlauf der Verdichtung und der  $\alpha$ -zu- $\beta$ -Umwandlung einander als Funktion der Sintertemperatur gegenüber gestellt sind.

In beiden Fällen eilt die Verdichtung der Phasenumwandlung deutlich voraus, so dass letztere erst in einem späten Sinterstadium stattfindet. Bei  $1400^\circ\text{C}$  wird so gut wie keine Phasenumwandlung beobachtet, während für  $\text{LiYO}_2$ - bzw.  $\text{LiAlSiO}_4$ -Additive schon mehr als 90 % bzw. 80 % der theoretischen Dichte erreicht sind. Bei höheren Temperaturen verringert sich der Abstand zwischen den beiden Phänomenen im Falle des Additvs  $\text{LiYO}_2$  deutlich, während die Verzögerung im Falle des Additvs  $\text{LiAlSiO}_4$  weiterhin bestehen bleibt.

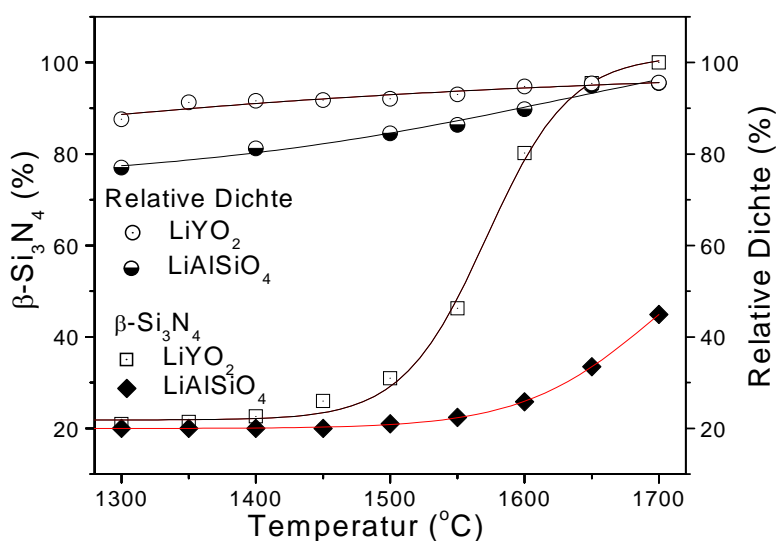
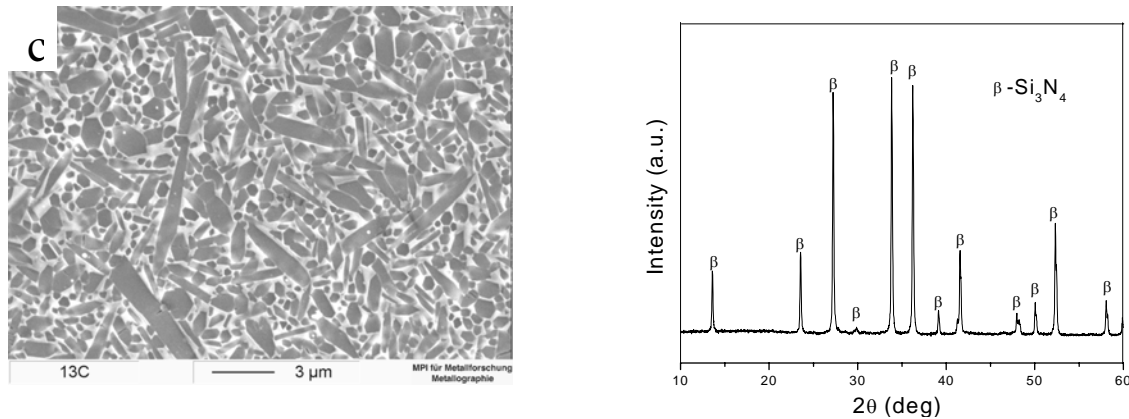


Abbildung 6.4: Verdichtung und Phasenumwandlung als Funktion der Sintertemperatur für  $\text{LiYO}_2\text{-Si}_3\text{N}_4$ - und  $\text{LiAlSiO}_4\text{-Si}_3\text{N}_4$ -Materialien

Die Gefüge der  $\text{Si}_3\text{N}_4$ -Materialien, die mit 15 Masse-% Additivgehalt für 8 h bei  $1600^\circ\text{C}$  gesintert wurden, sind durch eine homogene Verteilung gestreckter  $\text{Si}_3\text{N}_4$ -Körner mit an den Korngrenzen und Tripelpunkten eingelagerter Glasphase gekennzeichnet (Abbildung 7.0). Bei dieser Sintertemperatur findet Kornwachstum statt, was zu der beobachteten Mikrostruktur mit elongierten  $\beta\text{-Si}_3\text{N}_4$ -Körnern führt. Dass nahezu alle Kontaktstellen zwischen den  $\text{Si}_3\text{N}_4$ -Körnern mit Glasphase belegt sind, weist auf ein gutes Benetzungsverhalten hin.

In beiden Additivsystemen weisen die Röntgenbeugungsbilder der für 8 h bei 1600°C gesinterten Proben ausschließlich die Reflexe von  $\beta$ - $\text{Si}_3\text{N}_4$  auf, es sind also keine kristallinen Zweitphasen vorhanden (Abbildung 7.5). Dies zeigt an, dass die nach Abdampfen des  $\text{Li}_2\text{O}$  verbleibende Sekundärphase vollständig als Glasphase erstarrt und dass eine vollständige Umwandlung von  $\alpha$ - zu  $\beta$ - $\text{Si}_3\text{N}_4$  stattgefunden hat.



Abbildungen 7.0 und 7.5: Typische REM-Gefügeaufnahme (links, polierter und plasmageätzter Anschliff) und XRD-Diagramm (rechts) eines Materials mit 15 Masse-% Additivanteil nach dem Sintern für 8 h bei 1600°C.

Die experimentellen Ergebnisse dieser Arbeit lassen sich wie folgt zusammenfassen:

1. Es werden drei Verfahren des mechanischen Mischens (Mahlen mittels Attritormühle, Kugelmühle und Schwingmühle) zum Einbringen des  $\text{LiYO}_2$ -Additivs in das  $\text{Si}_3\text{N}_4$ -Pulver untersucht. Die besten Ergebnisse werden mit der Attritormühle erzielt. Man erhält hierbei ein feinkörniges, nichtagglomeriertes  $\text{Si}_3\text{N}_4$ -Pulver, in dem das Additiv gut dispergiert vorliegt und keine mahlbedingten Verunreinigungen auftreten. Das auf diese Weise hergestellte Pulver zeigt eine gute Sintercharakteristik.
2. Im Fall des  $\text{Si}_3\text{N}_4$ - $\text{LiYO}_2$ -Materialsystems hängt die Verdichtung hauptsächlich von der zugesetzten Menge an Sinteradditiv ab. Eine größerer Additivanteil bedeutet einen größeren Volumenanteil an flüssiger Phase, wodurch eine effizientere Teilchenumlagerung stattfindet, die zu höheren Sinterdichten führt. Im Fall des  $\text{Si}_3\text{N}_4$ - $\text{LiAlSiO}_4$ -Systems ist die Verdichtung weniger vom Additivgehalt abhängig. Bis zu einer Temperatur von 1500°C beobachtet man während der Verdichtung keine  $\alpha \rightarrow \beta$ -Transformation der  $\text{Si}_3\text{N}_4$ -Phase. Demnach wird hier der Endwert der Sinterdichte

ohne Vermittlung eines durch Entmischung, Diffusion und Phasenumlösung gekennzeichneten Mechanismus erzielt.

3. Die Kinetik des Sinterprozesses bei niedrigen Glühtemperaturen zeigt bei Verwendung von  $\text{LiYO}_2$  als Additive eine geringere zeitliche Verzögerung bei  $\text{LiAlSiO}_4$ . Der Einsatz von  $\text{LiYO}_2$  liefert höhere Dichten bei niedrigeren Glühtemperaturen und ermöglicht kürzere Sinterzeiten. Mit verlängerter Glühdauer werden die Unterschiede im Verdichtungsgrad geringer.
4. Die  $\alpha \rightarrow \beta$  Transformation des  $\text{Si}_3\text{N}_4$  läßt sich in beiden untersuchten Systemen als Umwandlung erster Ordnung klassifizieren.
5. Im  $\text{Si}_3\text{N}_4$ - $\text{LiYO}_2$ -Materialsystem erhöht sich die  $\alpha$ - $\beta$ -Umwandlungsrate mit steigendem Additivgehalt, während für das  $\text{Si}_3\text{N}_4$ - $\text{LiAlSiO}_4$ -System das entgegengesetzte Verhalten beobachtet wird.
6. Die  $\alpha \rightarrow \beta$  Umwandlung des  $\text{Si}_3\text{N}_4$  ist bei allen Proben erst am Ende der Verdichtung vollständig. Der zeitliche Verzug zwischen beiden Stadien des Sinterprozesses ist aufgrund der höheren Viskosität der flüssigen Phase im System  $\text{Si}_3\text{N}_4$ - $\text{LiAlSiO}_4$  stärker ausgeprägt.
7. Die  $\alpha \rightarrow \beta$ -Transformation der  $\text{Si}_3\text{N}_4$ -Phase geht mit Kornwachstum einher. Bei Variation der Glühdauer ändern sich sowohl die Korngröße als auch die Morphologie der entstehenden  $\beta$ - $\text{Si}_3\text{N}_4$ -Teilchen, wobei die anfangs ebenmäßig geformten Körner merklich elongieren. Das Kornwachstum verläuft anisotrop und führt zu stäbchenförmigen  $\text{Si}_3\text{N}_4$ -Kristallen. Die Kornwachstumsrate ist im  $\text{Si}_3\text{N}_4$ - $\text{LiYO}_2$ -Materialsystem höher als im  $\text{Si}_3\text{N}_4$ - $\text{LiAlSiO}_4$ -System.
8. Die Mikrostruktur der bei  $1600^\circ\text{C}$  gesinterten  $\text{Si}_3\text{N}_4$ -Keramiken ist für beide Additive charakterisiert durch eine homogene Verteilung elongierter  $\beta$ - $\text{Si}_3\text{N}_4$ -Körner sowie die Anwesenheit einer Glasphase, die in dünnen Schichten an Korngrenzen und in den Tripelpunkten auftritt.



9. Die Maximalwerte der Bruchzähigkeit der mit  $\text{LiYO}_2$  und  $\text{LiAlSiO}_4$  gesinterten  $\text{Si}_3\text{N}_4$ -Proben (8h bei  $1600^\circ\text{C}$ ) betragen 6.8 bzw. 6.2. Der höhere Wert beim  $\text{Si}_3\text{N}_4$ - $\text{LiYO}_2$ -System korrespondiert mit einem höheren Aspektverhältnis elongierter  $\beta$ - $\text{Si}_3\text{N}_4$ -Körner in der Mikrostruktur.
  
10. Die Wärmeleitfähigkeit der gesinterten  $\text{Si}_3\text{N}_4$ -Proben ist bei Verwendung von  $\text{LiYO}_2$  als Sinterzusatz höher als für  $\text{LiAlSiO}_4$ . Bei letzterem führt teilweise in den  $\beta$ - $\text{Si}_3\text{N}_4$ -Körnern gelöstes Al zu einer höheren Anzahl streuender Phononen und folglich zu einer geringeren Wärmeleitfähigkeit.

**REFERENCES**

- [1] J. F. Collins and R. W. Gerby, *Metals*, **7** (1955) 612.
- [2] G. Petzow and M. Herrmann, *Structure and Bonding*, **Vol. 102** (2002) p. 51., Springer-Verlag, Berlin.
- [3] G. Deeley, J. Herbert, *Powder Metall.*, **8** (1961) 145.
- [4] M. Mitomo and Y. Tayima, *J. Jpn. Ceram. Soc.*, **99** (1991) 1014.
- [5] G. R. Terwilliger, *J Am. Ceram. Soc.*, **57** (1974) 48.
- [6] M. Mitomo, *J. Mater. Sci.*, **11** (1976) 1103.
- [7] Y. Ojama and O. Kamigaito, *Jpn. J. Appl. Phys.*, **10** (1971) 1637.
- [8] K. H. Jack and W. J. Wilson, *Nature (Phys. Sci)*, **238** (1972) 28.
- [9] K. H. Jack, *J. Mater. Sci.*, **11** (1976) 1135.
- [10] F. Riley, *J. Am. Ceram. Soc.*, **83** [2] 245-65 (2000).
- [11] G. Ziegler, J. Heinrich, G. Wötting, *J. Mater. Sci.*, **22**, 3041-86 (1987).
- [12] D. Suttor, G. S. Fischman, *J. Am. Ceram. Soc.*, **75** (5) 1063-67 (1992).
- [13] L. M. Sheppard, *Ceram. Bull.*, **70** (1991) 692.
- [14] M. Herrmann, J. Schulz and J. Hintermayer, 4<sup>th</sup> Euro-Ceramics **Vol. 2** (1995) 211.
- [15] S. Kim, T. Sonders, *J. Am. Ceram. Soc.*, **74** (1991) 1833.
- [16] A. Zerr, G. Miehe, G. Serghiou, M. Schwarc, E. Kroke, R. Riedel, H. Fuess, P. Kroll and R. Boehler, *Nature*, **440** (1999) 340.
- [17] C. Kirk, *J. Appl. Phys.*, **50** (1979) 4190.
- [18] P. Morgan, in *Nitrogen Ceramics*, ed. F. Riley, Noordhoff, Leyden (1977) p. 23.
- [19] D. Thompson and P. Pratt, *Mat. Sci. Forum*, **47** (1989) 21.
- [20] W. Dressler and R. Riedel, *Int. J. Refractory Metals and Hard Materials*, **15** (1997) 13.
- [21] S. Wild, P. Grievson and K. Jack, 'Special Ceramics' **Vol. 5** (1972) p. 385.
- [22] H. Priest, F. Burns, G. Priest and E. Skaar, *J. Am. Ceram. Soc.*, **7** (1973) 395.
- [23] K. Kato, Z. Inoue, K. Kijima, I. Kawada, H. Tanaka and T. Yamane, *J. Am. Ceram. Soc.*, **58** (1975) 90.
- [24] T. Zoltai, *Am. Mineral.*, **45** (1960) 960.
- [25] C. Wang, X. Pan, M. Rühle, F. Riley and M. Mitomo, *J. Mater. Sci.*, **31** (1996) 5281.
- [26] D. Hardie and K. Jack, *Nature*, **180** (1957) 332.
- [27] R. Green, *Acta Crystallogr.*, **B35** (1979) 800.

- 
- [28] S. Hampshire and K. Jack, in *Progress in Nitrogen Ceramics*, ed. F. L. Riley, Martinus Nijhoff, Boston (1983) p. 225.
- [29] J. Jiang, K. Stahl, R. Berg, D. Frost, T. Zhou and P. Shi, *Europhys. Lett.*, **51** (2000) 62.
- [30] J. Jiang, K. Kragh, D. Frost, K. Stahl and H. Lindelov, *J. Phys. Condens. Matter*, **13** (2001) L515-L520.
- [31] R. Marchand, Y. Laurent, J. Guyader, P. L'Haridon and P. Verdier, *J. Eur. Ceram. Soc.*, **8** (1991) 197.
- [32] L. Gauckler, H. Lukas and G. Petzow, *J. Am. Ceram. Soc.*, **58** (1975) 346.
- [33] T. Ekström and M. Nygren, *J. Am. Ceram. Soc.*, **75** (1992) 259.
- [34] M. Herrmann, H. Klemm and C. Schubert, in *Silicon Nitride Based Hard Materials, Handbook of Ceramic Hard Materials, Vol. 2.*, ed. Ralf Riedel, Darmstadt, Wiley-VCH, Weinheim (2000) p. 749.
- [35] V. Izhevskiy, L. Genova, J. Bressiani and F. Aldinger, *J. Eur. Ceram. Soc.*, **20** (2000) 2275.
- [36] K. Jack, *Nature*, **274** (1978) 880.
- [37] K. Jack, *Prospects for nitrogen ceramics, Key Engng. Mat.*, **Vol. 89-91** (1994) 345.
- [38] H. Mandal, D. Thompson and T. Ekström, *J. Eur. Ceram. Soc.*, **12** (1993) 421.
- [39] M. R. Lee, S. S. Russel, J. W. Arden, C. T. Pillinger, *Meteoritics*, **30** (1995) 387.
- [40] W. Rhodes and S. Natansonh, *Ceram. Bull.*, **68** (1989) 1804.
- [41] D. Segal, *Br. Ceram. Transaction*, **85** (1986) 184.
- [42] F. Riley, *Mat. Sci. Forum*, **47** (1989) 70.
- [43] A. Merzhanov, *Ceram. Int.*, **21** (1995) 371.
- [44] M. Herrmann, I. Schulz, W. Hermel, Chr. Schubert and A. Wendt, *Z. Metallkd.*, **92** (2001) 788.
- [45] M. Ekelund and B. Forslund, *J. Am. Ceram. Soc.*, **75** (1992) 532.
- [46] T. Arakova, K. Ohno and K. Ueda, *Ceramics*, **22** (1987) 34.
- [47] Z. Pan, H. Li and H. Zhang, *J. Mater. Res.*, **13** (1998) 1996.
- [48] Z. Dohcevic, B. Matovic, S. Boskovic and Z. Popovic, *Philosophical Magazine A*, **82** (2002) 93.
- [49] G. Ziegler, *Z. Werkstofftech.* **14** (1983) 189.
- [50] A. H. Heuer and V. L. Lou, *J. Am. Ceram. Soc.*, **73** (1990) 2785.
- [51] H. M. Jennings, *J. Mater. Sci.*, **18** (1983) 951.
- [52] C. Greskovich, J. Rosolovski, *J. Am. Ceram. Soc.*, **59** (1976) 336.

- 
- [53] V. K. Lou, T. E. Mitchell and A. H. Heuer, *J. Am. Ceram. Soc.*, **68** (1985) 49.
- [54] W. D. Kingery, *Solid State Phenomena*, **25-26** (1992) 1.
- [55] A. W. Adamson and A. P. Gast, *Physical Chemistry of Surfaces*, Wiley-Interscience, New York (1997) p. 6.
- [56] W. D. Kingery, *Introduction to Ceramics*, John Wiley, New York (1960) p. 386.
- [57] M. W. Barsoum, *Fundamentals of Ceramics*, McGraw-Hill, Singapore (1997) p. 334.
- [58] W. D. Kingery, *J. Appl. Phys.*, **30** (1959) 301.
- [59] W. D. Kingery and M. D. Norasimhan, *J. Appl. Phys.*, **30** (1959) 307.
- [60] G. Petzow and W. J. Huppmann, *Z. Metallkde.*, **67** (1976) 579.
- [61] R. M. German, *Liquid Phase Sintering*, Plenum, New York (1985) p. 5.
- [62] J. Weiss and W. Kaysser, 'Liquid phase sintering', in *Progress in Nitrogen Ceramics*, ed. F. L. Riley, Martinus Nijhoff Publishers, Boston (1983) p. 169.
- [63] W. A. Kaysser and G. Petzow, *Z. Metallkde.*, **76** (1985) 687.
- [64] S. Kang, W. A. Kaysser, G. Petzow and D. N. Yoon, *Powder Metall.*, **27** (1984) 97.
- [65] S. Sarian and H. W. Weart, *J. Appl. Phys.*, **37** (1966) 1675.
- [66] J. Svoboda, H. Riedel and R. Gaebel, *Acta Mater.* **44** (1996) 3215.
- [67] S. Lee and S. L. Kang, *Z. Metallkde.*, **92** (2001) 669.
- [68] J. K. Park, S. J. Kang, K. Y. Eun and D. N. Yoon, *Metall. Trans.*, **20** (1989) 837.
- [69] S. J. Kang and P. Azou, *Powder Metall.*, **28** (1985) 90.
- [70] J. K. Park, S. J. Cho, and D. N. Yoon, *Metall. Trans.*, **15** (1984) 1075.
- [71] J. K. Park, H. H. Kwon, and D. N. Yoon, *Metall. Trans.*, **17** (1986) 1915.
- [72] O. J. Kwon and D. N. Yoon, *Int. J. Powder Metall.*, **17** (1981) 127.
- [73] G. Petzow and W. A. Kaysser, *Basic Mechanisms of liquid Phase Sintering*, in *Sintered Metal-Ceramic Composites*, ed. G. S. Upadhyaya, Elsevier Science Publishers, Amsterdam, (1984) p. 595.
- [74] G. Petzow and H. E. Exner, *Z. Metallkde.*, **67** (1976) 611.
- [75] N. J. Shaw, *Powd. Metall. Int.*, **21** (1983) 25.
- [76] M. N. Rahaman, *Ceramic Processing and sintering*, Dekker, New York, (1995) p. 524.
- [77] P. Drew and M. H. Lewis, *J. Mater. Sci.*, **9** (1974) 1833.
- [78] K. Kijima and S. Shirasaki, *J. Chem. Phys.*, **65** (1976) 2668.
- [79] G. Brebec, R. Sella, J. Bevenot and J. C. Martin, *Acta Metall.*, **28** (1980) 327.
- [80] D. R. Messier, F. L. Riley and R. J. Brook, *J. Mater. Sci.*, **13** (1978) 1199.
- [81] P. Drew and M. H. Lewis, *J. Mater. Sci.*, **9** (1974) 261.
- [82] M. Krämer, M. J. Hoffmann and G. Petzow, *Acta Metall. Mater.*, **41** (1993) 2939.

- [83] Y. Okamoto, N. Hirosaki, Y. Akimune and M. Mitomo, *J. Ceram. Soc. Jpn.*, **105** (1997) 476.
- [84] N. J. Shaw, *Powder Metall. Int.*, **21** (1989) 16.
- [85] D. D. Lee, S. L. Kang and D. N. Yoon, *J. Am. Ceram. Soc.*, **71** (1988) 803.
- [86] M. A. Einarsrud and M. Mitomo, *J. Am. Ceram. Soc.*, **76** (1993) 1624.
- [87] H. J. Kleebe, *J. Ceram. Soc. Jpn.*, **105** (1997) 453.
- [88] J. Rödel, *J. Eur. Ceram. Soc.*, **10** (1992) 143.
- [89] K. T. Faber and A. G. Evans, *Acta Metall.*, **31** (1983) 565.
- [90] T. M. Shaw, O. L. Krivanek and G. Thomas, *J. Am. Ceram. Soc.*, **62** (1979) 305.
- [91] I. C. Huseby and G. Petzow, *Powder Metall. Int.*, **6** (1974) 17.
- [92] S. Hausner, *Sci. Ceram.*, **12** (1983) 229.
- [93] K. H. Jack, in *Nitrogen Ceramics*, ed. F. L. Riley, Martinus-Nijhoff, (1983) p. 109.
- [94] J. Briggs, *Mater. Res. Bull.*, **12** (1997) p. 1047.
- [95] S. Hampshire, R. A. Drew and K. H. Jack, *Phys. Chem. Glasses*, **26** (1985) 182.
- [96] N. Hirosaki, A. Okada and K. Matoba, *J. Am. Ceram. Soc.*, **71** (1988) C-144.
- [97] O. Abe, *Ceram. Int.*, **16** (1990) 53.
- [98] O. Fabrichnaya, H. J. Seifert, R. Weiland, T. Ludwig, F. Aldinger and A. Navrotsky, *Z. Metallkd.* **92** (2001) 9.
- [99] J. C. Bressiani, V. Izhevskiy, A. H. Bressiani, *Mater. Res.*, **2** (1999) 165.
- [100] S. Bandyopadhyay, in *Sintered metallic and ceramic materials*, John Wiley, Chichester (2000) p. 556.
- [101] M. Herrmann, G. Putzky, S. Siegel and W. Hermel, *cfi. Ber. DKG*, **69** (1992) 375.
- [102] H. Björklund, L. K. Falk, K. Rundgren and J. Wasen, *J. Eur. Ceram. Soc.*, **17** (1997) 1285.
- [103] M. Herrmann and O. Goeb, *J. Eur. Ceram. Soc.*, **21** (2001) 304.
- [104] K. Yokoyama and S. Wada, *J. Ceram. Soc. Jpn.*, **108** (2000) 230.
- [105] M. M. Schwartz, 'Handbook of structural ceramics', McGraw-Hill. (1992) p. 21
- [106] K. Komeya, in *Fine Ceramics*, ed. S. Saito, Elsevier Science Publishing Co. New York (1988) p. 175.
- [107] P.F. Becher, C. H. Hsueh, P. Angelini and T. N. Tieges, *J. Am. Ceram. Soc.*, **71** (1988) 1050.
- [108] H. Mandel and M. J. Hoffmann, in *Nitrides and Oxynitrides*, ed. S. Hampshire, Trans. Tech. Publications Ltd., Zelene, (2000) p. 219.
- [109] P. Sajgalik, J. Dusza and M. Hoffmann, *J. Am. Ceram. Soc.*, **78** (1995) 2619.

- 
- [110] I. Peterson and T. Tien, *J. Am. Ceram. Soc.*, **78** (1995) 2345.
- [111] I. Tanaka, G. Pezzotti, K. Okamoto, Y. Miyamoto and M. Koizumi, *J. Am. Ceram. Soc.*, **74** (1992) 755.
- [112] G. D. Quinn, *J. Mater. Sci.*, **25** (1990) 4361.
- [113] W. E. Luecke, S. M. Wiederhorn, *J. Am. Ceram. Soc.*, **82** (1999) 2769.
- [114] K. Hirao, K. Watari, H. Hayashi and M. Kitayama, *MRS Bulletin* **6** (2001) 451.
- [115] S. Haggerty and A. Lightfoot, *Ceram. Eng. Sci. Proc.*, **16** (1995) 475.
- [116] K. Watari, *J. Ceram. Sci. Jpn.*, **109** (2001) 57.
- [117] T. Hirai, S. Hayashi and K. Niihara, *Am. Ceram. Soc. Bull.*, **57** (1978) 1126.
- [118] K. Tsukama, M. Shimada and M. Koizumi, *Am. Ceram. Soc. Bull.*, **60** (1981) 910.
- [119] K. Watari, L. Pottier, B. Li, D. Fournier and M. Torijama, in *Grain Boundary Engineering in Ceramics*, ed. T. Sakuma, L. Sheppard and Y. Ikuhara, Westerville, (2000) p. 341.
- [120] K. Watari, K. Hirao, M. Toriyama and K. Ishizaki, *J. Am. Ceram. Soc.*, **82**. (1999) 777.
- [121] M. Kitayama, K. Hirao, M. Toriyama and S. Kanzaki, *J. Am. Ceram. Soc.*, **82**. (1999) 3105.
- [122] S. C. Singhal, *J. Mater. Sci.*, **11** (1976) 500.
- [123] D. Cubicotti and K. H. Lau, *J. Am. Ceram. Soc.*, **61** (1978) 512.
- [124] C. N. Babini, A. Bellosi and P. Vincenzini, *J. Mater. Sci.*, **19** (1984) 1029.
- [125] A. Bouarroud, P. Goursat and J. L. Besson, *J. Mater. Sci.*, **20** (1985) 1150.
- [126] M. Mieskowski and W. A. Sanders, *J. Am. Ceram. Soc.*, **68** (1985) C1-60.
- [127] P. Andrews and F. L. Riley, *J. Eur. Ceram. Soc.*, **5** (1989) 245.
- [128] S. K. Biswas, J. Mukerji and P. K. Das, *Key Engng. Mater.*, **89-91** (1994) 271.
- [129] J. Schlichting, L. J. Gauckler, *Powder Metall. Int.* **9** (1977) 36.
- [130] G. Petzow and J. Weiss, *Bulletin de la societe chimique Beograd*, **46** (1981) 123.
- [131] L. J. Bowen, T. G. Carruthers and R. J. Brook, *J. Am. Ceram. Soc.*, **61** (1978) 335.
- [132] I. Tanaka, K. Niihara, S. Nasu and H. Adachi, *J. Am. Ceram. Soc.*, **76** (1993) 2833.
- [133] D. J. Kim, P. Greil and G. Petzow, *Advanced Ceram. Mat.*, **2** (1987) 817.
- [134] C.P. Gazzara, D.R. Messier, *J. Am. Ceram. Soc.* **78** (1977) 1076.
- [135] G. R. P. Anstis, P. Chantikul, B. R. Lawn and D. B. Marshall, *J. Am. Ceram. Soc.*, **64** (1981) 533.
- [136] M. Kitiyama, K. Hirao, A. Tsuge, K. Watari, M. Toriyama and S. Kauzaki, *J. Am. Ceram. Soc.*, **83** (2000) 1985.
- [137] D.C. Park, T. Yano, *J. Am. Ceram. Soc.*, **83** 296 (2000).

- 
- [138] A. Leriche, D. Libert, V. Vandeneede, F. Cambier, *Mater. Sci. Forum*, **47** 119 (1989).
- [139] G. Kaiser, H. Schubert, *J. Eur. Ceram. Soc.*, **11** 253 (1993).
- [140] I. A. Bondar and L. N. Korolova, *Russ. J. Inorg. Chem. (Engl. Transl.)*, **23** (1978) 900.
- [141] R. A. Eppler, *J. Am. Ceram. Soc.*, **46** (1963) 100.
- [142] S. Kim and T. H. Sanders, *J. Am. Ceram. Soc.*, **74** (1991) 1833.
- [143] W. Kaysser, M. Zivkovic and G. Petzow, *J. Mater. Sci.*, **20** (1985) 578.
- [144] B. Matovic, G. Rixecker and F. Aldinger, *J. Mater. Sci. Lett.*, **22** (2003) 91.
- [145] S. Wada, *J. Ceram. Soc. Jpn.*, **109** (2001) 803.
- [146] M. J. Hoffman, *MRS Bull.* **2** (1995) 28.
- [147] Y. Zou, A. Petric, *J. Phys. Chem. Solids*, **55** (1994) 493.
- [148] K. Jokoyama and S. Wada, *J. Ceram. Soc. Jpn.*, **108** (2000) 6.
- [149] M. Hillert, S. Jonsson and B. Sundman, **83** (1992) 648.
- [150] P. Rocabois, C. Chatillon and C. Bernard, *J. Am. Ceram. Soc.*, **79** (1996) 1351.
- [151] S. Hampshire and K. H. Jack, *Brit. Ceram. Soc. Proc.*, **6** (1975) 37.
- [152] S. Ordonez, I. Iturriza and F. Castro, *J. Mater. Sci.*, **34** (1999) 147.
- [153] J. Yang, Z. Deng, T. Ohji and K. Niihara, in *Grain Boundary Engineering in Ceramics*, ed. T. Sakuma, L. Sheppard and Y. Ikuhara, Clerance Center, Danvers (2000) p. 137.
- [154] H. Emoto, H. Hirotsuru and M. Mitomo, *Key Eng. Materials*, **159-160** (1999) 215.
- [155] [145] M. Kitayama, K. Hirao, M. Toriyama and S. Kanzaki, *J. Ceram. Soc. Jpn.*, **107** (1999) 10.
- [156] J. F. Yang, G. J. Zhang, T. Ohji and K. Nihira, *J. Ceram. Soc. Jpn.*, **108** (2000) 697.
- [157] M. Mitomo and K. Mizumo, *J. Ceram. Soc. Jpn.*, **94** (1986) 96.
- [158] H. Yang, G. Yang and R. Yuan, *Material Chem. Phys.*, **55** (1998) 164.
- [159].M. J. Hoffmann and G. Petzow, in *Silicon Nitride Ceramics: Scientific and Technological Advances*, ed. I. W. Chen, P. F. Becher, M. Mitomo, G. Pezow and T. S. Yen, *Mater. Res. Soc. Symp. Proc. Pittsburgh*, (1993) p. 3.
- [160]. M. Mitomo, in *Advanced Ceramics-2*, ed. S. Sömiya (Elsevier Applied Science, London, 1986) p. 147.
- [161].H. J. Kleebe, G. Pezzotti and G. Ziegler, *J. Am. Ceram. Soc.*, **82** (1999) 1857.
- [162]. J. L. Iskoa and F. F. Lange, in *Ceramic Microstructures*, ed. R. M. Fuhalti and J. A. Pask, Westview Press, Boulder (1977) p. 381.
- [163]. M. Krämer, M. J. Hoffmann and G. Petzow, *Acta Metall. Mater.*, **41** ((1993) 2939.

- [164]. M. Krämer, M. J. Hoffmann and G. Petzow, *J. Am. Ceram. Soc.*, **76** (1993) 2778.
- [165]. H. J. Kleebe, *J. Ceram. Soc. Jpn.*, **105** (1993) 453.
- [166] A. J. Pyzik and D. R. Beaman, *J. Am. Ceram. Soc.*, 76 (1993) 2737.
- [167] P. Sajgalik, J. Dusza and M. J. Hoffmann, *J. Am. Ceram. Soc.*, 78 (1995) 2619.
- [168] M. Kitayamy, *J. Am. Ceram. Soc.*, 83 (2000) 1985.
- [169] F. F. Lange, H. J. Siebeneck and D. P. Hasselman, *J. Am. Ceram. Soc.*, **59** (1976) 454.
- [170] D. Gerlich and G. A. Slack, *J. Phys. Chem. Solids*, 46 (1985) 433.



**CURRICULUM-VITAE**

*Family name* : Matović  
*Given name* : Branko  
*Date of birth* : November 26, 1959.  
*Place of birth* : Kraljevo, Jugoslavia  
*Nationality* : Serbian  
*Family status* : Married, one child

***Education and working Experiences:***

9. 1966 – 6. 1974 Primary School, Kraljevo, Jugoslavia.  
9. 1974 – 6. 1979 Gymnasium, Kraljevo, Jugoslavia.  
9. 1979 – 6. 1989 Dipl. Eng. Mineralogy and Crystallography, University of Belgrade.  
*Thesis : Preparation of Basalt-based Ceramics*  
8. 1990 – 11. 1998 Working in Institute for Refractory materials (Magnohrom Company).  
11. 1998 – 5. 2000 Working in Institute for Nuclear Science (Lab. for Material Science).  
9. 1992 – 6. 1994 Specialization in the field of refractory materials, University of Belgrade.  
*Title: Hydratation of High Aluminate Cement.*  
9. 1994 – 5. 1999 Master of Science degree in Mineralogy, University of Belgrade.  
*Master thesis : Mineralogical and Kinetics Investigation of Aluminate Cement.*  
5. 2000 – Now Studying for the degree Ph.D. of Science in Max-Planck-Institute for Metals Research and University of Stuttgart, Stuttgart, Germany, supported by Max-Planck-Society Scholarship.

*Ph.D. thesis* : **Low-temperature sintering additive for Si<sub>3</sub>N<sub>4</sub>**